Università degli Studi di Modena e Reggio Emilia

Dipartimento di Scienze Fisiche Informatiche e Matematiche
Corso di Dottorato di Ricerca in Fisica e Nanoscienze

MANIPULATING SPIN TRANSFER TORQUE WITH LIGHT

Relatore:
Dr. Massimo Rontani

Candidato:
Karsten Leding Vendelbjerg

Direttore della Scuola:
Prof. Marco Affronte

XXVIII

Contents

1 Introduction **3**
- 1.1 Background of Spintronics . . . 3
  - 1.1.1 Giant Magnetoresistance Effect . . . 3
  - 1.1.2 Tunnel Magnetoresistance . . . 6
- 1.2 Spin Transfer Torque . . . 7
  - 1.2.1 A Cartoon Picture for Spin Transfer Torque . . . 7
  - 1.2.2 Magnetic Dynamics in a Nanomagnet . . . 9
  - 1.2.3 Magnetic Switching . . . 11
  - 1.2.4 Persistent Magnetic Precession . . . 14
- 1.3 Dilute Magnetic Semiconductors . . . 15
  - 1.3.1 $Ga_{1-x}Mn_xAs$ as a model system for III-V DMS . . . 16
  - 1.3.2 Dynamic polarization of electrons in a non-magnetic layer. . . . 17
  - 1.3.3 Electronic structure . . . 19
  - 1.3.4 Magnetic interactions . . . 24
  - 1.3.5 Theoretical models . . . 26
- 1.4 Optical Reversal of Magnetization . . . 27
  - 1.4.1 Non-thermal origin . . . 28

2 Theoretical Background **33**
- 2.1 Junction Hamilitonian . . . 33
  - 2.1.1 Heisenberg equation of motion . . . 35
- 2.2 Gauge transformation of the Optical field . . . 36
- 2.3 Solution Bulk Problem . . . 38
- 2.4 Solution of the Scattering Problem . . . 40
  - 2.4.1 Basic Considerations . . . 40
  - 2.4.2 Boundary Conditions . . . 42
  - 2.4.3 Calculation: Transmission and Reflection Coefficients . . . 43
  - 2.4.4 Transmission and Reflection . . . 44
- 2.5 Conclusion . . . 47

3 Manipulating spin transfer torque with light **49**
- 3.1 Introduction . . . 49
- 3.2 Semiconductor-nanomagnet-semiconductor junction . . . 50
- 3.3 Scattering matrix . . . 51
- 3.4 Spin transfer torque . . . 55

3.5 Single channel 58
3.6 Conclusions 60

4 Conclusion **63**

Introduction

This Thesis is a theoretical proposal concerning the fundamental physics of nanoscale magnetic devices (a field known as spintronics) and its control by means of light. Spintronics is a relatively new area of electronics/magnetics engineering in which the spin or angular momentum of the electron in ferromagnetic materials plays a fundamental role. The signal is a magnetoresistance which depends on the relative orientation of the magnetic directions in adjacent ferromagnetic layers. The possibility to control the magnetic direction, and thereby change the readout, can be explained by considering exchange of spin angular momentum, refereed to as 'spin transfer', which was first introduced by Slonczewski and Berger in 1996. Even if spin transfer has been investigated intensively for the last fifteen years, important issues related to its control still draw a great deal of attention nowadays. The most important issues regard the reduction of current density required for magnetization switching, as well as enhancement of switching efficiency and thermal stability. Those challenges have to be overcome before current-controlled spin valve devices can replace the memory cells operated by external magnetic field which are used today. Such a technological progress, if realized, would certainly offer higher data storage density and faster manipulation with the information stored on a hard drive memory.

A real breakthrough would be the integration between spintronics and the well-established field of semiconductor electronics. In particular, an intriguing possibility offered by semiconductors is to use light as a handle to control spin transfer. Whereas this has already been the object of a great experimental and theoretical effort, for example aimed to pursue the optical reversal of the magnetization, here we take a different path and focus on the virtual absorption of photons, when the photon energy of the laser shining the device is smaller than the optical energy gap. If the laser is sufficiently strong, one may increase the coherence of the system in a controlled way (optical Stark effect) in the absence of real light absorption, i.e., without heating the system. In this Thesis we show that this could actually be useful to realize the coherent control of spin transfer torque (STT).

Specifically, we consider theoretically a one-dimensional junction made of a thin magnetic layer sandwiched between two identical direct-gap semiconductors. This layer, which could be made of a dilute magnetic semiconductor, acts as a spin-dependent contact force on electrons, as a n-type spin polarized current flows through the junction inducing a STT on the magnetic layer. As we shine the junction with an intense monocromatic laser beam, whose photon energy is smaller than the band gap, we drive a controlled excitonic coherence into the system. The Rabi energy couples conduction and valence bands, inducing an evanescent wave at the junction interface. We find that the Fano-like interference between this localized wave and the continuum spectrum may significantly vary with the spin projection of the scattering wave, which strongly affects the STT. The toy model we investigate here neglects many relevant features of actual devices, most noticeably band asymmetry, spin-orbit coupling, structure of the semiconductor-magnet interface, which will obviously affect our conclusions. Nevertheless, our aim here is to illustrate a novel concept that is possibly relevant for the coherent control of STT, leaving a more realistic case study to future research.

This Thesis is organized as follows:

Chapter 1 reviews the key concepts and ingredients of our proposal, including spin transfer torque, magnetic semiconductors, as well as an experimental setup reported in the literature that is close to the one we investigate theoretically.

Chapter 2 provides details about our theoretical approach and related concepts.

Chapter 3 is a manuscript by Karsten Leding Vendelbjerg and Massimo Rontani, presently submitted to the journal Superlattices and Microstructures, which reports the original findings of the present Thesis.

1 Introduction

1.1 Background of Spintronics

We introduce the fundamental spintronics development over time starting with the introduction to the Giant Magnetoresistance Effect, where the resistance is at a minimum when the two ferromagnetic layers are parallel, maximum when they are anti-parallel. To enhance resistance of the GMR structure, the non-magnetic metallic spacer can be replaced by a tunnel barrier.

Technological advancement in 20th century was largely based on the development of electronic devices. These devices provide the ability to control electron flows on microscopic scales, thereby enabling functions essential to applications in information technology. So far, most electrical devices are based on manipulating the electron's electric charge. However, besides electric charge, electrons also possess an intrinsic spin. In recent years, there have been intensive efforts to explore the possibility of manipulating electrons via their spins. Many achievements have been made along the way and have led to the opening of a new field, so called "spin based electronics" or "spintronics".

Spintronics has promising potential for making a new generation of devices that can offer great advantages such as non-volatility, increased speed and density, reduced power consumption, etc.[1] One good example of the benefit of spintronics is the "Giant Magneto-Resistance" (GMR) effect. It allows electrical detection of the magnetic orientation of a ferromagnet. Compared to the traditional method of detecting magnetization via electro-magnetic induction, the GMR effect becomes more efficient when the size of the magnet shrinks down to the nano-scale. The GMR effect is used in the read head of a hard drive to sense the magnetic field generated by the storage media, and its use has led to the increase of storage density by orders of magnitude. Another example is "Magnetic Random Access Memory" (MRAM), which uses the magnetic element for storing data. As the magnetic bit will not lose its magnetization over time, it can retain information without consuming any power "non-volatile". The reading and writing of data are done electrically, unlike the mechanical reading and writing in hard drives, which allows very fast operation speed. The reading mechanism is through the GMR effect mentioned above. For writing, one promising mechanism is through "Spin Transfer" effect.

1.1.1 Giant Magnetoresistance Effect

The Giant Magnetoresistance effect, discovered in 1988[2],[3], refers to the change of resistance of a ferromagnetic/non-magnetic/ferromagnetic metallic multilayer structure as the relative orientation of the magnetizations of two ferromagnetic layers changes, as illustrated in Fig. 1.1. The resistance is maximum when the magnetizations of two ferromagnetic layers are anti-parallel and minimum when they are parallel. The resistance difference between the maximum

and minimum values can be as much as a few 10's of percent, much larger than the scale of the anisotropic magnetoresistance ($\sim 1\%$) in metals, which is the reason for its name - "Giant Magnetoresistance".

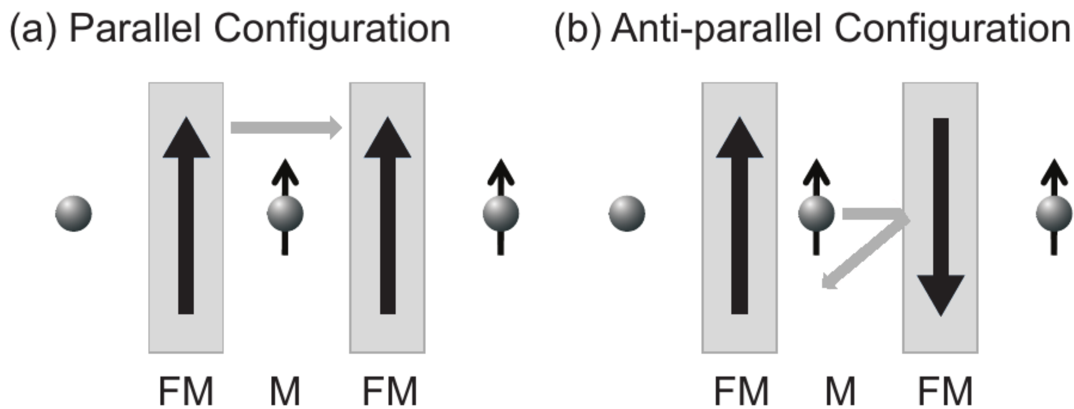

Figure 1.1: *Illustration of the GMR effect.* [3]

To understand the GMR effect, let us first consider a simple case: electrons passing through a single ferromagnetic layer. For a 3d transitional ferromagnetic metal like Ni, Co and Fe, ferromagnetism comes from the exchange coupling of the 3d electrons. In a simplified band structure for ferromagnetic metals, the exchange coupling results in an energy splitting of the 3d bands so that when the spin-up band and the spin-down band are filled up to the Fermi level there are more spin-up electrons than spin-down, so a net magnetization is induced. Another consequence is that the majority and minority spin bands also have different density of states at the Fermi level, see Fig. 1.2 for illustration. The conduction properties of a metal are primarily determined by the electrons near the Fermi level. Thus, when spin unpolarized electrons consisting of equal numbers of spin-up and spin-down electrons travel in a ferromagnet, different spins experience different resistances. In addition to the resistance within the ferromagnet, different types of spins also experience different scatterings at the ferromagnet/normal metal interface due to the band structure mismatch. Overall, one type of spin has a higher probability to transmit through than the other type. Therefore after passing through, electrons will become partially polarized in one spin direction. For Fe/Cu, the polarization is in the majority spin direction, while for Fe/Cr where GMR was first discovered, it is in the minority spin direction. The ferromagnet simply works as a spin filter.

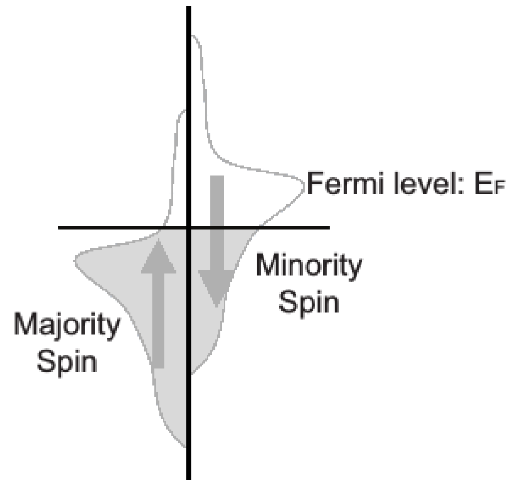

Figure 1.2: *A simple band structure for ferromagnet. The majority and minority spin bands have an energy split so they have different densities of states at the Fermi level.* [3]

When the spin polarized electrons travel into the non-magnetic spacer, they can maintain their spin directions for a relatively long distance when spin-dependent scattering is weak. For example, the spin diffusion length is on the order of 100's nm in Cu which is a typical material for the spacer. In the GMR structure, the spacer thickness is usually much smaller than the spin diffusion length so that the spin polarization is maintained when electrons reach the second layer. Then the probability for the electrons to transmit through the second ferromagnetic layer depends on the relative orientation of its magnetization and the electron spin polarization which is determined by the magnetization of the first layer. So when the second layer is parallel to the first layer, the same spin that has experienced a low resistance from the first layer will also have a higher probability to pass through the second layer. Overall this type of spin dominates the transport property through the multi-layer structure, which gives a low resistance. If the second layer is anti-parallel to the first layer, electrons of both spins experience high scattering in one layer or the other, and the resistance thus changes to a higher value. This resistance change is purely due to interactions with electron spins, so the GMR type of structure is also referred as a spin valve.

In general, the resistance of a GMR structure is minimum when the two ferromagnetic layers are parallel, maximum when they are anti-parallel, and its dependence on the relative angle between the two layers, θ, has roughly a cosine form:

$$R(\theta) = R_P + (R_{AP} - R_P)\cos(\theta) \tag{1.1}$$

This resistance dependence on the relative orientation of the ferromagnetic moments makes GMR useful in a number of applications. For example, it provides a way to electrically detect the orientation of a ferromagnet. As mentioned previously, this has benefited greatly the hard drive industry. It is also the read-out mechanism in MRAM applications. Furthermore, GMR also has a broad impact in the study of spin dependent electron transport in solid state devices and its discovery is widely considered as the beginning of the spintronics field. For this reason,

the 2007 Nobel Prize for Physics was rewarded to Fert and Grunberg for the discovery of GMR.

1.1.2 Tunnel Magnetoresistance

In a GMR structure, the non-magnetic metallic spacer can be replaced by a tunnel barrier. It will still show a similar effect of resistance dependence on the relative orientation of the ferromagnets, but with an even larger change. This is the "Tunnel Magnetoresistance" (TMR) effect. This effect was first discovered by Julliere in 1975 in Fe/GeO/Co magnetic tunnel junctions (MTJ)[4]. He also developed a simple model to explain the resistance change. His model assumes that the electron spin is conserved during the tunnelling process. Therefore the tunnelling probability of each type of spin can be calculated independently, as illustrated by Fig. 1.3. The tunnelling probability across the tunnel barrier (and hence the conductance) is proportional to the density of states of both initial and final states. Then we have

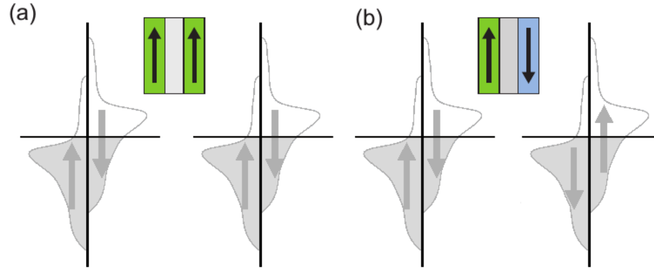

Figure 1.3: *Spin dependent tunneling across the tunnel barrier for (a) parrallel configuration of two ferromagnet and (b) anti-parrallel configuration.*[5]

$$G_P \propto \rho_{L\uparrow}\rho_{R\uparrow} + \rho_{L\downarrow}\rho_{R\downarrow} G_{AP} \propto \rho_{L\uparrow}\rho_{R\downarrow} + \rho_{L\downarrow}\rho_{R\uparrow} \quad (1.2)$$

where G_p (G_{ap}) is the parallel (anti-parallel) conductance, $\rho_{L\uparrow}$ and $\rho_{L\downarrow}$ ($\rho_{R\uparrow}$ and $\rho_{R\downarrow}$) are the densities of states for up and down spins of the left (right) ferromagnet. By definition, the spin polarization P is

$$P = \frac{\rho_\uparrow - \rho_\downarrow}{\rho_\uparrow + \rho_\downarrow} \quad (1.3)$$

Therefore the tunnel magnetoresistance ratio can be calculated as

$$TMR = \frac{R_{AP} - R_P}{R_P} = \frac{G_P - G_{AP}}{G_{AP}} = \frac{2P_L P_R}{1 - P_L P_R} \quad (1.4)$$

Unlike in the GMR structure where the spin dependent transport only contributes a small part to the total resistance, spin dependent tunneling has a dominating effect in TMR structure so that the TMR ratio can be much larger than GMR. In early studies of MTJs, a TMR ratio of a few 10's of percent was achieved with amorphous aluminum oxide (AlO) barriers. More recently, single crystalline magnesium oxide (MgO) barriers were predicted to provide a much higher TMR ratio due to the wavefunction match between the ferromagnetic electrodes and the tunnel

barrier[6],[7]. TMR ratios of around 200% were then demonstrated[8],[9] and led to intensive studies in MgO based MTJs. Today TMR values of 600% at room temperature and over 1000% at 4.2 K have been observed in CoFeB/MgO/CoFeB junctions[5]. We anticipate spin-dependent tunneling to be relevant for the theoretical proposal of ours illustrated in Chapt. 3.

1.2 Spin Transfer Torque

We describe in detail the mechanism of STT first from a simple cartoon picture, where the magnetization is fix. Followed by a more realistic model where the magnetization is treated dynamic, which can result in the possibility of magnetic switching where the orientation of the magnetization is changes due to spin transfer.

In GMR and TMR structures, the ferromagnetic electrodes influence the transport property of the spin polarized electrons via their magnetization. On the other hand, the spin polarized electrons also have an effect on the ferromagnets, that is, they can apply a torque on the ferromagnets via transfer of angular momentum. This torque can be strong enough to reverse the magnetization of the nanomagnet or excite persistent precession of the magnetic moment. This "Spin Transfer Torque" effect was first predicted by Slonczewski[10] and Berger[11] in 1996. Direct experimental observations of spin-transfer-induced magnetic reversal were made in 1999[12],[13] and first measurement of steady state magnetic precession was done in 2003[14], both at Cornell. The spin transfer effect provides an efficient way to manipulate the magnetic moment of a nanoscale magnet, which not only generates much interest in its technological applications, but also enables new kinds of studies of magnetic dynamics. A recent review of spin transfer torque can be found in[15].

1.2.1 A Cartoon Picture for Spin Transfer Torque

The spin transfer effect can be explained in a cartoon picture shown in Fig. 1.4. Consider a spin polarized electron entering a ferromagnet whose magnetization is in a direction non-collinear to the electron spin. When the electron passes through, as we have discussed in the GMR effect, the ferromagnet polarized the electron spin so that the outgoing electron has its spin in the same direction as the ferromagnet. If we then analyse the electron spin before and after, we will notice that there is a net change in its angular momentum, shown as the light gray arrow in 1.4. Due to the conservation of angular momentum, this component must be absorbed by the ferromagnet as it depolarizes the electron, and therefore a torque is applied on the ferromagnet by the electron. This seems to be a small effect, since the maximum angular momentum one electron can transfer is only $\hbar/2$. However as many electrons add together, for a small enough magnet, we can apply a reasonable amount of current to achieve a torque strong enough to re-orient the direction of its magnetization.

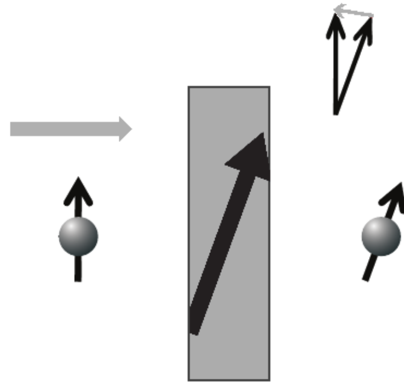

Figure 1.4: Illustration of the transfer of angular momentum when a spin polarized electron passes through a non-collinear ferromagnet.[15]

In a GMR or TMR structure of ferromagnet/spacer/ferromagnet, one of the ferromagnetic layers is usually made thicker or kept fixed by exchange bias so that this layer (the fixed layer) is less susceptible to spin torque and mainly serves as a polarized to provide spin polarization. The other layer (the free layer) is usually thin and can be excited by spin torque. Figure 1.5 illustrated the dependence of the spin torque on the direction of the current. When electrons flow from the fixed layer to the free layer, electrons are first polarized by the fixed layer, and then apply a torque on the free layer that rotate it toward the fixed layer direction. If current direction is reversed, the direction of torque on free layer is also reversed since now we need to analyse the electrons reflecting back from the fixed layer which have opposite spins as they enter the free layer compared to the previous case. The torque on the free layer now favours anti-parallel configuration of the two layers. So by controlling the current direction, we can control the direction of the spin torque, in favour of either parallel or anti-parallel configuration, providing an efficient way to manipulate the magnetic moment of a ferromagnet.

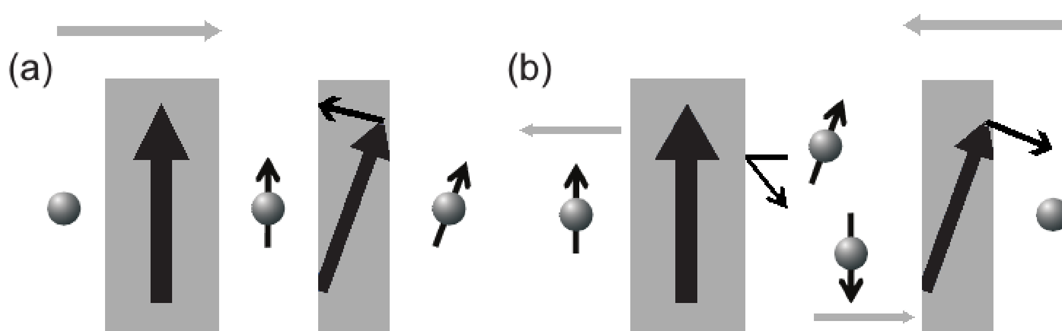

Figure 1.5: Direction of the torque on the free layer depends on the direction of the current.[15]

The above picture is only an intuitive cartoon for purpose of illustration. To calculate the quantitative behaviour of spin torque, one needs account for many realistic factors, for example, the detailed electronic structure of the material, whether the spin transport process is through diffusive or ballistic transport, etc. More detailed discussion can be found in the review paper[15]

and references therein. One simple form for spin torque in a symmetric ferromagnet/metallic spacer/ferromagnet structure was given by Slonczewski[16]

$$\frac{d\hat{M}}{dt} = g(\theta)\frac{\gamma\hbar I}{eV_{free}M_s}\hat{M}\times(\hat{M}\times\hat{M}_{fix}) \tag{1.5}$$

where $\hat{M}$ and $\hat{M}_{fix}$ are unit vectors for the magnetization of the two ferromagnetic layers, γ is the gyromagnetic ratio, $\hbar$ is the reduced Planck constant, I is the current, e is the electron charge, V_{free} is the volume of the free layer, M_s is the saturation magnetization of the free layer, and $g(\theta)$ is the unit less spin transfer efficiency. It has the form

$$g(\theta) = \frac{A}{1+B\cos(\theta)} \tag{1.6}$$

where A and B depend on details of the layer structure.

As indicated by Eq. 1.5, the direction of the torque is confined to be in the plane defined by the two ferromagnetic moments, perpendicular to the free layer direction, and pointing either toward or away from the fixed layer moment depending on the sign of the current. This behaviour is generally true for all metallic devices, while in magnetic tunnel junctions, there is also a component perpendicular to the plane defined by the two moments and it has a non-linear dependence on the bias applied across the tunnel barrier[17,18]. Nonetheless, Eq. 1.5 is good enough to describe the general effects of spin transfer torque.

1.2.2 Magnetic Dynamics in a Nanomagnet

Typically devices structure consist of two ferromagnetic layers separated by a spacer. The multilayers are patterned into a elliptically-shaped nanopillar with size typically around 100 nm, see Fig. 1.6. The top and bottom of the devices are connected to electrical leads to allow current to pass perpendicularly through the multilayers.

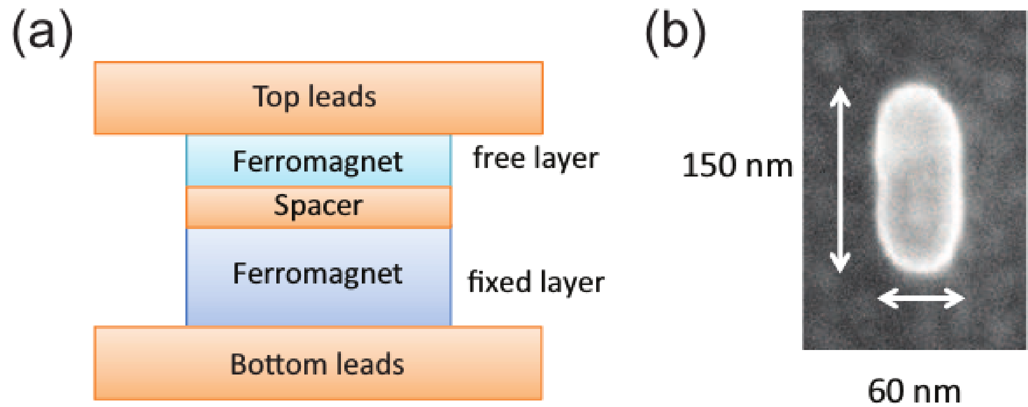

Figure 1.6: *(a) Structure of a nanopillar device. (b) SEM image of the elliptical shape of the nanopillar.*[15]

In each of the ferromagnetic layers, the magnetic moments of individual atoms are strongly

coupled together via exchange coupling. The result is that these magnetic moments will tend to move together and the variations among different moments can usually be ignored on such a small length scale. So we can substitute all the magnetic moments with a single moment or a "macrospin". This macrospin picture makes the analysis much easier and is quite good in explaining many behaviours of the magnetic dynamics in the nanomagnet.

In the thin elliptical-shaped magnetic free layer made of typical ferromagnetic materials such as Ni/Fe alloy or Co/Fe alloy, the magnetic easy axis is along the long axis direction of the ellipse due to shape anisotropy[1]. Without any external field, the magnetization of the free layer will lie in the energy minimum direction which is along the easy axis and can point to either end of the device. A detailed magnetic energy contour at zero external field can be calculated within the macrospin model and is shown in Fig. 1.7. Away from the magnetic easy axis, the energy contour has an elliptical shape due to the strong demagnetization field in the out-of-plane direction. Therefore when the magnetization is excited, it will follow these energy contours and precess around the easy axis.

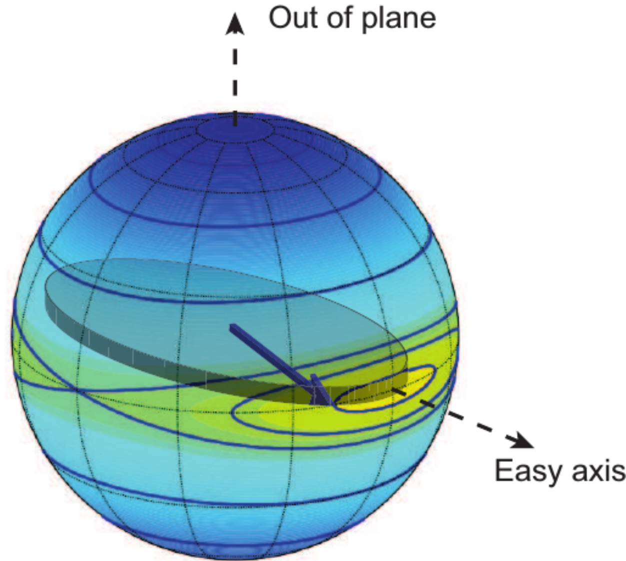

Figure 1.7: *Magnetic energy contour of a nanomagnet.* [15]

The dynamics of the magnetization in the presence of spin transfer can be described by the classical Laudau-Lifshitz-Gilbert (LLG) equation including an additional term for the spin torque:

$$\frac{d\hat{M}}{dt} = -\gamma\hat{M} \times H_{eff} + \alpha\hat{M} \times \frac{d\hat{M}}{dt} + g(\theta)\frac{\gamma\hbar I}{eV_{free}M_s}\hat{M} \times (\hat{M} \times \hat{M}_{fix}) \tag{1.7}$$

where H_{eff} is the total effective field including the applied field $H_{applied}$ and the anisotropy field H_{anis}, and α is the damping constant. The first term is the field torque term τ_H which makes the magnetization precess around the effective field direction, as illustrated in Fig. 1.8. The second term is the damping torque $\tau_{damping}$ which characterizes the energy dissipation. On average it points toward the equilibrium position of the magnetization, so that without any excitation the

[1] The magnetic crystalline anisotropy in these materials is usually small and can be ignored.

magnetization will relax back to the equilibrium. The third term is the spin transfer torque τ_{ST}. As discussed previously, the direction of this torque depends on the direction of the electron flow. For electron flow from the fixed layer to the free layer, this torque is in the same direction as the damping torque assuming the fixed layer also along the effective field direction, so that it works with the damping torque to accelerate the relaxation of the magnetization. For electron flow from the free layer to the fixed layer, this torque works against the damping torque and thus can reduce the relaxation or even excite dynamics of the magnetization depending on its strength relative to the damping torque.

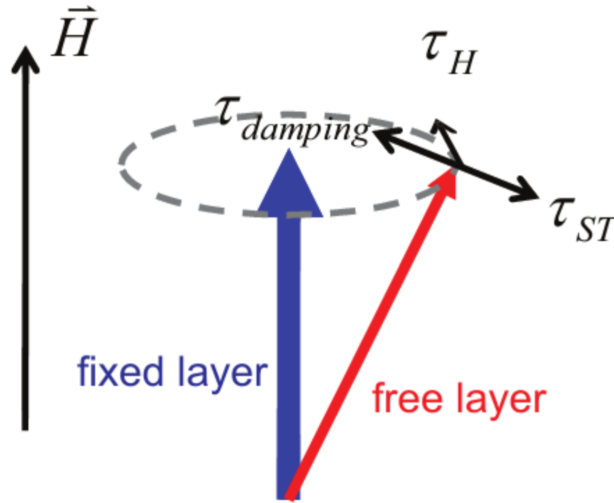

Figure 1.8: *Directions of the field torque τ_H, the damping torque $\tau_{damping}$, and the spin transfer torque τ_{ST}.* [15]

Usually the spin transfer torque is small compared to the field torque. So the effects of spin transfer torque can be viewed as either increasing or decreasing the amplitude of the magnetic precession. In general the magnetic dynamics excited by spin transfer torque can be categorized into two types: switching and persistent precession.

1.2.3 Magnetic Switching

At zero or small fields, both directions along the easy axis correspond to local energy minimums so it is possible to switch the magnetization between these two directions with spin transfer torque. For example, for a device with both free and fixed layers staying in the easy axis direction and parallel to each other, if we flow a positive current defined as electron flow from free to fixed layer, according to previous analysis, the spin torque acting on the free layer points away from the fixed layer and destabilizes this configuration so that the magnetic moment of the free layer goes into a precession around the easy axis. When the current increases, the amplitude of the free layer precession increases until it reaches the energy barrier which is around 90°. After that, the damping torque changes its direction and points toward the other local energy minimum. Now the spin torque and the damping torque are in the same direction, and the free layer relaxes to that energy minimum corresponding to anti-parallel alignment relative

to the fixed layer. Similarly, starting in the anti-parallel configuration, a strong enough negative current can switch the free layer back to the parallel configuration. If we monitor the resistance of the device, it will exhibit a hysteresis loop as we sweep the current, as shown in the example scan in Fig. 1.9.

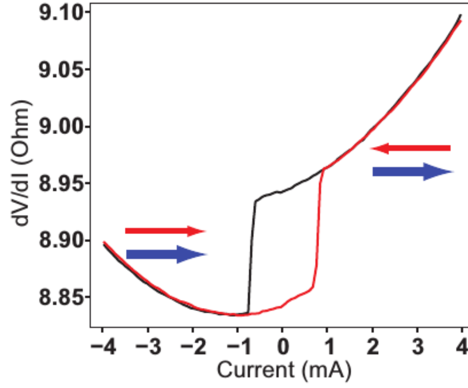

Figure 1.9: *Hysteresis loop of resistance as a function of current.* [19]

The current required to achieve switching at zero temperature (no thermal excitations) is defined as the critical switching current I_c . Above I_c, the spin torque is stronger than the damping torque and drives the free layer moment to switch direction. Figure 1.10 is a simulation example of a switching event. The switching proceeds via a precessional motion of the magnetization with increasing amplitude. Since the precession frequency is in the range of GHz, the switching can be a very fast process and typically finishes within a few nanoseconds. The switching time has a dependence on current in the form[19]

$$t_s \propto \frac{1}{I - I_c}. \tag{1.8}$$

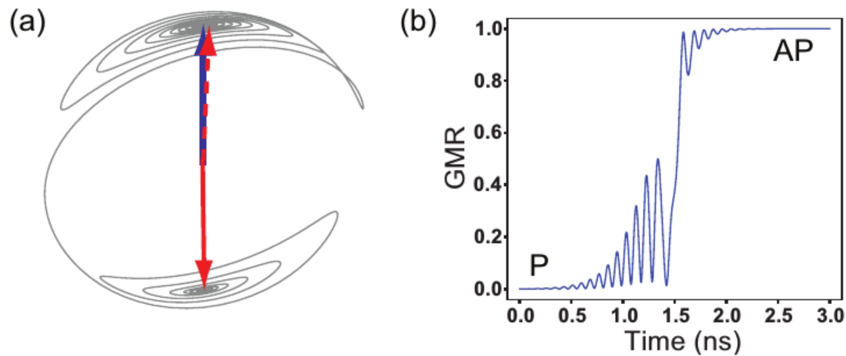

Figure 1.10: *An example of a simulated spin transfer switching event. (a) Trajectory of the switching. Red arrows indicates the direction of the free layer before (dotted line) and after (solid line) switching. Blue arrow indicates the direction of the fixed layer. (b) Corresponding normalized GMR as a function of time.* [20]

When the applied current is less than I_c , the spin torque cannot drive the free layer moment

to directly cross the energy barrier to achieve switching. Instead, it can only excite magnetic precession at small amplitudes. However, switching can still occur in this situation at finite temperatures due to thermal excitations. This is simply a thermal activation process. Disregarding spin transfer effect, thermally assisted magnetization reversal has been studied for a long time. The switching probability $P(t)$ can be described by the Neel-Brown relaxation time formula[20]

$$P(t) = 1 - exp\left(\frac{-t}{\tau}\right) \tag{1.9}$$

where t is the observation time, and τ is the relaxation time. τ is given by

$$\tau = \frac{1}{f_0} exp\left(\frac{E_b}{k_B T}\right) \tag{1.10}$$

where f_0 is the attempt frequency, E_b is the energy barrier, and T is the temperature. The effect of spin transfer on the thermally excited magnetic switching has also been studied in a number of experiments[19,21]. Theoretical calculations[22,23] suggest that the thermal fluctuations can be modelled by a fluctuating field with a Gaussian stochastic process. Then by solving the stochastic LLG equation including the fluctuating thermal field and its corresponding Fokker-Planck equation, they found that the form for the relaxation time τ can be modified as the following

$$\tau = \frac{1}{f_0} exp\left[\frac{E_b}{k_B T}\left(1 - \frac{I}{I_c}\right)\right] \tag{1.11}$$

Therefore the effect of spin transfer torque can be viewed equivalently as introducing either an effective energy barrier $E_b^* = Eb(1 - I/I_c)$ or an effective temperature $T_b^* = T/(1 - I/I_c)$. Above and below I_c, the switching time has very different dependences on the applied current Eq. 1.8 and Eq. 1.11. In order to achieve a very short switching time, a large current is required. This presents a problem for ST-MRAM applications. Many strategies have been pursued to improve the performance of spin transfer switching. These include: reducing the switching current by using large-aspect-ratio elliptical shape to reduce the volume of the free layer while maintaining thermal stability[24] or by partially cancelling the free layer demagnetization field[25], increasing the switching speed by using a perpendicular polarize to achieve out-of-plane precessional switching[26,27], and maintaining thermal stability by using perpendicularly magnetized materials[28]. We recall that a goal of the theoretical proposal of this Thesis is to improve the efficiency of spin transfer torque using coherent light without heating the system.

Another related topic is to develop techniques to characterize the magnetic switching process driven by the spin torque, especially on the ultrafast time scale down to below 1 ns. One technique is to study statistically the switching induced by nanosecond current pulses[24,29]. In this type of measurement, the device is excited by a nanosecond current pulse many times and the switching probability is measured. This technique is useful in determining the value of the critical current and its dependence on various experimental conditions and material parameters. However, it does not provide much information about the magnetic dynamics during switching. Another technique is to directly measure the switching in the time domain[19,30,31]. During the switching process, the precession of the free layer induces a resistance oscillation which is, at

the same time, converted to a voltage oscillation by the applied current bias. This oscillating voltage signal can then be recorded by an oscilloscope. For metallic spin valves, this voltage signal scale is very small due to the small GMR ratios. Therefore, to achieve enough signal-to-noise ratio requires averaging over many switching events[19,30,32]. However due to thermal fluctuations, the switching is not a repeatable process so that most of the oscillation signal is washed out after averaging. In magnetic tunnel junctions, the large TMR ratio makes it possible to study the switching with single-shot technique on an event-to-event basis[33,31].

1.2.4 Persistent Magnetic Precession

The other type of dynamics that can be excited by spin transfer torque occurs when a large magnetic field is applied on the sample. In this case, the energy profile of the free layer is changed and there is only one local energy minimum which is along the magnetic field direction. Now if a positive current is applied to the sample, the spin torque can drive the free layer away from the energy minimum. Since there is no other stationary equilibrium state, the free layer will remain in a dynamic state - it will precess steadily around the field direction, as shown in Fig. 1.11. During one cycle of precession, the spin torque cancels out the damping torque on average so that the precession reaches a steady state. This steady-state precession produces a resistance oscillation and hence a voltage oscillation in the microwave frequency range. The frequency can be tuned by the applied field and the applied current. These features allow spin transfer devices to be used as nanoscale microwave oscillators with tunable frequencies.

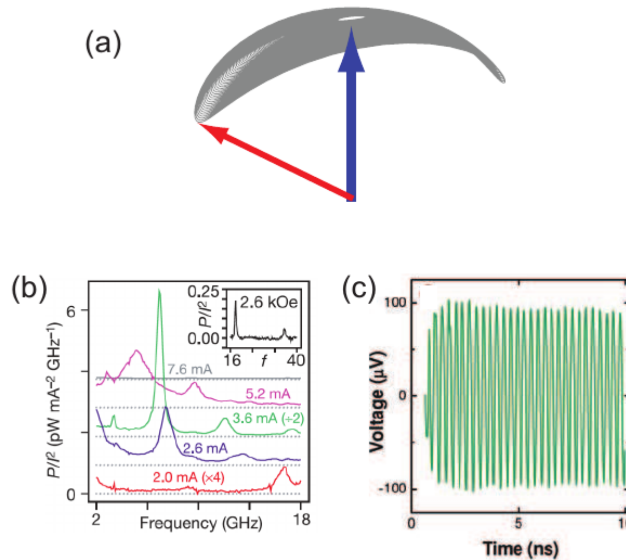

Figure 1.11: *Illustration of persistent magnetic precession. (a) Trajectory of a simulated persistent precession. (b, c) Characterization of the persistent precession in (b) frequency domain[14] and (c) time domain[30].*

The first direct experimental observation of spin-transfer-driven persistent precession was made at Cornell in 2003 by measuring the microwave signal with a spectrum analyser[14]. It can also be measured directly in the time domain[30,34]. One important issue regarding spin-transfer based nano-oscillators are the coherence time. Long coherence time means narrow linewidth

in the power spectrum, and this is desirable for nano-oscillator applications. A lot of efforts have been made in trying to understanding the mechanisms limiting the linewidth of spin-transfer-driven oscillations. In spin valve structures, experiments have been made to study the dependence of linewidth on temperature [35], on the excitation of the fixed layer dynamics [36], on the in-plane angle of the magnetic field [37], and on the switching between different dynamic modes [34]. Non-uniform magnetic structures such as magnetic point contact devices [38,39] and magnetic vortex devices [40,41] have also been studied and have achieved much narrower linewidths than in spin valves.

Spin-Transfer Ferromagnetic Resonance

Besides the DC-driven persistent precession, an AC current can also excite magnetic dynamics in a resonant fashion. The AC-excited magnetic precession can be detected by measuring a DC voltage resulting from mixing between the resistance oscillation and the AC current drive. This Spin-Transfer Ferromagnetic Resonance (ST-FMR) technique [42,43] is similar to the traditional ferromagnetic resonance, but can be performed in much smaller samples. It can characterize important material properties such as magnetic damping [44]. It can also directly measure the strength of the spin transfer torque, and, particularly, in magnetic tunnel junctions, it can provide quantitative measurements of the spin torque vector and its bias dependence [45,46], which is very important in understanding the spin dependent tunnelling process and characterizing and optimizing the MTJs for applications. Furthermore, it can provide information about magnetic modes observed in the DC-driven dynamics measurements [44].

1.3 Dilute Magnetic Semiconductors

We introduce a brief introduction to diluted magnetic semiconductors, and more specifically to $Ga_{1-x}Mn_xAs$. We describe the electronic structure of $Ga_{1-x}Mn_xAs$ and the magnetic interactions that may be relevant for this material, and discuss the hole mediated ferromagnetism in more detail. A brief overview is given of theoretical models that describe the origin of the ferromagnetism in $Ga_{1-x}Mn_xAs$, as these are the candidate materials to realize the junction we have theoretically studied in this Thesis.

Diluted magnetic semiconductors (DMS) consist of standard semiconductors in which some subset of the lattice atoms is randomly substituted by a magnetic atom, thus inserting local magnetic moments in the semiconductor matrix shown in Fig. 1.12. These magnetic moments can originate from $3d$ or $4f$ open shells of transition metals or rare-earth elements, respectively, so that typical examples of DMS are $Cd_{1-x}Co_xSe$, $Hg_{1-x}Fe_xSe$, $Zn_{1-x}Co_xS$, $Ga_{1-x}Mn_xAs$, $In_{1-x}Mn_xAs$ and $Pb_{1-x}Eu_xTe$ [47]. In most cases Mn is used as the magnetic dopant. The term DMS is usually reserved for single-phase systems to differentiate them from systems where magnetic second phases are incorporated as precipitates. In early works DMS materials have been also referred as "semimagnetic semiconductors" [48].

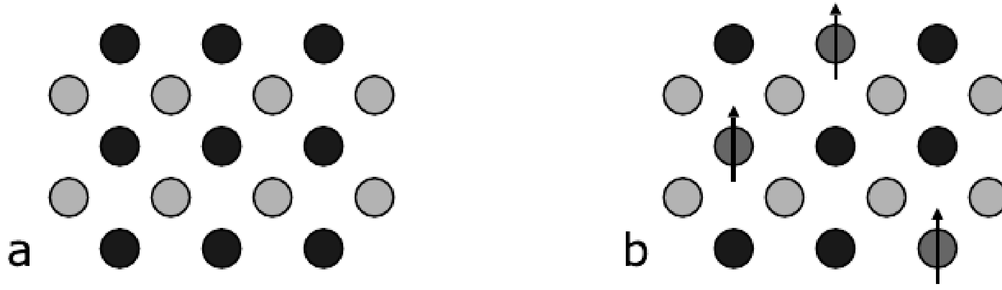

Figure 1.12: Schematic representation of a) non-magnetic semiconductors and b) diluted magnetic semiconductors. [49]

As magnetic semiconductors these materials combine the complementary properties of semiconductors and ferromagnets. DMS can exhibit a wide range of magnetic properties, from paramagnetism and spin-glass behaviour to ferromagnetism. They can span the range from highly insulating to metallic, even in the same alloy system.

In the 1970's and 1980's research on DMS was mainly focussed on II-VI based systems in which the valence of the cations matches that of the common magnetic ions such as Mn[47]. Although such materials are relatively easy to prepare, it is difficult to add p- or n-type doping to II-VI based DMS. The magnetic interaction in these materials is therefore dominated by the antiferromagnetic exchange among the *Mn* spins, which results in paramagnetic, antiferromagnetic, or spin-glass behaviour. However ferromagnetic ordering, with $T_c < 10K$ can be obtained in II-VI DMS with sufficient p-type doping[50,51], when the antiferromagnetic exchange is overcompensated by ferromagnetic interactions mediated by RKKY interaction[52].

The III-V semiconductors with a sizeable concentration of magnetic elements were not obtained until the 1990's due to the low solubility of transition metals in III-V materials of the order of 10^{18} cm^3 or less. The use of non-equilibrium growth, primarily by molecular beam epitaxy (MBE) at relatively low temperatures, made it possible to grow III-V DMS such as $In_{1-x}Mn_xAs$[53,54] and Ga_{1-x} Mn_xAs[55] with a considerably higher concentration of magnetic atoms.

1.3.1 $Ga_{1-x}Mn_xAs$ as a model system for III-V DMS

In III-V diluted magnetic semiconductors typically a fraction of the group-III cations is substituted by transition metal, mostly *Mn*. *As* the valence of the *Mn* ions in this position is 2, they do not only act as magnetic impurities but are also acceptors and dope the system with holes. There is a general consensus and vast experimental evidence that these holes mediate the ferromagnetic exchange interaction between the localized *Mn* spins. As these holes carry electrical current through the system, there is a crucial interaction between the transport properties, which are determined by the electronic band structure of the material, and the magnetic properties, determined by the nature of the magnetic impurities and the magnetic coupling.

The successful growth of ferromagnetic $Ga_{1-x}Mn_xAs$ films[55,56] and the relatively high Curie temperature T_c up to 110 K that could be obtained[57,58], attracted a lot of interest for this material from both a fundamental and an applied point of view. Nowadays $Ga_{1-x}Mn_xAs$

is one of the most extensively studied and best understood magnetic semiconductors. Mn concentrations that are typically studied vary between 2% and 10% of the total number of Ga-sites, and T_c values between 10 K and 173 K[53] can be obtained, depending on the Mn content and growth parameters, where the highest T_c's are obtained after a post-growth annealing treatment[53]. $Ga_{1-x}Mn_xAs$ has so far been successfully used in spin injection and detection experiments[59,60], and in components based on the TMR effect[61]. Although the Curie temperatures are still far below what is required for room temperature applications, $Ga_{1-x}Mn_xAs$ is very often considered as an important model system for III-V diluted magnetic semiconductors.

1.3.2 Dynamic polarization of electrons in a non-magnetic layer.

The article by *V.L. Korenev et al.*[62] suggested following experimental setup to polarize electrons created by photoexcitation in a FM layer. A hybrid ferromagnet-semiconductor systems is used, in which the different constituents take over the separate tasks required for making the device functional as a FM semiconductor. In such a FM-SC hybrid system, each component have specific properties as high charge carrier mobility.

This type of hybrid system could be a candidate for spintronic diverses, however besides the readout of the FM and that the device is electrical control which means that a high density $\sim 10^8 Acm^{-2}$ electric current[10,15], should be used for reorientation of the FM, such a huge current density would damage the semiconductor. The threshold can be decreased down to $10^5 Acm^{-2}$ in the low-temperature Mn-based ferromagnetic semiconductors[63]. Therefore, methods for reducing the current density have to be considered, whereas one method could be a coherent control of the STT by means of the sub-bandgap optical Stark effect. Which show promising results to change the efficiency of the STT without heating the system, suggested in this thesis.

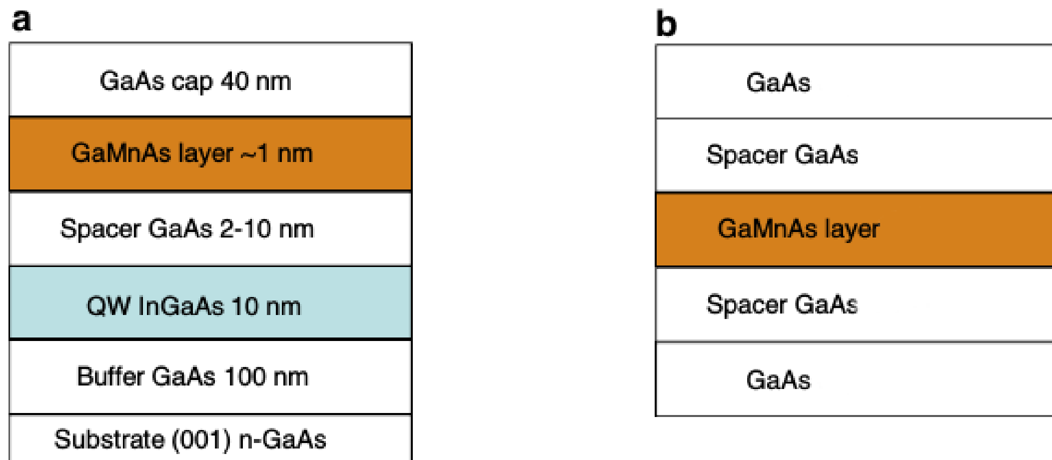

Figure 1.13: *Spin orientation of photoexcited carriers by FM layer. (a) Scheme of structures used by V.L. Korenev et al.*[62] *(b) Scheme of structures suggested in this thesis.*

The GaAs-based structures, fig. 1.13 (a), used by *V.L. Korenev et al.*[62] are very similar to the structure proposed in this thesis, see Fig. 1.13 (b) which thereby indicates that a hybrid

ferromagnet-semiconductor structure makes a interesting candidate for further work.

The spin separation is a result of an intense circularly polarized photoluminescence of the structure. The laser illumination have a photon energy $\hbar\omega = 1.92$ eV, slightly higher than the band gap of the GaAs, the photoluminescence spectrum consists of emission from the quantum well with a maximum at 1.417 eV, Fig. 1.14 (a), this emission arises from recombination of electrons and heavy holes in the ground states. The transfer of electron spin from the FM into the SC bulk is negligible in such a structure, so that the detection of ferromagnetism is local ($<$ 10 nm resolution). Figure 1.14 (b) shows the polarization hysteresis loop, measured at the photoluminescence maximum under linearly polarized above-barrier excitation. The coercive force is determined to be $B_c \sim 9$ mT, and the polarization, measured at 80 mT field strength, is 3.5 %. The appearance of hysteresis demonstrates that the polarization degree of the quantum well emission is controlled by the GaMnAs FM layer (magneto-optical Kerr rotation reveals a hysteresis loop with a shape that is similar to the one in fig. 1.14 (c). The magnetization of this layer is, however, detected by carriers localized in the InGaAs quantum well. The presence of hysteresis also means that the easy axis of magnetization is non-orthogonal to the growth axis [001], as reported for GaAs/AlGaAs structures with a δ-Mn layer.

The experiential procedure can thereby, be used as a guideline for experiential support of the theoretical proposal of this Thesis.

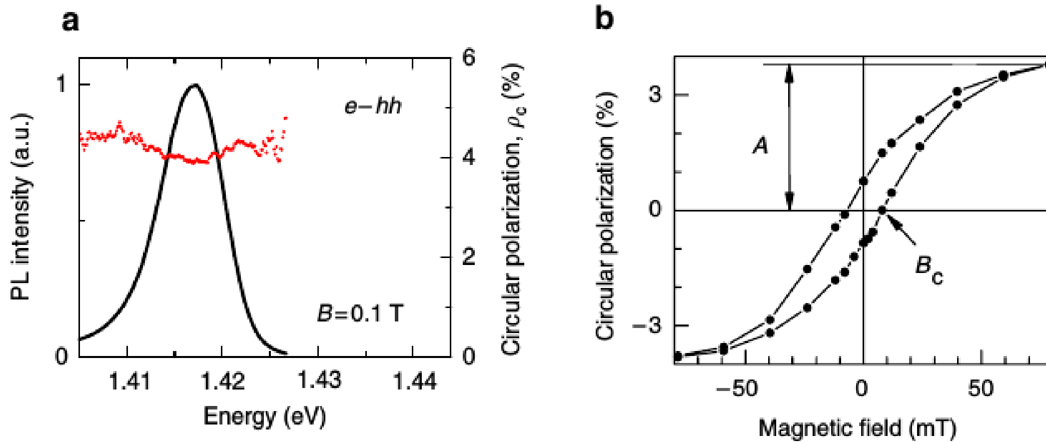

Figure 1.14: *Spin orientation of photoexcited carriers by FM layer. (a) Spectra of photoluminescence intensity (black curve) and polarization (red points) for 10 nm sample under linearly polarized excitation with photon energy 1.92 eV and power 2 mW. (b) Polarization hysteresis loop in Faraday geometry in 10 nm sample for the transition e-hh.* [62]

There are two main contributions to the FM-induced spin polarization of SC charge carriers: the first one is the equilibrium spin polarization due to the thermal population of spin levels split by the exchange magnetic field of the FM. In this case, the FM layer acts as spin polarizer. The second one is the non-equilibrium polarization arising from the spin transfer through the FM-SC interface. The authors of reference [64] use the FM as spin separator redistributing the spins spatially. The former mechanism is expected for FM/QW hybrids [65,64], whereas the latter is demonstrated via the spin injection/reflection of free electrons at a FM-SC interface. Here we show unambiguously that, in contrast to previous expectations, the spin polarization in

GaMnAs-based FM/QW hybrid is a non-equilibrium, dynamic one. The spin-separation effect considered here is due to the QW electrons and would take place even for the FM/QW hybrid embedded into insulating that is, non-injection structure.

1.3.3 Electronic structure

In this subsection we review in some detail the electronic structure of GaMnAs. As this is the candidate material for the active layer of the junction studied in this thesis, it is important to recall under which conditions the material is transparent to the light shining the junction.

Mn impurity levels

GaAs is a direct band gap semiconductor with an energy gap $E_g = 1.42$ eV at 300 K[66]. When magnetic impurities like Mn are incorporated in a semiconductor their magnetic and transport properties will depend on the positions of the energy levels corresponding to the magnetic shells with respect to the energy bands of the host semiconductor. Together with the on-site correlation energy U, this position of the Mn energy levels will determine the charge and spin state of the Mn atom, and whether it will act as a dopant. Isolated Mn atoms have (Ar)$3d^5 4s^2$ electron configuration, and when these atoms are incorporated in a III-V semiconductor, they are expected to substitute the trivalent cation. As the Mn atom has only two valence electrons, the formation of a hole is expected and at this substitutional position there are three possible electronic ground states for the Mn impurity: $A^0(d^4)$, $A^0(d^5+h)$ and $A^-(d^5)$[67]. Here, A^0 denotes the state in which the Mn center is neutral in respect to the GaAs background and thus corresponds to a Mn^{3+} state, while A^- is the "negatively charged" Mn^{2+} center. The notation in brackets is the electronic configuration of the d-electrons.

In case of $A^0(d^4)$ the hole resides in the Mn $3d$ shell. In $GaAs$ doped with Mn the A^0 (d^4) configuration is not observed[67], as due to a strong intra-site Hund coupling a state with five d-electrons is energetically more favourable, as is the case for $A^0(d^5+h)$ and $A^-(d^5)$. In accordance to that, photoemission measurements in $Ga_{1-x}Mn_xAs$[68] reveal an energy level deep (~ 2.7 eV) below the valence band edge which can be attributed to the Mnd^4/d^5 acceptor state, i.e. the transformation of the triply ionized ions Mn^{3+} into Mn^{2+}. As the acceptor state lies under the top of the valence band, the ground state corresponds to the Mnd^5 state. This is corroborated by x-ray magnetic circular dichroism (XMCD) studies which indicate that the 3d electron count of Mn is ~ 5[69].

When an $A^0(d^4)$ traps an electron tightly in the $3d$ shell forming the high spin, $S = 5/2$, $3d^5$ configuration, it is negatively charged in respect to the GaAs background and can therefore bind the hole in a effective mass acceptor state $A^0(d^5+h)$. The energy of this hydrogen-like state will then be found just above the valence band, where the binding energy of the hole corresponds to the ionization energy of the acceptor. In the low doping range Mn ions are indeed found to be acceptors with an ionization energy of 112 meV[66]. Various experimental results indicate that the ground state of the Mn impurity at low doping concentrations corresponds to the $A^0(d^5+h)$ configuration[67]. Photoemission experiments show that the itinerant holes originating from the Mn acceptor level mainly have an As $4p$-character, and can thus be associated with the host

semiconductor valence band[70]

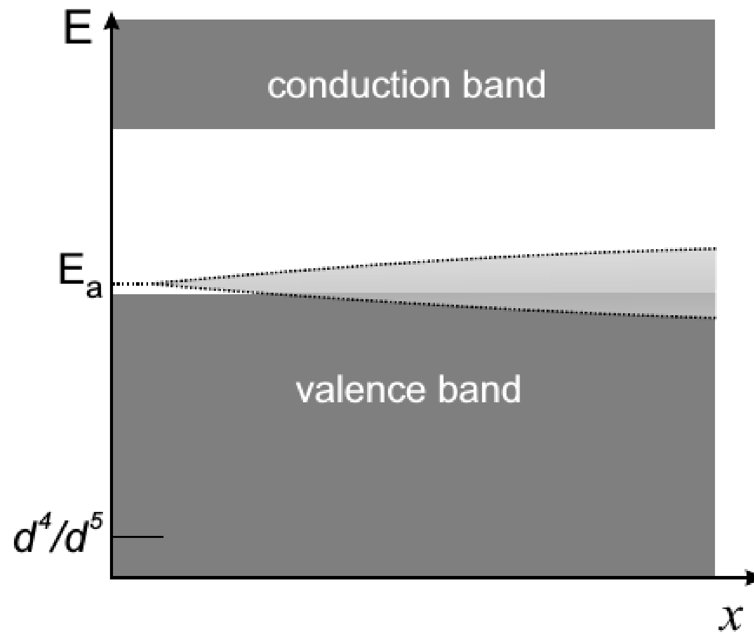

Figure 1.15: Schematic representation of the $Ga_{1-x}Mn_xAs$ energy band diagram at $k = 0$ as a function of the Mn content. [70]

When the Mn concentration is increased the acceptor states will start to overlap and the energy level will broaden and form an impurity band, see Fig. 1.15. At high Mn content this impurity band will merge with the GaAs valence band, leading to the insulator-to-metal transition as holes are induced in the valence band that can be considered as itinerant. In this case the ground state of some of the Mn atoms will be $A^-(d^5)$, where the hole resides in the valence band and the Mn ion is in the $3d^5$ $(S = 5/2)$ configuration. Electron spin resonance (ESR) spectra for MBE grown low-temperature $Ga_{1-x}Mn_xAs$ show only one resonance corresponding to $g = 2.0$[67], which is attributed to $A^-(d^5)$ centres. This configuration will also be favoured due to the high hole concentrations in the typical doping range of $Ga_{1-x}Mn_xAs$, which may lead to screening of the Coulomb potentials of the A^- centres, resulting in a lower ionization energy of the holes[67].

Metal-insulator transition

An additional effect which will in general influence the electronic structure of a semiconductor is the correlation between the charge carriers. These electron-electron (or hole-hole) interactions, result in a Hubbard split of the impurity band: an upper Hubbard band (UHB) is formed and the center of this band is separated from the middle of the actual impurity band or lower Hubbard band (LHB), by the correlation energy U. If one for example considers that an impurity center has a finite probability of being occupied by two charge carriers, then these two charges will repel each other and the correlation energy U is the Coulomb repulsion between two electrons in the same impurity orbital. When the doping level increases, then the distance R between the impurities decreases and both the lower and the upper Hubbard band broaden until they

overlap, as schematically depicted in Fig. 1.16 for electrons. Mott suggested that at this point, the metal-insulator transition[2] (MIT) occurs[71,72]. He also predicted that the MIT should occur at a critical electron concentration, n_c, given by $n_c^{1/3}\, a_B \approx 0.25$[72] where a_B is the effective Bohr radius for the isolated impurity center.

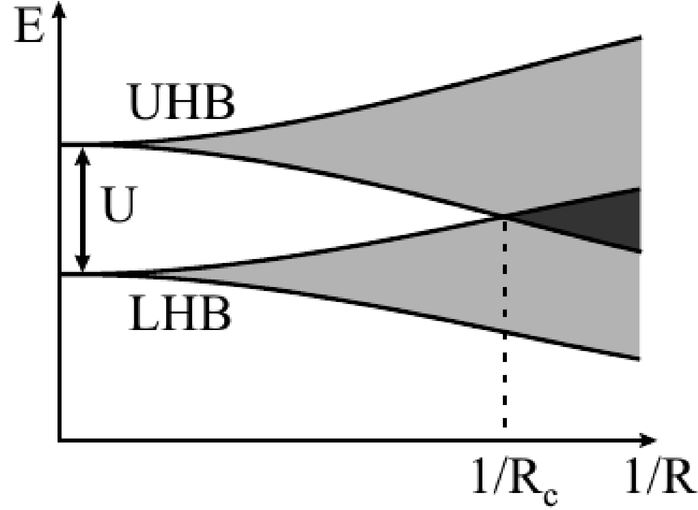

Figure 1.16: *Schematic illustration of the dependence of the Hubbard bands on impurity concentration. R is the mean distance between two neighbouring impurities ($R \approx n^{1/3}$), while $1/R_c$ marks the metal-insulator transition.*[71,72]

$Ga_{1-x}Mn_xAs$ can be considered as a charge transfer insulator, since the coupling of the carriers with the magnetic Mn centres significantly enhances the separation between the two Hubbard bands. Therefore one has to consider merging of the impurity band i.e. the lower Hubbard band with the valence band, rather than merging with the upper Hubbard band. As a consequence the critical distance R_c for the merging of the relevant bands decreases by a factor of two[71,72]. Like in other doped semiconductors, the metal-insulator transition will occur when the distance between the Mn acceptors becomes smaller than $R_c \approx 2.55 a_B$[71,72]. Since this distance is approximately $N_A^{-1/3}$, with N_A the acceptor ion density, one easily finds a simple criterion for the critical acceptor density n_c, similar to that derived by Mott[71,72]:

$$n_c^{1/3} a_B \approx 0.4 \tag{1.12}$$

The Bohr radius of $Ga_{1-x}Mn_xAs$ can however be estimated in several ways:

- When one considers the holes occupying the localized state of a single quantum-well, the energy eigenvalues are found to be dependent on the localization radius. Using the experimental Mn ionization energy $E_a = 112$ meV[66] the effective Bohr radius can thus be calculated as[73,74]

[2]One can also more generally call this a metal-nonmetal transition. However, for $T \to 0$ a semiconductor can be considered as an insulator.

$$a_B = \frac{\hbar}{\sqrt{2m_h^* E_a}} = 7.8\mathring{A} \tag{1.13}$$

where $\hbar$ is Planck's constant divided by 2π and m_h^* is the effective hole mass, which is evaluated at 0.56 times the electron mass [74]

- Applying the hydrogen model, effective mass theory, for a hole bound to the Mn acceptor ion in a dielectric GaAs background gives

$$a_B = \frac{4\pi\varepsilon_0\varepsilon_r\hbar^2}{m_h^* e^2} = 11.7\mathring{A} \tag{1.14}$$

Here, ε_0 is the vacuum permittivity, e is the electron charge, and ε_r is the static dielectric constant of the semiconductor matrix, $\varepsilon_r = 12.4$ for GaAs [66].

- Other expressions or slightly different estimates for the above parameters lead to similar values e.g. $a_B \approx 10\mathring{A}$ is also used in literature [75,76].

The quantum-well estimate, $a_B = 7.8\mathring{A}$, starts from the experimental ionization energy and is therefore likely to be more accurate. Moreover, amongst the cited values, it gives the highest critical concentration for metallic behavior, $N_c = 1.3 \cdot 10^{20} cm^{-3}$ or $x_c \approx 0.006\%$. However, as noted by *Dietl et al.* [77], a strong p-d antiferromagnetic interaction between the localized Mn spin and the hole spin enhances strongly the acceptor binding energy and reduces a_B. Thus the critical doping concentration can easily mount up to the experimentally found lower limit for metallic behaviour: $x_c \sim 1 - 1.5\%$ [78] or $N_c \sim 3.3 \cdot 10^{20} cm^{-3}$. When assuming $x_c = 0.015$, one can estimate this reduced Bohr radius as

$$a_B = 5.7\mathring{A} \tag{1.15}$$

Note that this value is approximately the $Ga_{1-x}Mn_xAs$ lattice parameter, and thus still larger than the distance between the Mn ion and the neighbouring As anions $d_{Mn-As} \approx 2.4\mathring{A}$, and the Mn-Ga distance $d_{Mn-Ga} \approx 4.0\mathring{A}$. Detailed theoretical studies [79,80] that include disorder and the typical defect configurations in $Ga_{1-x}Mn_xAs$, predict a metal-insulator transition for 1% Mn doping in GaAs, in good agreement with the experimental values.

Effects of disorder

The electronic band structure which is sketched above is still simplified a lot. One of the main refinements of this impurity band picture is the inclusion of disorder effects. A first effect of disorder is band tailing. The random distribution of charged impurities results in potential fluctuations of the band edges. This typically results in a tail is which is formed in the density of states at the band edge, due to states with energy above the unperturbed valence band.

The most important consequence of disorder is the possibility of charge localization. Anderson studied the impurity band structure for a non-ideal impurity lattice, by assuming a regular lattice of potential wells with a random depth [73,81]. His model contains one dimensionless

parameter W/I, where I is the overlap integral for neighbouring sites, while W is the energy interval in which the energy distribution can be considered uniform, and thus W is a measure for the disorder in the lattice. When W/I increases, i.e. increasing disorder and/or reduced overlap between neighbouring sites, regions with localized states appear at the band edges. The energy which separates the localized states at the band edges from the delocalized states in the middle is called the mobility edge E_m. As the disorder/overlap ratio increases the localized regions expand, until they take up the entire band for sufficiently large W/I. A similar phenomenon is expected for potential wells with constant depth but with a random distribution in space.

This model illustrates that depending on the doping, the compensation and the amount of disorder the electronic states in a impurity band may be localized or delocalized. By changing any of these parameters the Fermi level may cross from a region with localized states to a region with delocalized states. If the states at the Fermi level are extended than the system can be considered as metallic and the conductivity will tend to a finite value for $T \to 0$. If the states at the Fermi energy E_F are localized, then the electrical transport at low temperatures can only occur through electron or hole hopping, while at higher temperatures conduction can also take place by thermally activating charge carriers above the mobility edge. This model thus presents an alternative mechanism for the metal-insulator transition. To describe the MIT in a doped semiconductor both disorder as charge correlations must be considered and the Hubbard model and the Anderson model must be combined[71,72]. The MIT will then no longer occur when the upper and lower Hubbard band begin to overlap as both band edges will consist of localized states, but when the band broadening becomes large enough for E_F to cross the mobility edge.

In $Ga_{1-x}Mn_xAs$ with $x > 0.015$ the situation will be similar to what is drawn in Fig. 1.17(b). As estimated above, the Mn impurity band starts to overlap with the valence band at $x_c \approx 0.006$, while the typical Mn concentrations in $Ga_{1-x}Mn_xAs$ films largely exceed this critical value with $0.02 \leq x \leq 0.08$, so the overlap of the bands will be considerable. The doping efficiency determines to what extent the impurity band will be filled with holes, and thus it indicates whether and how deep the Fermi level resides in the valence band. Note that the discrepancy between the estimated $x_c \approx 0.006$ and the experimentally observed $x_c \approx 0.01 - 0.015$ may also be due to the fact that the overlapping regions of the impurity and the valence band initially only contain localized states.

The region with localized states at the band edges in Fig. 1.17 only serves as an illustration, since the exact position of the mobility edge will depend strongly on the amount of disorder in the $Ga_{1-x}Mn_xAs$ layer, and is thus influenced by the doping level, the defect concentration and the compensation. The relative positions of the Fermi level, the mobility edge and impurity band itself will eventually determine the transport properties, and should be considered for every sample individually. As will be discussed below, it is still a controversial issue whether the transport in $Ga_{1-x}Mn_xAs$ is really carried by itinerant or weakly bound holes that reside in the valence band, or rather by extended or bound carriers in the impurity band.

Due to the high concentration of randomly distributed charged impurities and the large amount of defects present in the samples, the disorder effects in $Ga_{1-x}Mn_xAs$ are expected to be strong, and although the systems may be above the Mott limit, they are close to being Anderson insulators due to these strong disorder effects. An overview of the effects of disorder on the transport and magnetic properties of diluted magnetic semiconductors, and $Ga_{1-x}Mn_xAs$ in

specific, can be found in a recent review article by Timm[82].

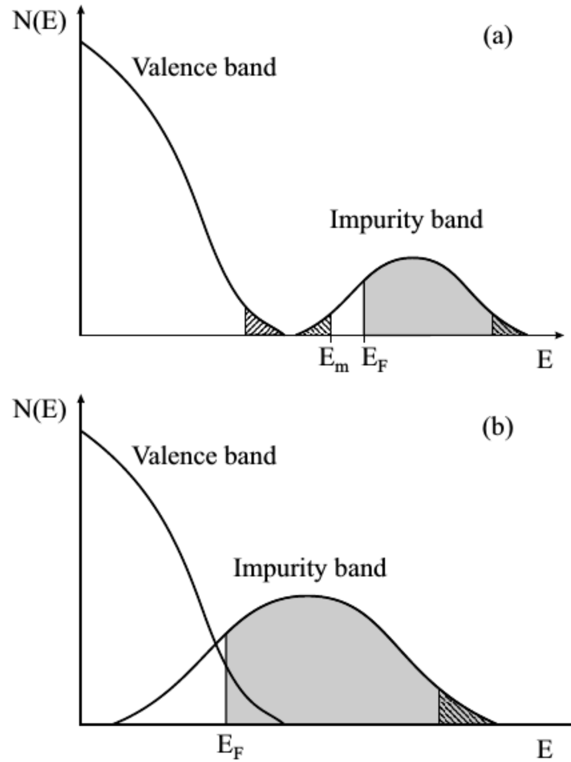

Figure 1.17: *Schematic representation of the band structure in a $Ga_{1-x}Mn_xAs$ compound with (a) $x \ll x_c$ and (b) $x > 1.5\%$. The localized states are dashed, while the gray region indicates the occupied states at $T = 0K$.* [82].

1.3.4 Magnetic interactions

In orthogonal orbitals[3], of equal energy, electrons remain unpaired if possible in order to minimize electron-electron repulsion. For the same reason these unpaired electrons try to align parallel, since due to the Pauli exclusion principle, electrons with the same spin keep away from each other better than those of opposite spin, thus minimizing the Coulomb repulsion. The application of this guideline for atoms and molecules is known as Hund's rule, and can lead to quite high spin states and atomic moments. In Mn^{2+} for example, applying Hund's rule leads to the alignment of the five unpaired electrons to give the high spin $S = 5/2$ in the $3d$ level. Many materials that contain atoms with a net magnetic moment, show some type of spontaneous magnetic ordering below a certain transition temperature. A material is called ferromagnetic when the moments are aligned parallel to each other, and the transition temperature is then called the Curie Temperature T_C . For such a spontaneous ordering to take place, one needs a coupling or interaction between these moments, as the classical dipole interaction is typically not strong enough to provide the normal ordering mechanism.

[3]Orbitals with different orbital quantum numbers

Exchange interactions

There are several origins for the interactions between the magnetic moments that can lead to a long-range ordering of the unpaired spins, called exchange interactions. The most common exchange interactions are schematically illustrated in Fig. 1.18.

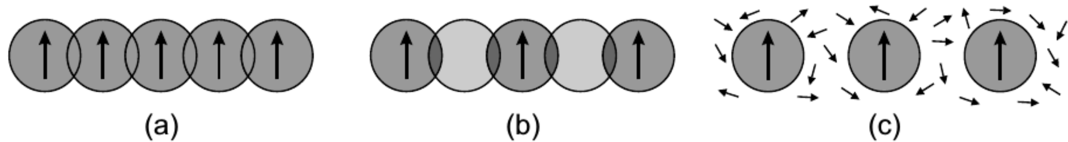

Figure 1.18: *Schematic illustration of (a) direct exchange, in which the magnetic ions interact through their overlapping charge distributions; (b) superexchange, where the interaction takes place via an intermediate non-magnetic ion; and (c) indirect exchange, in which the interaction is mediated by interactions with the charge carriers.* [75]

- Direct exchange occurs when there is direct overlap of the wave functions of electrons associated with nearest-neighbour magnetic atoms. This direct exchange can also be understood intuitively in terms of the Pauli exclusion principle and the Coulomb repulsion of alike charges, since the Coulomb repulsion, and thus the associated energy, will be lower if the electron spins of the neighbouring atoms are aligned parallel, because the exclusion principle then ensures their spatial separation. In diluted magnetic semiconductors the distance between the magnetic impurities is typically too large for the direct exchange mechanism to be relevant.
- Superexchange is a an indirect exchange mechanism, that describes the interaction of magnetic cations via an intermediate non-magnetic anion. In the case of II-VI and III-V diluted magnetic semiconductors, the superexchange results from the spin dependent hybridization between anion p and Mn d states and leads to a short-range antiferromagnetic (AF) coupling among the Mn moments. In the absence of holes, Mn-based II-VI and III-V DMS are indeed found to be antiferromagnets [47].
- When the direct overlap of the magnetic atoms is small, they are also able to interact through indirect exchange interactions which are mediated by the charge carriers. This indirect exchange can occur through several mechanisms such as the RKKY [52] interaction, the double exchange or the Zener mechanism. In diluted magnetic semiconductors it is exactly this indirect exchange which will lead to the ferromagnetism that can be observed in compounds like $Ga_{1-x}Mn_xAs$.

Hole mediated ferromagnetism

Several experimental results indicate that the ferromagnetic interaction in diluted magnetic semiconductors is mediated by the charge carriers, which are in most cases valence band holes. Ferromagnetic ordering in II-VI DMS for instance, can only be obtained with sufficient p-type doping [50], indicating that the antiferromagnetic exchange in these samples can be overcompensated by ferromagnetic interactions mediated by band holes. A similar phenomenon is observed in III-V DMS, since the magnetic interaction among Mn has been shown to be antiferromagnetic

in n-type $In_{1-x}Mn_xAs$[83] and in fully carrier compensated $Ga_{1-x}Mn_xAs$ using Sn as a donor, indicating the critical role of the holes for the magnetic coupling. The carrier-induced nature of the ferromagnetic state in III-V DMS has been compellingly demonstrated by field-effect experiments on $In_{1-x}Mn_xAs$[84], where the carrier concentration was tuned by a gate and the critical temperature was modified accordingly. The hole mediated origin of the ferromagnetism in $Ga_{1-x}Mn_xAs$ is further evidenced by the correlation between its transport and magnetic properties.

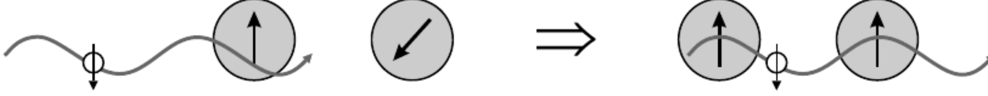

Figure 1.19: Schematic illustration of the hole mediated exchange interaction in diluted magnetic semiconductors. A long range ferromagnetic interaction of the Mn spins results from a strong anti-ferromagnetic coupling of the itinerant or weakly bound holes tothe localized spins. [47]

The ferromagnetic properties of diluted magnetic semiconductors result from the presence of a spin-dependent interaction between the electrons or holes in the sp bands of the semiconductor host and those residing on the d shells of the magnetic impurities[47], as illustrated schematically in Fig. 1.19. This interaction assumes a form of the Heisenberg exchange coupling,

$$H_{ex} = -J_{ex}\hat{s}\cdot\hat{S}, \tag{1.16}$$

where J_{ex} describes the strength of the interaction between the carrier spin $\hat{s}$ and the transition-metal spin $\hat{S}$. If J_{ex} is positive then the lowest energy state corresponds to a parallel spin alignment, while an antiferromagnetic alignment is favoured when J_{ex} is negative. In $Ga_{1-x}Mn_xAs$, the hybridization of the valence band holes with p-orbital character and the Mn d states results in spin-dependent interaction, the so-called kinetic exchange, which is characterized by a rather large exchange energy $J_{pd} \sim -1\text{eV}$[47]. The negative sign of J_{pd} reflects an antiferromagnetic coupling between the hole spin and the localized Mn spin. These $sp-d$ exchange couplings give rise to a spin-splitting of the bands proportional to the sample magnetization.

The antiferromagnetic coupling between the hole spin and the localized Mn spin leads to a long range ferromagnetic coupling between neighbouring Mn spins, see Fig. 1.19, which eventually results in a ferromagnetic state at low temperatures. In principle various mechanisms for the hole mediated exchange coupling in $Ga_{1-x}Mn_xAs$ are possible:

1.3.5 Theoretical models

In this section a brief overview is given of theoretical models that describes the origin of the ferromagnetism observed in $Ga_{1-x}Mn_xAs$. The theoretical modelling of diluted magnetic semiconductors takes starting point from the effective Hamiltonians containing experimentally determined parameters. The latter models are semi-phenomenological, as they assert, rather then derive, some key features of the material, such as the localized nature of the Mn d-orbital mo-

ments and the $p-d$ hybridization parametrized by an effective exchange constant J_{pd}. The effective magnetic Hamiltonian in these models is also known as the kinetic-exchange interaction, given by

$$H_{k-e} = J_{pd} \sum_i \int d^3 r \delta(\mathbf{r} - \mathbf{R}_i) \hat{S}_i \cdot \hat{s}(\mathbf{r}) \quad (1.17)$$

where $\hat{S}_i$ is the Mn spin at site $\mathbf{R}_i$, $\hat{s}$ is the spin of the carrier at site $\mathbf{r}$ and $J_{pd} > 0$ is the antiferromagnetic $p-d$ exchange constant. The sum over i goes over all the Mn sites in the GaAs lattice, and the delta function reflects the short range character of the interaction. This Hamiltonian is a well-known interaction Hamiltonian in condensed mater physics.

Although it is generally accepted that the ferromagnetic coupling between the local moments of the Mn ions in $Ga_{1-x}Mn_xAs$ is mediated by holes in the semiconductor valence band, the electronic nature of these holes is still a somewhat controversial issue. The ferromagnetism in $Ga_{1-x}Mn_xAs$ and other diluted magnetic semiconductors is often discussed using one or the other of two extreme models, which consider weakly disordered holes with an itinerant character residing in the valence band, and localized holes residing in an impurity band, respectively. The key approximation of the first approach is that disorder in the magnetically doped semiconductor is either ignored or treated perturbatively, while the second approach assumes that the holes are strongly localized in approximately hydrogenic wave-functions bound to Mn acceptors. In the latter case the holes reside in an impurity band, and, as discussed earlier, this picture is expected to be valid in the low density regime, where the resistivity shows insulating behaviour. At higher Mn densities and sufficiently large hole concentrations, it is expected that the impurity band merges with the valence band, so that the holes will likely reside in extended valence band states. However, some authors question the presence of extended valence band holes, even at more elevated Mn contents, and suggest that the $Ga_{1-x}Mn_xAs$ that show "metallic" behaviour at low temperatures may very well also be insulating at $T = 0$ K[85].

1.4 Optical Reversal of Magnetization

In this section we review the effect of light on magnetization when the photon energy is larger the semiconductor gap. In this case, the absorbed photons are real, whereas in our theoretical proposal the absorbed photons are virtual as the photon energy is smaller than the gap.

The impact of the laser pulse on a ferromagnetic $Ga_{1-x}Mn_xAs$ sample, with the photon energy exceeding the energy of the band gap $E_g = 1.42$ eV leads to an instant generation of the electron-hole pairs, where the concentration of the photon induced holes δn_h and electrons δn_e is equal. The scattering processes among the carriers build up a hot carrier Fermi-Dirac distribution on the sub-picosecond time scale[86]. Subsequently, the carriers recombine nonradiative at the high concentration of non-radiative recombination points caused by the low-temperature growth by MBE which increases the density of phonons due to the carrier-phonon interactions[86]. The initial carrier energy is thus transferred to the lattice, resulting into a local increase of the temperature within a few picoseconds[87,88]. The accumulated heat than diffuses from the illumi-

nated area towards the equilibrium conditions on the time scale of hundreds of picoseconds [89]. The temperature raise time can be obtained directly from differential reflectivity measurements $\Delta R/R$ that provide information about the photo-injected carrier concentration and life-time, see Fig. 1.20(a) [90]. The schematic picture of the temperature increase δT is depicted in Fig. 1.20(b).

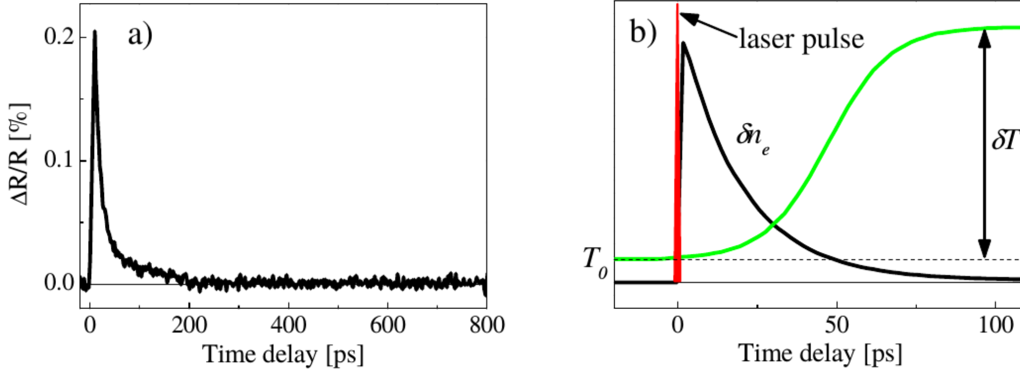

Figure 1.20: *a) Dynamics of the pump pulse-induced change of the sample reflectivity measured for a ferromagnetic $Ga_{1-x}Mn_xAs$ sample with 3% Mn doping and the pump intensity $I = 42\mu Jcm^{-2}$. The reflectivity dynamics provide the information about the laser-induced carrier concentration, amplitude of the $\Delta R/R$ and lifetime, defined as a time where the reflectivity amplitude decreases to $1/e$. b) Schematic illustration of the laser-induced change of the electron concentration δn_e and the subsequent temperature increase δT from the equilibrium temperature after impact of the femtosecond laser pulse. The dynamics of δn_e is obtained from the measured transient reflectivity data shown in a) where the corresponding lifetime is ~ 20 ps.* [90]

1.4.1 Non-thermal origin

The non-thermal processes that lead to magnetization precession are caused by the photo-induced carriers and can be divided, regarding the polarization of the excitation light, into two groups. The polarization independent and the polarization dependent ones. In the later ones, the circularly polarized light generates carriers with the defined spin orientation [91] and the subsequent magnetization precession is caused by a transfer of the spin angular momentum from the photo-carriers to the magnetization. This effect, known as the optical spin transfer torque (OSST), was theoretically predicted several years ago [92], but it was experimentally observed recently by Nemec et al. [93]. On the other hand, the polarization independent processes can be observed for any polarization of light[4]. In this case, the magnetization precession occurs as a result of the carrier spin polarization caused by the relativistic spin-orbit coupling (SOC) among the photo-induced carriers in the spin-split energy band. The effect is called the optical spin-orbit torque (OSOT) and was for the first time ever observed by Tesarova et al. [89]. Both of these non-thermal processes are described in more detail in the following sections.

[4] Also for the linearly polarized light

Optical spin-orbit torque

The current induced spin-orbit torques (SOT), that were recently observed in $Ga_{1-x}Mn_xAs$, opened a new possibilities for further technological development, such as the extension of the operational capabilities in the electronic devices, or the unprecedented characterizing techniques in material research[94,95]. The OSOT is its optical analogue and it enables studying the magnetization-related phenomena on the time scales which are orders of magnitudes shorter than in the current induced SOT. This effect is based on the easy axis reorientation due to the optically induced change of the carrier concentration, holes in particular, since the electrons are weakly spin-orbit coupled[89]. However, the reorientation of the easy axis and the subsequent initial tilt of magnetization can be in the opposite direction than in the case of the thermal mechanism, where the easy axis rotates towards the [010] and the magnetization tilts towards [001] crystallographic directions, respectively. Distinction between magnetization dynamics, which can be determined from the analysis of magnetization real-space trajectory, represents a straightforward method how to distinguish between the thermal and the non-thermal origin of magnetization precession. Such a simplified picture of the non thermally induced oscillations of magnetization are in agreement with theoretical calculations, based on **k p** kinetic exchange Hamiltonian of the hole-concentration dependent easy axis position[96], but the detailed understanding of this effect requires more rigorous explanation, based on the SOC in the valance band.

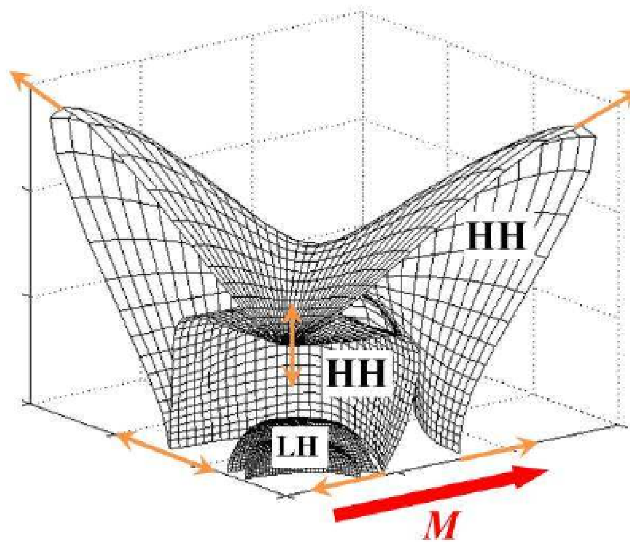

Figure 1.21: *Splitting of the valance band into four bands - the spin-split heavy (HH) and light (LH) holes bands, for ferromagnetic* $Ga_{1-x}Mn_xAs$*.*[97]

Figure 1.21 shows the a ferromagnetic $Ga_{1-x}Mn_xAs$ valance band, where the magnetization leads to the anisotropic splitting of the valance band into four bands - the spin-split heavy (HH) and light (LH) holes bands, respectively[97]. The SOC causes the change of the expected spin orientation along the top of the Fermi surface, which is essential for the occurrence of the magnetization torque and can be described as following. The impact of the linearly polarized laser

light induces a non-equilibrium hole population. Since the angular momentum of light is zero, there is no momentum that could be transferred into the system, so the excited holes are not spin polarized. However, the subsequent relaxation towards the spin-split Fermi sea of the equilibrium holes produces a non-equilibrium spin polarization, which is misaligned with the magnetization orientation. This photo-hole polarization can be perceived as an effective magnetic field that exerts a torque on the magnetization via the kinetic exchange coupling and leads to magnetization precession. It is important to note that in the case of no SOC, the only polarization that the holes could acquire would be parallel with magnetization orientation, which would exclude the existence of the torque. Despite the relatively simple physical origin of the OSOT, its quantitative description, involving the estimate of the hole polarization, is a rather challenging problem.

Optical spin-transfer torque

The optical spin-transfer torque (OSTT) represents another non-thermal effect responsible for the magnetization dynamics after the impact of the laser light. Similarly to the OSOT, the magnetization oscillations are caused by the spin-momentum transfer from the carriers to the magnetization via the exchange coupling. The main difference between these two effects is that in the case of OSTT, the carriers acquire their spin polarization directly from the circularly polarized light and thus no SOC is needed for observing this effect.[93]

The circularly polarized light generates the spin-polarized carriers, $\delta n_e = \delta n_h < n_{h0}$, where the carrier spin orientation σ is parallel with the direction of the incident light and perpendicular to magnetization orientation in the case of typical, compressively strained $Ga_{1-x}Mn_xAs$ samples with the in-plane equilibrium position of M, see Fig. 1.22. The appearance of the OSTT is conditioned by the relatively long spin lifetime of the photo-injected carriers[93] and only the photo-electrons spin lifetime of ~ 10 ps, which is given mainly by the interaction with Mn moments and by the electron recombination time, is sufficient to exert a torque on magnetization. The spin lifetime of holes is dominated by the strong SOC and it is estimated to be $\sim 1-10$ fs[92] which is not enough to cause the OSTT[93], so holes will be omitted in further discussion. Right after the impact of the circularly polarized light, the orientation of the generated spins σ is given by the propagation direction and by helicity of the circular polarization. However, the exchange field produced by the Mn moment yields the electron spins precession around the magnetization vector M, with the precessing period ~ 100 fs[92]. As the electron spin lifetime highly exceeds this precession period, the spins precess many times before they relax. In this steady-state regime, the spin σ_0 is oriented in the plane of the sample, but perpendicular to M, and exerts a torque on the magnetization vector, which leads to the subsequent precession of magnetization. It is important to note, that the OSTT starts to act during the laser pulse impact when the electrons with a concentration δn_e are photo injected and fades away within the electron spin lifetime $\sim$ ps. However, the magnetization precession persists up to several nanoseconds. The influence of OSTT is, therefore, most clearly observable in the initial phase of the detected magneto-optical signal[93].

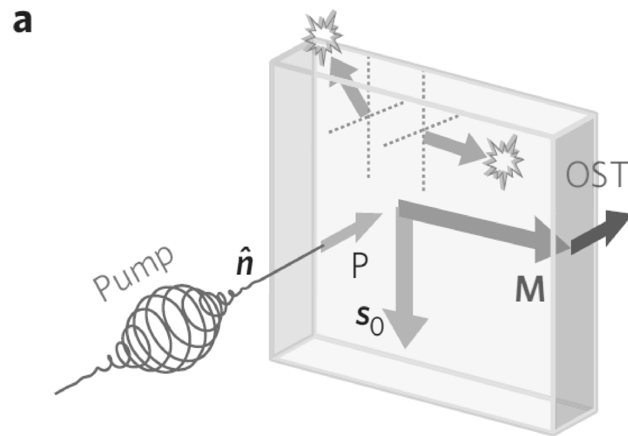

Figure 1.22: *Schematic illustration of the optical spin transfer torque. The circularly polarized light generates the carrier spin polarization, where the initial orientation of spins* $\boldsymbol{n}$ *is parallel with the incident light direction and perpendicular to magnetization* $\boldsymbol{M}$*. The steady-state component of the injected spin density* $\boldsymbol{s}_0$ *is oriented in the sample plane, perpendicular to* $\boldsymbol{M}$*, and exerts a torque on the magnetization vector* $\boldsymbol{M}$*.* [93]

Theoretical Background 2

2.1 Junction Hamilitonian

In the following section, will the model Hamiltonian be introduced to describe the interaction between a SC-FM-SC junction and an optical field. For further evaluation is the Heisenberg equation of motion been constructed for the system in terms of creation and destruction operators. The SC coupling to a optical field is transformed using the rotating wave approximation to eliminate the time dependency.

Consider the model Hamiltonian for an one-dimensional junction made of a thin single-domain ferromagnetic (FM) layer sandwiched between two identical direct-gap semiconductors (SC), as shown in 2.1. The FM layer, located at x = 0, disconnects the two SC sides, we consider the electronic transport through the one-dimensional junction. The material parameters determining the performance of this device include the gap of the semiconductor, the exchange split energy E_{ex} of the FM material, and the band mismatch E_0 between the SC material and FM material. As mentioned in chapter 1, a candidate system for the FM layer is a dilute magnetic semiconductor. When the electrons at the Fermi surface in the SC region is driven by electric field and move into the FM region, they will feel a potential barrier Δ_σ dependent on their spin states, and get scattered.

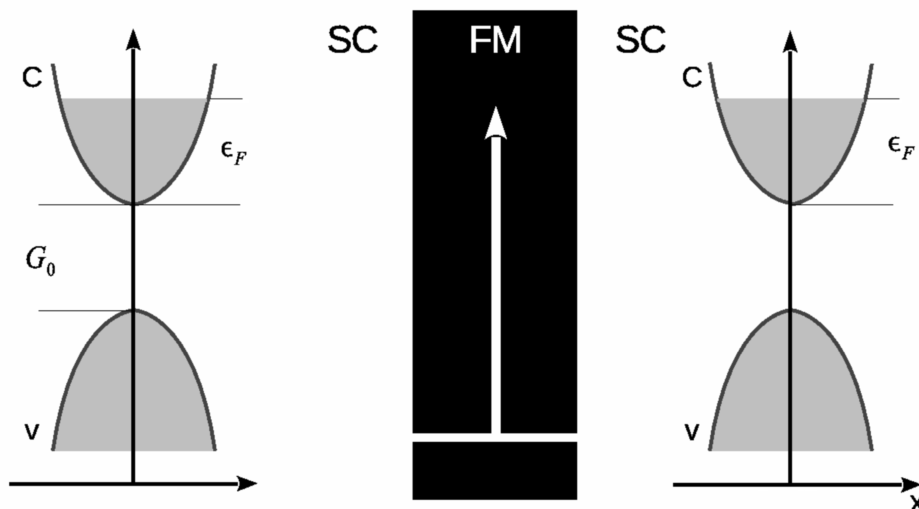

Figure 2.1: *Energy landscape of the semiconductor-nanomagnet-semiconductor junction.*

In many-particle physics, we usefully express the Hamiltonian in terms of an electronic field operator $\Psi_\sigma(x,t)$, where $\sigma = \uparrow, \downarrow$ is the electron spin. The field operator can be expanded in any convenient basis of single-particle states characterized by creation and annihilation operators of

electrons in the single-particle state. The Hamiltonian is expressed in the Heisenberg picture, i.e., the wavefunctions are independent of time, whereas the time dependence is carried by the operators. We describe the essential transport process in the ferromagnetic sandwiched structure by the following model Hamiltonian

$$H_{SC-FM-SC} = \sum_{\sigma} \int d^3x \hat{\Psi}^{\dagger}_{c,\sigma}(x) H^{kin}_{c} \hat{\Psi}_{c,\sigma}(x,t) + \hat{\Psi}^{\dagger}_{v,\sigma}(x) H^{kin}_{v} \hat{\Psi}_{v,\sigma}(x) + \hat{\Psi}^{\dagger}_{c,\sigma}(x) H^{FM}_{\sigma} \hat{\Psi}_{c,\sigma}(x,t) + \hat{\Psi}^{\dagger}_{v,\sigma}(x) H^{FM}_{\sigma} \hat{\Psi}_{v,\sigma}(x,t)$$
$$+ \hat{\Psi}^{\dagger}_{c,\sigma}(x) H^{opt}_{cv} \hat{\Psi}_{v,\sigma}(x) + \hat{\Psi}^{\dagger}_{v,\sigma}(x) H^{opt}_{vc} \hat{\Psi}_{c,\sigma}(x) \tag{2.1}$$

The Hamiltonian consists of following terms; first is the kinetic energy term H_b^{kin} where isotropic nondegenerate parabolic conduction and valence bands are assumed for electrons in the direct-gap semiconductor. The electron energies are evaluated in the effective-mass approximation and are, respectively,

$$H^{kin}_{c} = -\frac{\hbar^2}{2m}\frac{\partial^2}{\partial x^2} + \frac{G}{2} \tag{2.2}$$
$$H^{kin}_{v} = \frac{\hbar^2}{2m}\frac{\partial^2}{\partial x^2} - \frac{G}{2} \tag{2.3}$$

where G is the gap of the intrinsic semiconductor, m are the particle effective mass.
Second term describes the interaction between the conducting electron and localized d electrons within the ferromagnet

$$H^{FM}_{\sigma} = \delta(x)\,(\lambda_0 \pm \lambda_z \sigma_z) \tag{2.4}$$

where the parameters λ_0 and λ are determined from the device parameters E_0, E_{ex}, n_d, J as

$$\lambda_0 = \frac{E_0 n_d}{J\hbar} \tag{2.5}$$
$$\lambda = \frac{E_{ex} d}{J\hbar^2} \tag{2.6}$$

where E_0 are the band mismatch between the FM and SC material, E_{ex} is the exchange split energy of FM material, n_d is the number of d electrons and J is the number of spin polarized electrons.
Third term describes the interaction Hamiltonian between a coherent monochromatic classical field and the semiconductor electrons within the two bands expressed using second quantization where the electric field $\mathcal{E}(r,t)$ is assumed to have a simple exponential space dependency

$$H_{I,b} = \sum_{b\neq b'} \int d^3r \hat{\psi}^{\dagger}_{b,\sigma}(r,t)(-er)\cdot \mathcal{E}(r,t)\hat{\psi}_{b',\sigma}(r,t) \tag{2.7}$$

$$\mathcal{E}(r,t) = \mathcal{E}(t)\frac{1}{2}\left(e^{iq\cdot r} + e^{-iq\cdot r}\right) \approx \mathcal{E}(t)\text{Neglection of space dependency}$$

$$= \sum_{b\neq b'} \int d^3r \hat{\psi}^{\dagger}_{b,\sigma}(r,t)(-er)\mathcal{E}(t)\hat{\psi}_{b',\sigma}(r,t)$$

$$= \sum_{b\neq b'} \int d^3r \hat{\psi}^{\dagger}_{b,\sigma}(r,t)(-er)\mathcal{E}(t)\hat{\psi}_{b',\sigma}(r,t)$$

$$\simeq -\sum_{b\neq b'} \delta_{k,k'} d_{b,b'}$$

$$H_{I,b} = -\sum_{b\neq b'} d_{b,b'}\mathcal{E}(t) \tag{2.8}$$

where the dipole approximation $q \to 0$ and the definition of $d_{b,b'}$ as the projection of the dipole in the direction of the field. The interaction Hamiltonian, shows how the applied field causes transitions of electrons between the two bands. We have further restrict the treatment to the optical transitions between the valence and conduction bands of the semiconductor (two-band approximation) and suppressing of the spin-flip process.

$$H^{opt}_{cv} = d^*_{cv}\mathcal{E}(t) \tag{2.9}$$

$$H^{opt}_{vc} = d_{cv}\mathcal{E}^*(t) \tag{2.10}$$

Here, d is the operator for the electric dipole moment and it's assumed that the homogeneous electromagnetic field is polarized in x-direction.

2.1.1 Heisenberg equation of motion

By using the Heisenberg transformation the spin-dependent Hamiltonian $H_{SC-FM-SC}$ 2.11 is transformed into the Heisenberg picture, eq. 2.13 and 2.14,

$$\begin{aligned} H_{SC-FM-SC} = \sum_{\sigma} \int d^3x \hat{\Psi}^{\dagger}_{c,\sigma}(x) &\left(-\frac{\hbar^2}{2m}\frac{\partial^2}{\partial x^2} + \frac{G}{2} + \delta(x)\lambda_0 + \delta(x)\lambda_z\sigma_z\right)\hat{\Psi}_{c,\sigma}(x) \\ &+ \hat{\Psi}^{\dagger}_{v,\sigma}(x)\left(\frac{\hbar^2}{2m}\frac{\partial^2}{\partial x^2} - \frac{G}{2} + \delta(x)\lambda_0 + \delta(x)\lambda_z\sigma_z\right)\hat{\Psi}_{v,\sigma}(x) \\ &+ \hat{\Psi}^{\dagger}_{c,\sigma}(x)d^*_{cv}\mathcal{E}(t)\hat{\Psi}_{v,\sigma}(x) \\ &+ \hat{\Psi}^{\dagger}_{v,\sigma}(x)d_{cv}\mathcal{E}^*(t)\hat{\Psi}_{c,\sigma}(x) \end{aligned} \tag{2.11}$$

in terms of the creation $\hat{\Psi}^{\dagger}_{b,\sigma}$ and destruction $\hat{\Psi}_{b,\sigma}$ operators for an electron at point x in the conduction- or valences band with spin σ. These fermion operators obey the anti-commutation relations

$$\{\hat{\Psi}_{b,\sigma}(x), \hat{\Psi}^{\dagger}_{b',\sigma'}(x')\} = \delta_{b,b'}\delta_{\sigma,\sigma'}\delta(x-x') \qquad \{\hat{\Psi}_{b,\sigma}(x), \hat{\Psi}_{b',\sigma'}(x')\} = 0 \qquad \{\hat{\Psi}^{\dagger}_{b,\sigma}(x), \hat{\Psi}^{\dagger}_{b',\sigma'}(x')\} = 0 \tag{2.12}$$

Let us first derive the Heisenberg equation of motion for the SC-FM-SC junction,

$$\frac{\partial}{\partial t}\hat{\Psi}_{v,\sigma}(\mathbf{r},t) = \frac{i}{\hbar}\left[H, \hat{\Psi}_{v,\sigma}(\mathbf{r},t)\right] \Leftrightarrow -i\hbar\frac{\partial}{\partial t}\hat{\Psi}_{v,\sigma}(\mathbf{r},t) = \left[H, \hat{\Psi}_{v,\sigma}(\mathbf{r},t)\right] \tag{2.13}$$

$$\frac{\partial}{\partial t}\hat{\Psi}_{c,\sigma}(\mathbf{r},t) = \frac{i}{\hbar}\left[H, \hat{\Psi}_{c,\sigma}(\mathbf{r},t)\right] \Leftrightarrow -i\hbar\frac{\partial}{\partial t}\hat{\Psi}_{c,\sigma}(\mathbf{r},t) = \left[H, \hat{\Psi}_{c,\sigma}(\mathbf{r},t)\right] \tag{2.14}$$

The conversion to the Heisenberg equation have two immediate consequences of great importance. First, observables that commute with the Hamiltonian are constants of motion. Second, any constant of motion can be diagonalized simultaneously with the Hamiltonian they are simultaneous eigenstates. The Hamiltonian and a set of constants of motion can be diagonalized simultaneously provided that all these constants of motion commute with each other.

Heisenberg equation of motion for the SC-FM-SC junction where the spin σ represent both spin-up and spin-down

$$i\hbar\frac{\partial}{\partial t}\hat{\Psi}_{c,\uparrow}(x) = \left(-\frac{\hbar^2}{2m}\frac{\partial^2}{\partial x^2} + \frac{G}{2} + \delta(x)\left(\lambda_0 + \lambda_z\right)\right)\hat{\Psi}_{c,\uparrow}(x) + d^*_{cv}\mathcal{E}(t)\hat{\Psi}_{v,\uparrow}(x) \tag{2.15}$$

$$i\hbar\frac{\partial}{\partial t}\hat{\Psi}_{c,\downarrow}(x) = \left(-\frac{\hbar^2}{2m}\frac{\partial^2}{\partial x^2} + \frac{G}{2} + \delta(x)\left(\lambda_0 - \lambda_z\right)\right)\hat{\Psi}_{c,\downarrow}(x) + d^*_{cv}\mathcal{E}(t)\hat{\Psi}_{v,\downarrow}(x) \tag{2.16}$$

$$i\hbar\frac{\partial}{\partial t}\hat{\Psi}_{v,\uparrow}(x) = \left(\frac{\hbar^2}{2m}\frac{\partial^2}{\partial x^2} - \frac{G}{2} + \delta(x)\left(\lambda_0 + \lambda_z\right)\right)\hat{\Psi}_{v,\uparrow}(x) + d_{cv}\mathcal{E}^*(t)\hat{\Psi}_{c,\uparrow}(x) \tag{2.17}$$

$$i\hbar\frac{\partial}{\partial t}\hat{\Psi}_{v,\downarrow}(x) = \left(\frac{\hbar^2}{2m}\frac{\partial^2}{\partial x^2} - \frac{G}{2} + \delta(x)\left(\lambda_0 - \lambda_z\right)\right)\hat{\Psi}_{v,\downarrow}(x) + d_{cv}\mathcal{E}^*(t)\hat{\Psi}_{c,\downarrow}(x) \tag{2.18}$$

Matrix represents of the four Heisenberg equation of motion 2.15-2.18, demonstrates that the matrix will control the dynamic behaviour of the system.

$$\begin{bmatrix} \left(-\frac{\hbar^2}{2m}\frac{\partial^2}{\partial x^2} + \frac{G}{2} + \delta(x)\left(\lambda_0 + \lambda_z\right)\right) & 0 & 0 & d^*_{cv}\mathcal{E}(t) \\ 0 & \left(-\frac{\hbar^2}{2m}\frac{\partial^2}{\partial x^2} + \frac{G}{2} + \delta(x)\left(\lambda_0 - \lambda_z\right)\right) & d^*_{cv}\mathcal{E}(t) & 0 \\ 0 & d_{cv}\mathcal{E}^*(t) & \left(\frac{\hbar^2}{2m}\frac{\partial^2}{\partial x^2} - \frac{G}{2} + \delta(x)\left(\lambda_0 + \lambda_z\right)\right) & 0 \\ d_{cv}\mathcal{E}^*(t) & 0 & 0 & \left(\frac{\hbar^2}{2m}\frac{\partial^2}{\partial x^2} - \frac{G}{2} + \delta(x)\left(\lambda_0 - \lambda_z\right)\right) \end{bmatrix} \begin{pmatrix} \hat{\Psi}_{c,\uparrow}(x) \\ \hat{\Psi}_{c,\downarrow}(x) \\ \hat{\Psi}_{v,\uparrow}(x) \\ \hat{\Psi}_{v,\downarrow}(x) \end{pmatrix} = i\hbar\frac{\partial}{\partial t}\begin{pmatrix} \hat{\Psi}_{c,\uparrow}(x) \\ \hat{\Psi}_{c,\downarrow}(x) \\ \hat{\Psi}_{v,\uparrow}(x) \\ \hat{\Psi}_{v,\downarrow}(x) \end{pmatrix} \tag{2.19}$$

2.2 Gauge transformation of the Optical field

Let us define the quasiparticle amplitudes $u_\sigma(x)$ and $v_\sigma(x)$ as

$$u_\sigma(x) = \langle\Psi_0|\hat{\Psi}_{c,\sigma}(x)|\Psi_1\rangle \tag{2.20}$$

$$v_\sigma(x) = \langle\Psi_0|\hat{\Psi}_{v,\sigma}(x)|\Psi_1\rangle \tag{2.21}$$

where $|\Psi_0\rangle$ and $|\Psi_1\rangle$ are respectively the ground state of the system and the excited state with one quasiparticle added to the system. The quantities $u_\sigma(x)$ and $v_\sigma(x)$ are the probability amplitudes to find the quasiparticle (a free electron or hole) with spin σ at position x in the conduction and valence band, respectively.

The equations of motion for electron like quasiparticles are

$$i\hbar\frac{\partial}{\partial t}u_{\uparrow}(x) = \left(-\frac{\hbar^2}{2m}\frac{\partial^2}{\partial x^2} + \frac{G}{2} + \delta(x)\left(\lambda_0+\lambda_z\right)\right)u_{\uparrow}(x) + d_{cv}^{*}\mathcal{E}(t)v_{\uparrow}(x) \tag{2.22}$$

$$i\hbar\frac{\partial}{\partial t}u_{\downarrow}(x) = \left(-\frac{\hbar^2}{2m}\frac{\partial^2}{\partial x^2} + \frac{G}{2} + \delta(x)\left(\lambda_0-\lambda_z\right)\right)u_{\downarrow}(x) + d_{cv}^{*}\mathcal{E}(t)v_{\downarrow}(x) \tag{2.23}$$

$$i\hbar\frac{\partial}{\partial t}v_{\uparrow}(x) = \left(\frac{\hbar^2}{2m}\frac{\partial^2}{\partial x^2} - \frac{G}{2} + \delta(x)\left(\lambda_0+\lambda_z\right)\right)v_{\uparrow}(x) + d_{cv}\mathcal{E}^{*}(t)u_{\uparrow}(x) \tag{2.24}$$

$$i\hbar\frac{\partial}{\partial t}v_{\downarrow}(x) = \left(\frac{\hbar^2}{2m}\frac{\partial^2}{\partial x^2} - \frac{G}{2} + \delta(x)\left(\lambda_0-\lambda_z\right)\right)v_{\downarrow}(x) + d_{cv}\mathcal{E}^{*}(t)u_{\downarrow}(x) \tag{2.25}$$

$d_{cv} = d_{vc}^{*}$ is the interband dipole matrix element and $\mathcal{E}^{*}(t) = \mathcal{E}(t) = \mathcal{E}(\omega)exp(-i\omega t) + \mathcal{E}^{*}(\omega)exp(i\omega t)$ is the real classic optical field.

The Rotating wave approximation is used to reduced the optical field and thereby remove the time independences

$$i\hbar\frac{\partial}{\partial t}u_{\uparrow}(x) = \left(-\frac{\hbar^2}{2m}\frac{\partial^2}{\partial x^2} + \frac{G}{2} + \delta(x)\left(\lambda_0+\lambda_z\right)\right)u_{\uparrow}(x) + d_{cv}^{*}\mathcal{E}(\omega)e^{-i\omega t}v_{\uparrow}(x) \tag{2.26}$$

$$i\hbar\frac{\partial}{\partial t}u_{\downarrow}(x) = \left(-\frac{\hbar^2}{2m}\frac{\partial^2}{\partial x^2} + \frac{G}{2} + \delta(x)\left(\lambda_0-\lambda_z\right)\right)u_{\downarrow}(x) + d_{cv}^{*}\mathcal{E}(\omega)e^{-i\omega t}v_{\downarrow}(x) \tag{2.27}$$

$$i\hbar\frac{\partial}{\partial t}v_{\uparrow}(x) = \left(\frac{\hbar^2}{2m}\frac{\partial^2}{\partial x^2} - \frac{G}{2} + \delta(x)\left(\lambda_0+\lambda_z\right)\right)v_{\uparrow}(x) + d_{cv}\mathcal{E}^{*}(\omega)e^{i\omega t}u_{\uparrow}(x) \tag{2.28}$$

$$i\hbar\frac{\partial}{\partial t}v_{\downarrow}(x) = \left(\frac{\hbar^2}{2m}\frac{\partial^2}{\partial x^2} - \frac{G}{2} + \delta(x)\left(\lambda_0-\lambda_z\right)\right)v_{\downarrow}(x) + d_{cv}\mathcal{E}^{*}(\omega)e^{i\omega t}u_{\downarrow}(x) \tag{2.29}$$

Introduce the gauge transformation

$$u(x) \to u'(x) = u(x)e^{i\frac{\omega}{2}t} \tag{2.30}$$

$$v(x) \to v'(x) = v(x)e^{-i\frac{\omega}{2}t} \tag{2.31}$$

this transformation simply shifts the energies of the conduction and valence bands

$$i\hbar\frac{\partial}{\partial t}u'_{\uparrow}(x) = \left(-\frac{\hbar^2}{2m}\frac{\partial^2}{\partial x^2} + \frac{G}{2} - \frac{\hbar\omega}{2} + \delta(x)\left(\lambda_0+\lambda_z\right)\right)u'_{\uparrow}(x) + d_{cv}^{*}\mathcal{E}(\omega)v'_{\uparrow}(x) \tag{2.32}$$

$$i\hbar\frac{\partial}{\partial t}u'_{\downarrow}(x) = \left(-\frac{\hbar^2}{2m}\frac{\partial^2}{\partial x^2} + \frac{G}{2} - \frac{\hbar\omega}{2} + \delta(x)\left(\lambda_0-\lambda_z\right)\right)u'_{\downarrow}(x) + d_{cv}^{*}\mathcal{E}(\omega)v'_{\downarrow}(x) \tag{2.33}$$

$$i\hbar\frac{\partial}{\partial t}v'_{\uparrow}(x) = \left(\frac{\hbar^2}{2m}\frac{\partial^2}{\partial x^2} - \frac{G}{2} + \frac{\hbar\omega}{2} + \delta(x)\left(\lambda_0+\lambda_z\right)\right)v'_{\uparrow}(x) + d_{cv}\mathcal{E}^{*}(\omega)u'_{\uparrow}(x) \tag{2.34}$$

$$i\hbar\frac{\partial}{\partial t}v'_{\downarrow}(x) = \left(\frac{\hbar^2}{2m}\frac{\partial^2}{\partial x^2} - \frac{G}{2} + \frac{\hbar\omega}{2} + \delta(x)\left(\lambda_0-\lambda_z\right)\right)v'_{\downarrow}(x) + d_{cv}\mathcal{E}^{*}(\omega)u'_{\downarrow}(x) \tag{2.35}$$

which result in a chemical potential $-\hbar\omega/2$ for conduction electrons and $\hbar\omega/2$ for valence holes.

By writing $\frac{\tau}{2} = \frac{G}{2} - \frac{\hbar\omega}{2}$ as a detuning parameter the equations of motion takes the following form

$$\varepsilon u_{\uparrow}(x) = \left(-\frac{\hbar^2}{2m}\frac{\partial^2}{\partial x^2} + \frac{\tau}{2} + \delta(x)\left(\lambda_0 + \lambda_z\right)\right) u_{\uparrow}(x) + d_{cv}^{*}\mathcal{E}(\omega) v_{\uparrow}(x) \tag{2.36}$$

$$\varepsilon u_{\downarrow}(x) = \left(-\frac{\hbar^2}{2m}\frac{\partial^2}{\partial x^2} + \frac{\tau}{2} + \delta(x)\left(\lambda_0 - \lambda_z\right)\right) u_{\downarrow}(x) + d_{cv}^{*}\mathcal{E}(\omega) v_{\downarrow}(x) \tag{2.37}$$

$$\varepsilon v_{\uparrow}(x) = \left(\frac{\hbar^2}{2m}\frac{\partial^2}{\partial x^2} - \frac{\tau}{2} + \delta(x)\left(\lambda_0 + \lambda_z\right)\right) v_{\uparrow}(x) + d_{cv}\mathcal{E}^{*}(\omega) u_{\uparrow}(x) \tag{2.38}$$

$$\varepsilon v_{\downarrow}(x) = \left(\frac{\hbar^2}{2m}\frac{\partial^2}{\partial x^2} - \frac{\tau}{2} + \delta(x)\left(\lambda_0 - \lambda_z\right)\right) v_{\downarrow}(x) + d_{cv}\mathcal{E}^{*}(\omega) u_{\downarrow}(x) \tag{2.39}$$

The conduction and valence band amplitudes are shifted by the frequency ω of the interband transition back and forth between the two bands induced by the laser. For positive detuning $\tau = G - \hbar\omega > 0$, electron - hole pairs are virtual.

2.3 Solution Bulk Problem

In this section, will I describe the calculation of the bulk solution for a semiconductor for thereby to determine the coherent factors

Determined now a solution for the four equation expressed in terms of quasiparticles amplitudes u_σ and v_σ where it's assumed that the x, y and z- component for the total angular momentum is zero the magnetization is therefore also zero. Further it's assumed that no spin-flip processes is takes into account.

$$\begin{bmatrix} -\frac{\hbar^2}{2m}\frac{\partial^2}{\partial x^2} + \frac{G}{2} & d_{c,v}^{*}\mathcal{E}(\omega) \\ d_{c,v}\mathcal{E}^{*}(\omega) & \frac{\hbar^2}{2m}\frac{\partial^2}{\partial x^2} - \frac{G}{2} \end{bmatrix} \begin{pmatrix} u_\sigma(x) \\ v_\sigma(x) \end{pmatrix} = \varepsilon \begin{pmatrix} u_\sigma(x) \\ v_\sigma(x) \end{pmatrix} \tag{2.40}$$

The solution to the above equation of motion consist of four linear independent equations. Consider now an ansatz solution of the following form

$$\begin{pmatrix} u_\sigma(x) \\ v_\sigma(x) \end{pmatrix} = \begin{pmatrix} u_0 \\ v_0 \end{pmatrix} e^{ikx} \tag{2.41}$$

Solve the equation of motion for the initial state within the bulk semiconductor, no contribution from the delta potential originated from the nanomagnet $\delta(x)(\lambda_0 \pm \lambda) = 0$.

Consider an electron with a fix energy larger than zero $\varepsilon > 0$ and solve eq. 2.40 to obtain a real and an imaginary solution.
We start by evaluating the real solution corresponding to a travelling wave with are positive real wave vector k. The calculation is simplified by expressing the kinetic energy for an electron within the conduction band as $\varepsilon_c = \frac{\hbar^2 k^2}{2m} + \frac{G}{2}$ and $\varepsilon_v = \frac{-\hbar^2 k^2}{2m} - \frac{G}{2}$ for an electron within the valences band. Thereby, can the quadratic equation, eq. 2.40 be solved with respect to the eigenvalue for the equation of motion at the initial state ε

$$\begin{aligned}(\varepsilon-\varepsilon_c)(\varepsilon-\varepsilon_v) &= |d_{c,v}\mathcal{E}(\omega)|^2 \\ \varepsilon &= \frac{1}{2}(\varepsilon_c+\varepsilon_v) \pm \frac{1}{2}\sqrt{(\varepsilon_c-\varepsilon_v)^2+4|d_{c,v}\mathcal{E}(\omega)|^2}\end{aligned} \tag{2.42}$$

the equation is further simplified by evaluating the kinetic energy to $\varepsilon_c - \varepsilon_v = \frac{\hbar^2 k^2}{m}$, $\varepsilon_c + \varepsilon_v = 0$

$$\varepsilon^2 = \left(\frac{\hbar^2 k^2}{2m} + \frac{G}{2}\right)^2 + |d_{c,v}\mathcal{E}(\omega)|^2 \tag{2.43}$$

$$k^{\pm} = \pm\sqrt{\frac{2m}{\hbar^2}}\sqrt{-\frac{G}{2}+\sqrt{\varepsilon^2-|d_{c,v}\mathcal{E}(\omega)|^2}} \tag{2.44}$$

If the wave vector k characterises a travelling wave, it most be real, therefore following constrained on the energy must exist $\varepsilon^2 \geq |d_{c,v}\mathcal{E}(\omega)|^2 + \frac{G^2}{4}$. In contrast, the case with energies $\varepsilon^2 \leq |d_{c,v}\mathcal{E}(\omega)|^2 + \frac{G^2}{4}$ will the solutions acquire an imaginary part and a real part of the order $\pm\sqrt{\frac{mG}{\hbar^2}}$,

$$\varepsilon^2 = \left(\frac{\hbar^2 q^2}{2m} - \frac{G}{2}\right)^2 + |d_{c,v}\mathcal{E}(\omega)|^2 \tag{2.45}$$

$$q^{\pm} = \pm\sqrt{\frac{2m}{\hbar^2}}\sqrt{\frac{G}{2}+\sqrt{\varepsilon^2-|d_{c,v}\mathcal{E}(\omega)|^2}} \tag{2.46}$$

$q^{\pm}$ describe a standing exponential decreasing wave.
The optical field in equation 2.40 enters with either a plus or minus sign, but the sign of the optical field is insignificant because the optical field only enters as the absolute square.

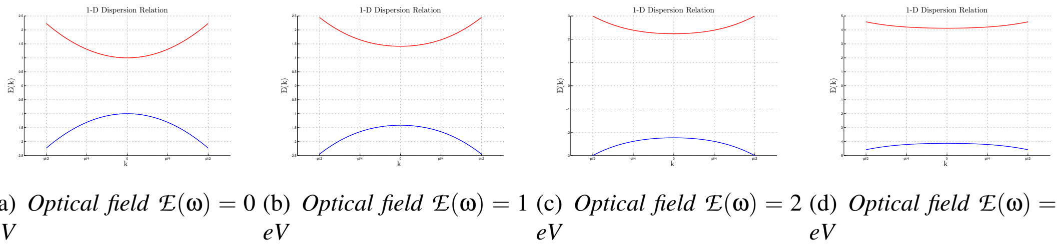

(a) *Optical field* $\mathcal{E}(\omega) = 0$ *eV* (b) *Optical field* $\mathcal{E}(\omega) = 1$ *eV* (c) *Optical field* $\mathcal{E}(\omega) = 2$ *eV* (d) *Optical field* $\mathcal{E}(\omega) = 4$ *eV*

Figure 2.2: *Energies and wave vectors are connected through the dispersion relation, which shows a parabolic relation, similar to the free electron case. Conduction and valences band are plotted for energies larger than* $\varepsilon^2 \geq G^2/4 + |d_{c,v}\mathcal{E}(\omega)|^2$.

From equation 2.44 and 2.46 can it be observed that the semiconductor gap opens when an optical field are applied.
The coherent factors u_0 and v_0 describe the possibility for quasi-particle like excitation with energy ε and momentum k in the conduction or valence band. The coherent factors have further to obtained the normalization condition to insure that the quasi-particle will be located at a point $|u_0|^2 + |v_0|^2 = 1$

$$\left(\frac{\hbar^2k^2}{2m}+\frac{G}{2}\right)u_0+d^*_{c,v}\mathcal{E}(\omega)v_0=\varepsilon u_0 \qquad \left(\frac{\hbar^2k^2}{2m}+\frac{G}{2}\right)^2=\varepsilon-|d_{c,v}\mathcal{E}(\omega)|^2$$

$$\left(\frac{-\hbar^2k^2}{2m}-\frac{G}{2}\right)v_0+d_{c,v}\mathcal{E}^*(\omega)u_0=\varepsilon v_0 \qquad \left(\frac{-\hbar^2k^2}{2m}-\frac{G}{2}\right)^2=\varepsilon-|d_{c,v}\mathcal{E}(\omega)|^2$$

$$u_0=\sqrt{\frac{1}{2}\left(1+\sqrt{\frac{\varepsilon^2-|d_{c,v}\mathcal{E}(\omega)|^2}{\varepsilon^2}}\right)}=\sqrt{\frac{d_{c,v}\mathcal{E}(\omega)}{2\varepsilon}}e^{\frac{1}{2}\cosh^{-1}\left(\frac{\varepsilon}{d_{c,v}\mathcal{E}(\omega)}\right)} \tag{2.47}$$

$$v_0=\sqrt{\frac{1}{2}\left(1-\sqrt{\frac{\varepsilon^2-|d_{c,v}\mathcal{E}(\omega)|^2}{\varepsilon^2}}\right)}=\sqrt{\frac{d_{c,v}\mathcal{E}(\omega)}{2\varepsilon}}e^{-\frac{1}{2}\cosh^{-1}\left(\frac{\varepsilon}{d_{c,v}\mathcal{E}(\omega)}\right)} \tag{2.48}$$

For energies lower than $\varepsilon^2<|d_{c,v}\mathcal{E}(\omega)|^2+\frac{G^2}{4}$ the coherent factors $\overline{u}_0$ and $\overline{v}_0$ correspond to a hole-like excitation with the same energy ε but with an imaginary momentum q

$$\left(-\frac{\hbar^2q^2}{2m}+\frac{G}{2}\right)\overline{u}_0+d^*_{c,v}\mathcal{E}(\omega)\overline{v}_0=\varepsilon\overline{u}_0 \qquad \left(\frac{-\hbar^2q^2}{2m}+\frac{G}{2}\right)^2=\varepsilon-|d_{c,v}\mathcal{E}(\omega)|^2$$

$$\left(\frac{\hbar^2q^2}{2m}-\frac{G}{2}\right)\overline{v}_0+d_{c,v}\mathcal{E}(\omega)\overline{u}_0=\varepsilon\overline{v}_0 \qquad \left(\frac{\hbar^2q^2}{2m}-\frac{G}{2}\right)^2=\varepsilon-|d_{c,v}\mathcal{E}(\omega)|^2$$

$$\overline{u}_0=\sqrt{\frac{1}{2}\left(1-i\sqrt{\frac{|d_{c,v}\mathcal{E}(\omega)|^2-\varepsilon^2}{\varepsilon^2}}\right)}=\sqrt{\frac{d_{c,v}\mathcal{E}(\omega)}{2\varepsilon}}e^{\frac{i}{2}\cos^{-1}\left(\frac{\varepsilon}{d_{c,v}\mathcal{E}(\omega)}\right)} \tag{2.49}$$

$$\overline{v}_0=\sqrt{\frac{1}{2}\left(1+i\sqrt{\frac{|d_{c,v}\mathcal{E}(\omega)|^2-\varepsilon^2}{\varepsilon^2}}\right)}=\sqrt{\frac{d_{c,v}\mathcal{E}(\omega)}{2\varepsilon}}e^{-\frac{i}{2}\cos^{-1}\left(\frac{\varepsilon}{d_{c,v}\mathcal{E}(\omega)}\right)} \tag{2.50}$$

2.4 Solution of the Scattering Problem

In this section, will I describe the calculation of the spin depended reflection and transmission coefficients for a semiconductor ferromagnet junction. I will start by considering the quasi-particle wavefunction on both side of the ferromagnet and thereby use the appropriated boundary condition to obtain a set of linearly independent equations. Those equation can thereby be used to obtaining the eight reflection and transmission coefficients.

2.4.1 Basic Considerations

When a thin magnetic material is placed between two identical direct-gap semi-infinite semiconductor, and a spin polarized current flows through the junction under the influence of an intense monocromatic laser beam. Will the properties of both materials change dramatically. Here we focus on how scattering states in the semiconductor are affected by the laser beam.
Consider a flow of electrons approaching from right SC_1, cf. Fig. 2.3 when the electrons interacts with the interface, it is subjected with various probabilities to four distinct processes: either by been reflected back into the SC_1 region, left moving quasiparticles, or transmitted into the SC_2 region, right moving particles. Additional to the plane wave solutions, can also exist two evanescent waves characterized by an imaginary wave vector, both types of solutions are fully

accepted solution for the system.

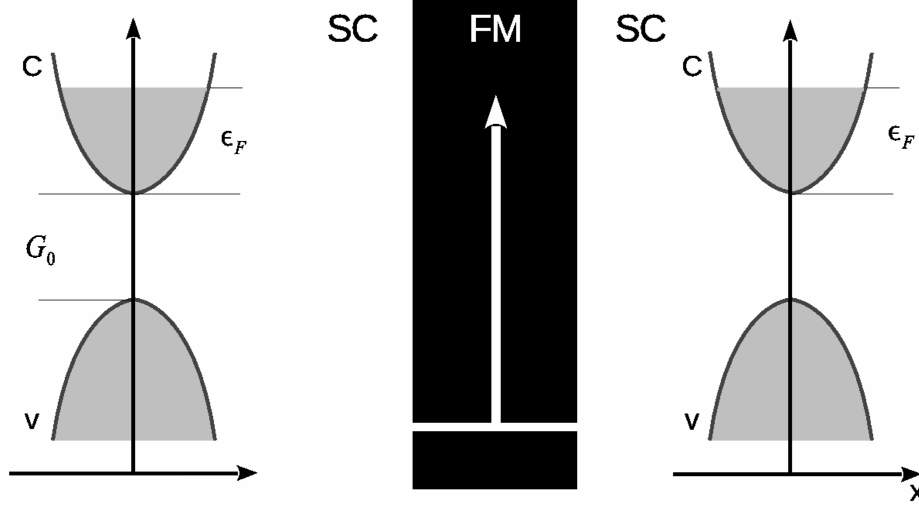

Figure 2.3: Scattering of quasiparticles for a spin depended junction located at $x = 0$ with barrier strength defined by Z_σ along z. The transport and scattering properties is obtained by consider a flow of spin polarized quasiparticles through the barrier, the electrons is originate from an exciton condensate.

The complete solution to the spin-dependent two-band system consist of two travelling plan waves within the conduction band $\pm k$ and two standing evanescent waves meanly within the valence band $\pm q$.
The incoming quaisparticle $\Psi_{in}(x)$ is a plane wave moving from left to right with spin polarized along the direction $\mathbf{P}_{\text{in}} \equiv (\sin\vartheta\cos\varphi, \sin\vartheta\sin\varphi, \cos\vartheta)$:

$$\Psi_{\text{in}}(x) = \begin{pmatrix} \cos(\vartheta/2)e^{-i\varphi/2}u_0 \\ \cos(\vartheta/2)e^{-i\varphi/2}v_0 \\ \sin(\vartheta/2)e^{i\varphi/2}u_0 \\ \sin(\vartheta/2)e^{i\varphi/2}v_0 \end{pmatrix} e^{ikx} \qquad x < 0. \tag{2.51}$$

A distinctive feature of the two-band model, in contrast with the one-band picture, is that the evanescent wave localized at the interface adds to usual travelling waves to make the elastic-scattering basis complete. In the expression of both reflected,

$$\Psi_{\text{refl}}(x) = \begin{pmatrix} \cos(\vartheta/2)e^{-i\varphi/2}a_\uparrow v_0^* \\ \cos(\vartheta/2)e^{-i\varphi/2}a_\uparrow u_0^* \\ \sin(\vartheta/2)e^{i\varphi/2}a_\downarrow v_0^* \\ \sin(\vartheta/2)e^{i\varphi/2}a_\downarrow u_0^* \end{pmatrix} e^{qx} \quad + \quad \begin{pmatrix} \cos(\vartheta/2)e^{-i\varphi/2}r_\uparrow u_0 \\ \cos(\vartheta/2)e^{-i\varphi/2}r_\uparrow v_0 \\ \sin(\vartheta/2)e^{i\varphi/2}r_\downarrow u_0 \\ \sin(\vartheta/2)e^{i\varphi/2}r_\downarrow v_0 \end{pmatrix} e^{-ikx} \qquad x < 0, \tag{2.52}$$

and transmitted waves,

$$\Psi_{\text{trans}}(x) = \begin{pmatrix} \cos(\vartheta/2)e^{-i\varphi/2}t_{\uparrow}u_0 \\ \cos(\vartheta/2)e^{-i\varphi/2}t_{\uparrow}v_0 \\ \sin(\vartheta/2)e^{i\varphi/2}t_{\downarrow}u_0 \\ \sin(\vartheta/2)e^{i\varphi/2}t_{\downarrow}v_0 \end{pmatrix} e^{ikx} \quad + \quad \begin{pmatrix} \cos(\vartheta/2)e^{-i\varphi/2}d_{\uparrow}v_0^* \\ \cos(\vartheta/2)e^{-i\varphi/2}d_{\uparrow}u_0^* \\ \sin(\vartheta/2)e^{i\varphi/2}d_{\downarrow}v_0^* \\ \sin(\vartheta/2)e^{i\varphi/2}d_{\downarrow}u_0^* \end{pmatrix} e^{-qx} \qquad x > 0, \tag{2.53}$$

where the superposition coefficient a_σ is an evanescent reflection coefficients, an electron with energy above the gap reflected as an electron below the energy gap, characterized by a shifting from a real to an imaginary wave vector $k \to q$ for both spins, r_σ ordinary reflection coefficients $e \to e$ where the wave vector remain the same, but with opposite direction $k \to -k$, t_σ normal transmission through the interface $k \to k$ and d_σ is the transmitted evanescent wave characterized by a shifting of the wave vector $k \to -q$

2.4.2 Boundary Conditions

Use the appropriate boundary conditions, for the quasiparticles travelling from the semiconductor through the ferromagnet (delta potential).
First requirement, is continuity of the wave function across the boundary located at $x = 0$, cf. Fig. 2.3 which is reasonable if $|\Psi(x)|^2$ is the probability density. Secondly, continuity of the wave function and the potential directly implies continuity of the first derivation of $\Psi(x)$. However the use of a discontinuous potential (Delta function) results in demise of this assumption. Therefore, a determination of the discontinuity in the first derivation given a discontinuous potential is required.

This discontinuity is determined by integrating over the discontinuity, assuming a potential that are discontinuous at the point $x = 0$, integrate then the ansatz solution over the interval from $x_{0-\delta}$ to $x_{0+\delta}$

$$\left(\frac{-\hbar^2}{2m}\frac{\partial^2}{\partial x^2} + \frac{G}{2} + \delta(x)(\lambda_0+\lambda)\right) u_{\uparrow}(x) + d^*_{c,v}\mathcal{E}(\omega)v_{\uparrow}(x) = \varepsilon u_{\uparrow}(x) \tag{2.54}$$

$$\left(\frac{-\hbar^2}{2m}\frac{\partial^2}{\partial x^2} + \frac{G}{2} + \delta(x)(\lambda_0-\lambda)\right) u_{\downarrow}(x) + d^*_{c,v}\mathcal{E}(\omega)(x)v_{\downarrow} = \varepsilon u_{\downarrow}(x) \tag{2.55}$$

$$\left(\frac{\hbar^2}{2m}\frac{\partial^2}{\partial x^2} - \frac{G}{2} + \delta(x)(\lambda_0+\lambda)\right) v_{\uparrow}(x) + d_{c,v}\mathcal{E}^*(\omega)(x)u_{\uparrow} = \varepsilon v_{\uparrow}(x) \tag{2.56}$$

$$\left(\frac{\hbar^2}{2m}\frac{\partial^2}{\partial x^2} - \frac{G}{2} + \delta(x)(\lambda_0-\lambda)\right) v_{\downarrow}(x) + d_{c,v}\mathcal{E}^*(\omega)(x)u_{\downarrow} = \varepsilon v_{\downarrow}(x) \tag{2.57}$$

To illustrate this way of calculation of the discontinuity we take starting point in the eigenvalue problem for the quasiparticle scattering states for the SC-FM-SC junction

$$\begin{aligned} &\int_{x_0-\delta}^{x_0+\delta}\left(\frac{-\hbar^2}{2m}\frac{\partial^2}{\partial x^2} + \frac{G}{2} + \delta(x)(\lambda_0+\lambda)\right) u_{\uparrow}(x) + d^*_{c,v}\mathcal{E}(\omega)v_{\uparrow}(x)dx = \int_{x_0-\delta}^{x_0+\delta}\varepsilon u_{\uparrow}(x)dx \\ &\frac{-\hbar^2}{2m}\int_{x_0-\delta}^{x_0+\delta}\frac{\partial^2}{\partial x^2}u_{\uparrow}(x)dx + \frac{G}{2}\int_{x_0-\delta}^{x_0+\delta}u_{\uparrow}(x)dx + \int_{x_0-\delta}^{x_0+\delta}\delta(x)(\lambda_0+\lambda)u_{\uparrow}(x)dx + d^*_{c,v}\mathcal{E}(\omega)\int_{x_0-\delta}^{x_0+\delta}v_{\uparrow}(x)dx = \int_{x_0-\delta}^{x_0+\delta}\varepsilon u_{\uparrow}(x)dx \end{aligned} \tag{2.58}$$

The idea now is to shrink the interval down until it encloses just x_0, by letting $\delta \to 0$. Assuming that u_σ and v_σ itself is continuous results in that the integral on the right side and the second and fourth integral on the left side go towards zero as $\delta \to 0$

$$\frac{-\hbar^2}{2m}\int_{x_0-\delta}^{x_0+\delta}\frac{\partial^2}{\partial x^2}u_\uparrow(x)dx+\int_{x_0-\delta}^{x_0+\delta}\delta(x)(\lambda_0+\lambda)u_\uparrow(x)dx=0$$
$$\frac{-\hbar^2}{2m}\left.\frac{\partial u_\uparrow(x)}{\partial x}\right|_{x_0-\delta}^{x_0+\delta}=-\delta(x)(\lambda_0+\lambda)u_\uparrow(x_0) \tag{2.59}$$

For the delta function, the equation governing the derivative discontinuity is eq. 2.59

$$\left.\frac{\partial u_\uparrow(x)}{\partial x}\right|_{x_0-\delta}^{x_0+\delta}=\frac{2m}{\hbar^2}(\lambda_0+\lambda)u_\uparrow(x_0)\Rightarrow\left[\left.\frac{\partial u_\uparrow(x+)}{\partial x}\right|_{x=x_0}-\left.\frac{\partial u_\uparrow(x-)}{\partial x}\right|_{x=x_0}\right]=\frac{2m}{\hbar^2}(\lambda_0+\lambda)u_\uparrow(x_0) \tag{2.60}$$
$$\left.\frac{\partial v_\uparrow(x)}{\partial x}\right|_{x_0-\delta}^{x_0+\delta}=-\frac{2m}{\hbar^2}(\lambda_0+\lambda)v_\uparrow(x_0)\Rightarrow\left[\left.\frac{\partial v_\uparrow(x+)}{\partial x}\right|_{x=x_0}-\left.\frac{\partial v_\uparrow(x-)}{\partial x}\right|_{x=x_0}\right]=-\frac{2m}{\hbar^2}(\lambda_0+\lambda)v_\uparrow(x_0) \tag{2.61}$$
$$\left.\frac{\partial u_\downarrow(x)}{\partial x}\right|_{x_0-\delta}^{x_0+\delta}=\frac{2m}{\hbar^2}(\lambda_0-\lambda)u_\downarrow(x_0)\Rightarrow\left[\left.\frac{\partial u_\downarrow(x+)}{\partial x}\right|_{x=x_0}-\left.\frac{\partial u_\downarrow(x-)}{\partial x}\right|_{x=x_0}\right]=\frac{2m}{\hbar^2}(\lambda_0-\lambda)u_\downarrow(x_0) \tag{2.62}$$
$$\left.\frac{\partial v_\downarrow(x)}{\partial x}\right|_{x_0-\delta}^{x_0+\delta}=-\frac{2m}{\hbar^2}(\lambda_0-\lambda)v_\downarrow(x_0)\Rightarrow\left[\left.\frac{\partial v_\downarrow(x+)}{\partial x}\right|_{x=x_0}-\left.\frac{\partial v_\downarrow(x-)}{\partial x}\right|_{x=x_0}\right]=-\frac{2m}{\hbar^2}(\lambda_0-\lambda)v_\downarrow(x_0) \tag{2.63}$$

Summing-up this boundary conditions section for the wave function which should require following, continuous at the origin,

$$\Psi_{in}(x_0)+\Psi_{refl}(x_0)=\Psi_{trans}(x_0) \tag{2.64}$$

as well as satisfy the contact condition for the FM layer exchange force,

$$\frac{\partial u_\sigma(x_0+)}{\partial x}-\frac{\partial u_\sigma(x_0-)}{\partial x}=Z_\sigma u_\sigma(x_0), \tag{2.65}$$
$$\frac{\partial v_\sigma(x_0+)}{\partial x}-\frac{\partial v_\sigma(x_0-)}{\partial x}=-Z_\sigma v_\sigma(x_0), \tag{2.66}$$

where the position

$$Z_\sigma=\frac{2m}{\hbar^2}(\lambda_0+\sigma\lambda_z). \tag{2.67}$$

2.4.3 Calculation: Transmission and Reflection Coefficients

We use the above boundary conditions for the quasiparticle wave functions describing the left 3.9, 3.15 and right side 3.16 of the semiconductor junction. The calculation of the reflection and transmission coefficients is simplified by assuming that the relative mass for particles in the conduction and valences band are equal

1) Continuity

$$\Psi_{in}(x_0)+\Psi_{refl}(x_0)=\Psi_{trans}(x_0)$$

$$u_\uparrow(x_0+)=u_\uparrow(x_0-)$$

$$\cos(\theta/2)e^{-i\varphi/2}u_0e^{ikx_0}+\cos(\theta/2)e^{-i\varphi/2}a_\uparrow v_0^*e^{qx_0}+\cos(\theta/2)e^{-i\varphi/2}r_\uparrow u_0e^{-ikx_0}=\cos(\theta/2)e^{-i\varphi/2}t_\uparrow u_0e^{ikx_0}+\cos(\theta/2)e^{-i\varphi/2}d_\uparrow v_0^*e^{-qx_0}$$

Let $x_0 \to 0$

$$u_0+a_\uparrow v_0^*+r_\uparrow u_0=t_\uparrow u_0+d_\uparrow v_0^* \tag{2.68}$$

$$u_0+a_\downarrow v_0^*+r_\downarrow u_0=t_\downarrow u_0+d_\downarrow v_0^* \tag{2.69}$$

$$v_0+a_\downarrow u_0^*+r_\downarrow v_0=t_\downarrow v_0+d_\downarrow u_0^* \tag{2.70}$$

$$v_0+a_\uparrow u_0^*+r_\uparrow v_0=t_\uparrow v_0+d_\uparrow u_0^* \tag{2.71}$$

2) Amplitude of the Discontinuity

Calculation of the discontinuity amplitude using eq. 2.60 to 2.63.

$$\begin{aligned}\left[\frac{\partial u_\uparrow(x+)}{\partial x}\bigg|_{x=x_0}-\frac{\partial u_\uparrow(x-)}{\partial x}\bigg|_{x=x_0}\right]&=\frac{2m}{\hbar^2}(\lambda_0+\lambda)u_\uparrow(x_0)\\ u_\uparrow(x_0)&=u_0+a_\uparrow v_0^*+r_\uparrow u_0\\ \frac{\partial u_\uparrow(x-)}{\partial x}&=ik\cos(\theta/2)e^{-i\varphi/2}u_0e^{ikx_0}+q\cos(\theta/2)e^{-i\varphi/2}a_\uparrow v_0^*e^{qx_0}-ik\cos(\theta/2)e^{-i\varphi/2}r_\uparrow u_0e^{-ikx_0}\\ \frac{\partial u_\uparrow(x+)}{\partial x}&=ik\cos(\theta/2)e^{-i\varphi/2}t_\uparrow u_0e^{ikx_0}-q\cos(\theta/2)e^{-i\varphi/2}d_\uparrow\bar{u}_0e^{-qx_0}\end{aligned} \tag{2.72}$$

Let $x_0 \to 0$

$$\left[(ikt_\uparrow u_0-qd_\uparrow v_0^*)-(iku_0+qa_\uparrow v_0^*-ikr_\uparrow u_0)\right]=Z_\uparrow(u_0+a_\uparrow v_0^*+r_\uparrow u_0) \tag{2.73}$$

$$\left[(ikt_\downarrow u_0-qd_\downarrow v_0^*)-(iku_0+qa_\downarrow v_0^*-ikr_\downarrow u_0)\right]=Z_\downarrow(u_0+a_\downarrow v_0^*+r_\downarrow u_0) \tag{2.74}$$

$$\left[(ikt_\downarrow v_0-qd_\downarrow u_0^*)-(ikv_0+qa_\downarrow u_0^*-ikr_\downarrow v_0)\right]=-Z_\downarrow(v_0+a_\downarrow u_0^*+r_\downarrow v_0) \tag{2.75}$$

$$\left[(ikt_\uparrow v_0-qd_\uparrow u_0^*)-(ikv_0+qa_\uparrow u_0^*-ikr_\uparrow v_0)\right]=-Z_\uparrow(v_0+a_\uparrow u_0^*+r_\uparrow v_0) \tag{2.76}$$

2.4.4 Transmission and Reflection

By collecting the four linear equation for spin up and down the determination of four spin depended reflection and transmission coefficients can be carried out.

Spin Up: Use equation 2.68, 2.71, 2.73 and 2.76 to calculate the reflection coefficients $a_\uparrow$, $r_\uparrow$ and transmission coefficients $t_\uparrow$, $d_\uparrow$

(2.77)

$$a_\uparrow = \frac{4ikZ_\uparrow u_0 v_0}{Z_\uparrow\left[Z_\uparrow(|u_0|^2-|v_0|^2)-2q\right]+2ik\left[-Z_\uparrow+2q(|u_0|^2-|v_0|^2)\right]} \quad (2.78)$$

$$r_\uparrow = \frac{Z_\uparrow\left[2q-Z_\uparrow(|u|^2-|v|^2)\right]}{Z_\uparrow\left[Z_\uparrow(|u_0|^2-|v_0|^2)-2q\right]+2ik\left[-Z_\uparrow+2q(|u_0|^2-|v_0|^2)\right]} \quad (2.79)$$

$$t_\uparrow = 1+r_\uparrow \quad (2.80)$$

$$d_\uparrow = a_\uparrow \quad (2.81)$$

Spin Down: Equation 2.69, 2.70, 2.74 and 2.75 is used to calculate the reflection coefficients for spin down $a_\downarrow$, $r_\downarrow$ and the transmission coefficients $t_\downarrow$, $d_\downarrow$

$$a_\downarrow = \frac{4ikZ_\downarrow u_0 v_0}{Z_\downarrow\left[Z_\downarrow(|u_0|^2-|v_0|^2)-2q\right]+2ik\left[-Z_\downarrow+2q(|u_0|^2-|v_0|^2)\right]} \quad (2.82)$$

$$r_\downarrow = \frac{Z_\downarrow\left[2q-Z_\downarrow(|u|^2-|v|^2)\right]}{Z_\downarrow\left[Z_\downarrow(|u_0|^2-|v_0|^2)-2q\right]+2ik\left[-Z_\downarrow+2q(|u_0|^2-|v_0|^2)\right]} \quad (2.83)$$

$$t_\downarrow = 1+r_\downarrow \quad (2.84)$$

$$d_\downarrow = a_\downarrow \quad (2.85)$$

Only travelling waves contribute to the probability current, so the transmission and reflection coefficients should obey following condition for the conservation of probability,

$$|r_\sigma|^2+|t_\sigma|^2 = 1 \quad (2.86)$$

In general $|a_\sigma|^2$, $|r_\sigma|^2$, $|t_\sigma|^2$ and $|d_\sigma|^2$ depend on the angle of incidence of the trajectory and on the detailed shape of the scattering potential. For simplicity, we have restricted ourselves to a one-dimensional geometry.

Plot of the square modulus of the reflections and transmission coefficients where it's assumed that the optical field is a coherent monochromatic plan-wave with constant sub-band gap frequency. The laser photon energy to exactly match the bare gap, $G_0 = \omega$, hence $k_F = q_F$. For weak Rabi coupling ($|d_{cv}\mathcal{E}(\omega)|/\varepsilon_F = 0.1$, (—) in fig. 2.4), as the laser intensity increases ($|d_{cv}\mathcal{E}(\omega)|/\varepsilon_F = 0.5$, (—) in fig. 2.4).

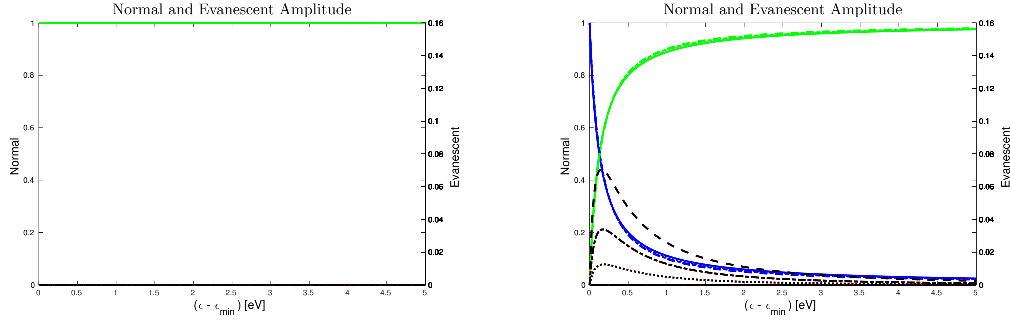

(a) *Normal Reflection* $|b_s|^2$ *and Transmission* $|c_s|^2$ *for* $|d_{cv}\mathcal{E}(\omega)|/\varepsilon_F = [0, 0.1, 0.3, 0.5]$ *eV.*

(b) *Normal Reflection* $|b_s|^2$ *and Transmission* $|c_s|^2$ *for* $|d_{cv}\mathcal{E}(\omega)|/\varepsilon_F = [0, 0.1, 0.3, 0.5]$ *eV.*

Figure 2.4

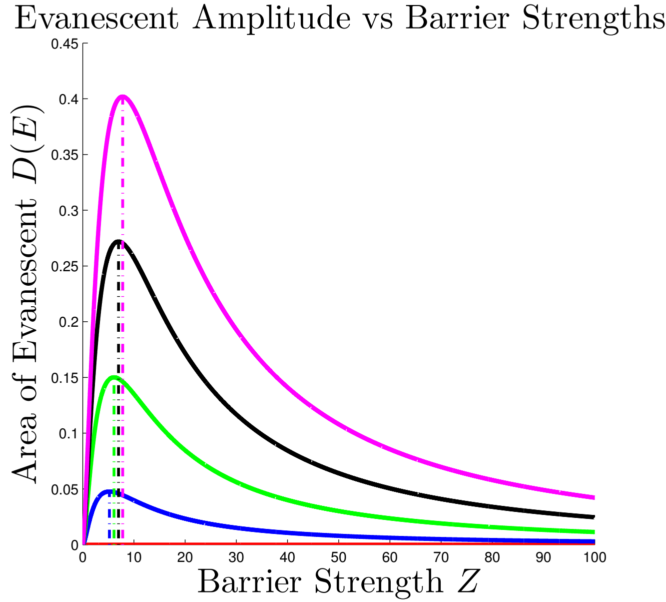

Figure 2.5: *Plots of the evanescent area for are various of different dimensionless interface potential strength* $0 \leq Z_\sigma \leq 100$ *and optical fields* $|d_{cv}\mathcal{E}(\omega)|/\varepsilon_F = [0, 0.1, 0.3, 0.5]$ *eV. From the plots can it been observed that the maximum evanescent amplitude is observed for are barrier strength equal to* $Z_\sigma = 5.22$ *for* $|d_{cv}\mathcal{E}(\omega)|/\varepsilon_F = 0.1$ *eV (—),* $Z_\sigma = 6.11$ *for* $|d_{cv}\mathcal{E}(\omega)|/\varepsilon_F = 0.3$ *eV (—),* $Z_\sigma = 6.99$ *for* $|d_{cv}\mathcal{E}(\omega)|/\varepsilon_F = 0.4$ *eV (—) and* $Z_s = 7.80$ *for* $|d_{cv}\mathcal{E}(\omega)|/\varepsilon_F = 0.5$ *eV (—)*

The plots of the evanescent area for different optical amplitudes, fig. 2.5 shows are increase of the evanescent area for enhancements of the optical field from $|d_{cv}\mathcal{E}(\omega)|/\varepsilon_F = [0, 0.1, 0.3, 0.5]$ eV. Furthermore, is it observed that the evanescent area increase to are maximum for barrier strengths between $5 - 8$ for the different optical fields whereas are decrease of the area for larger barrier strength is observed.

This is in agreement with fig. 2.4 which show are decrease of the transmission amplitude and thereby are increase of the reflection amplitude. These effects is observed for are increase in the optical field. The changes in reflection and transmission amplitudes is due to the increase in the band gap of the semiconductor when the optical field is applied.

Since the FM scattering potential has zero range the scattering phase shift for the odd-parity wave is exactly zero, so we are left with the phase shift δ_σ for the even-parity channel. As shown e.g. in Chap. 8 of Ref.[98], one has $r_\sigma + t_\sigma = exp(2i\delta_\sigma)$, which provides, after some manipulations:

$$\frac{1+itan(\delta)}{1-itan(\delta)} = \frac{Z_\sigma\left[2q - Z_\sigma(|u_0|^2-|v_0|^2)\right]}{Z_\sigma\left[Z_\sigma(|u_0|^2-|v_0|^2)-2q\right]+2ik\left[-Z_\sigma+2q(|u_0|^2-|v_0|^2)\right]} + \frac{4ikq(|u_0|^2-|v_0|^2)-2ikZ_\sigma}{Z_\sigma\left[Z_\sigma(|u_0|^2-|v_0|^2)-2q\right]+2ik\left[-Z_\sigma+2q(|u_0|^2-|v_0|^2)\right]}$$

$$tan(\delta_\sigma) = \frac{-Z_\sigma\left[2q - Z_\sigma(|u_0|^2-|v_0|^2)\right]}{2k\left[-Z_\sigma+2q(|u_0|^2-|v_0|^2)\right]} \tag{2.87}$$

In the limit of weak Rabi coupling, $|u_0|^2 - |v_0|^2 \to 1$, one recovers the expected single-band result,

$$tan(\delta_\sigma) = \frac{-Z_\sigma}{2k} \tag{2.88}$$

For a short-range potential the wave function does not change very much in the region of the potential, and eq. 2.58 gives the change in the derivative of the wave function from one side of the potential to the other. The right-hand side is just the product of the wave function and the integral of the potential which is the phase shift experienced by a free electron when scattered by a contact force of strength Z_σ.

2.5 Conclusion

In this original Chapter background information on the theoretical treatment of the semiconductor-ferromagnet-semiconductor junction has been given.

Different theoretical tools, including the effective-mass theory, the rotating-wave approximation, as well as the quantum theory of scattering, are combined together in order to describe the transfer of angular momentum between polarized electron spin and nanomagnet.

3 Manipulating spin transfer torque with light

The following paper by Karsten Leding Vendelbjerg and Massimo Rontani is in press the journal Superlattices and Microstructures, DOI: 10.1016/j.spmi.2016.12.047

We study the spin transfer torque (STT) induced onto a nanomagnet as a spin-polarized current flows through a junction made of the magnet sandwiched between two semiconductors. This junction is one-dimensional and highly idealized, the thin magnetic layer being mimicked by a spin-dependent contact force. We show that the STT may be externally controlled by shining the junction at sub-bandgap frequency with an intense laser beam. The excitonic coherence driven by the laser dresses the virtual electron-hole pairs coupling conduction and valence bands and inducing evanescent waves at the junction interface. The Fano-like quantum interference between these localized states and the continuum spectrum, being different in the two spin channels, significantly affects the STT.

Spin transfer torque, Optical Stark effect, Fano resonance

3.1 Introduction

A long-term goal of spintronics is the integration between the well-established principles of semiconductor electronics and the novel strategies to manipulate the spin degree of freedom [77]. A key concept is spin transfer torque (STT), which allows for switching the magnetization of an active element by varying the current flowing through the device [99]. Semiconductor structures provide us with light as an additional experimental handle, which may impact both current and magnetization. Recently, the optical reversal of magnetization has received a great deal of attention [100,101,102]. Here we follow a different path, exploring how light may coherently affect the STT in the absence of power absorption.

We consider theoretically a one-dimensional junction made of a thin magnetic layer sandwiched between two identical direct-gap semiconductors. This layer acts as a spin-dependent contact force on electrons, as a *n*-type spin polarized current flows through the junction inducing a STT on the magnetic layer. As we shine the junction with an intense monocromatic laser beam, whose photon energy is smaller than the band gap, we drive a controlled excitonic coherence into the system (optical Stark effect [103,104]). The Rabi energy couples conduction and valence bands, inducing an evanescent wave at the junction interface. We find that the Fano-like interference between this localized wave and the continuum spectrum may significantly vary with the spin projection of the scattering wave, which strongly affects the STT. This kind of coherent

control of the STT has the advantage that the laser does not heat the system, as the optically-excited electron-hole pairs are virtual [52,105].

The toy model we investigate here neglects many relevant features of actual devices, most noticeably band asymmetry, spin-orbit coupling, structure of the semiconductor-magnet interface, which will obviously affect our conclusions. Nevertheless, our aim here is to illustrate a novel concept that is possibly relevant for the coherent control of STT, leaving a more realistic case study to future research.

The structure of the paper is as follows. The Hamiltonian is defined in section 3.2 and the associated scattering problem is solved in section 3.3. After the general theory of the STT is presented in section 3.4, results for a single conduction channel are discussed in section 3.5.

3.2 Semiconductor-nanomagnet-semiconductor junction

We consider the electronic transport through a one-dimensional junction made of a thin single-domain ferromagnetic (FM) layer—a nanomagnet—sandwiched between two identical direct-gap semiconductors (SC), as shown in Fig. 3.1. The FM layer, located at $x = 0$, disconnects the two SC sides, whose bulk Hamiltonians are 2×2 matrix operators

$$H_{\rm SC} = \begin{bmatrix} -(\hbar^2/2m)\partial^2/\partial x^2 + G/2 & d_{cv}^*\,\mathcal{E}(\omega) \\ \\ d_{cv}\,\mathcal{E}^*(\omega) & (\hbar^2/2m)\partial^2/\partial x^2 - G/2 \end{bmatrix}, \tag{3.1}$$

acting on the pseudospinor

$$\Psi_\sigma(x) = \begin{bmatrix} u_\sigma(x) \\ v_\sigma(x) \end{bmatrix}. \tag{3.2}$$

The components u and v are amplitudes for occupying conduction and valence bands, respectively, whereas the additional label $\sigma = \pm 1$ is the projection of spin along the z axis, which we take to be antiparallel to the direction $\mathbf{M}$ of the FM magnetization ($|\mathbf{M}| = 1$), i.e., parallel to the nanomagnet angular momentum. The bands have like masses m, opposite curvatures, and are coupled by a strong monocromatic laser beam of frequency ω and electric field amplitude $\mathcal{E}(\omega)$. The interband dipole matrix element d_{cv} occurring in Eq. (3.1) is evaluated at the band edge in the $\mathbf{k}\cdot\mathbf{p}$ approximation, whereas G is the quasiparticle band gap renormalized by the optical field. The gap G is obtained in the rotating wave approximation starting from the bare direct gap G_0 after performing a gauge transformation [106,103,104],

$$G = G_0 - \hbar\omega, \tag{3.3}$$

where $\hbar\omega$ is the laser photon energy, which may be tuned in the lab. Whereas the SC Hamiltonian $\hat{H}_{\rm SC}$ is diagonal in the electron spin space,

$$\hat{H}_{\rm SC} = H_{\rm SC} \otimes \hat{I}, \tag{3.4}$$

the FM layer is a spin-active scattering interface,

$$\hat{H}_{\mathrm{FM}} = \begin{bmatrix} \lambda_0 \delta(x) & 0 \\ 0 & \lambda_0 \delta(x) \end{bmatrix} \otimes \hat{I} + \begin{bmatrix} \lambda_z \delta(x) & 0 \\ 0 & \lambda_z \delta(x) \end{bmatrix} \otimes \hat{\sigma}_z. \tag{3.5}$$

Here $\hat{I}$ and $\hat{\sigma}_z$ are respectively the identity matrix and the z-component Pauli matrix operating on spin-1/2 spinors, λ_0 is the non-magnetic interface potential strength, and $2\,|\lambda_z|$ is the nanomagnet exchange field. The total junction Hamiltonian is $\hat{H}_{\mathrm{SC}} + \hat{H}_{\mathrm{FM}}$.

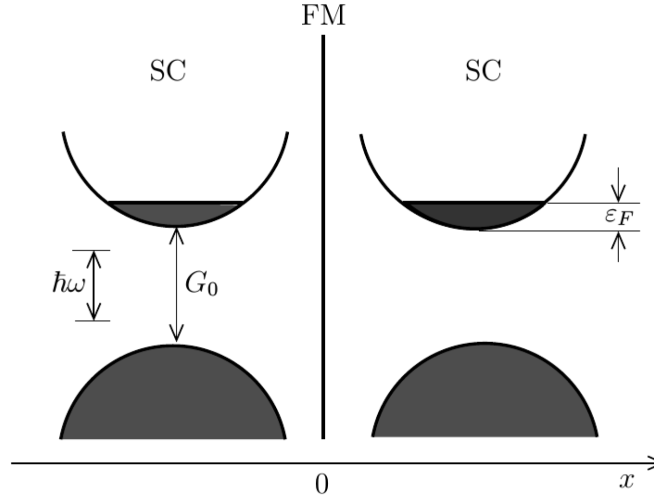

Figure 3.1: Energy landscape of the semiconductor-nanomagnet-semiconductor junction.

We limit our study to the off-resonant case, $G \geq 0$, i.e., only virtual electron-hole pairs are generated by the laser. Besides, we assume the FM layer is transparent to radiation, hence the laser does not heat the system. Furthermore we only consider n-doped systems, that is, in the absence of the optical field at zero temperature the valence band is completely filled whereas electron states in the conduction band are filled up to the (small) Fermi energy ε_F (ε_F is reckoned from the bottom of conduction band, cf. Fig. 3.1). We neglect the renormalization of ε_F due to coherent Rabi coupling. Also, we neglect effects due to electron-electron interactions but the exchange field of the ferromagnetic layer.

3.3 Scattering matrix

The quasiparticle scattering states of the SC-FM-SC junction solve the eigenvalue problem

$$\left(\hat{H}_{\mathrm{SC}} + \hat{H}_{\mathrm{FM}}\right) \Psi(x) = \varepsilon \Psi(x). \tag{3.6}$$

Here the scattering state $\Psi(x)$ is a column vector with four components in the spin / pseudospin product space,

$$\Psi(x) \equiv \begin{bmatrix} \Psi_\uparrow(x) \\ \Psi_\downarrow(x) \end{bmatrix} \equiv \begin{bmatrix} u_\uparrow(x) \\ v_\uparrow(x) \\ u_\downarrow(x) \\ v_\downarrow(x) \end{bmatrix}. \tag{3.7}$$

Since the total junction Hamiltonian commutes with both $\hat{\sigma}_z$ and the spatial inversion $x \to -x$ it follows that the scattering matrix $\hat{\mathcal{S}}$ is diagonal in spin z-projection and parity indices.

To work out $\hat{\mathcal{S}}$ we write $\Psi(x)$ as the sum of an incoming, reflected, and transmitted wave,

$$\Psi(x) = \begin{cases} \Psi_{\text{in}}(x) + \Psi_{\text{refl}}(x) & x < 0, \\ \Psi_{\text{trans}}(x) & x > 0. \end{cases} \tag{3.8}$$

The incoming quasiparticle $\Psi_{\text{in}}(x)$ is a plane wave moving from left to right with spin polarized along the direction $\mathbf{P}_{\text{in}} \equiv (\sin\vartheta\cos\varphi, \sin\vartheta\sin\varphi, \cos\vartheta)$:

$$\Psi_{\text{in}}(x) = \begin{pmatrix} \cos(\vartheta/2)e^{-i\varphi/2}u_0 \\ \cos(\vartheta/2)e^{-i\varphi/2}v_0 \\ \sin(\vartheta/2)e^{i\varphi/2}u_0 \\ \sin(\vartheta/2)e^{i\varphi/2}v_0 \end{pmatrix} e^{ikx} \qquad x < 0. \tag{3.9}$$

This spin polarization may be enforced by either using a second—resonant—laser beam or electrically injecting the electron after it has flown through a spin valve. As (3.9) is a solution of the bulk SC the wave vector $k > 0$ is related to the quasiparticle energy $\varepsilon > 0$ through[107]

$$\varepsilon = \sqrt{\left(\hbar^2k^2/2m + G/2\right)^2 + |d_{cv}\mathcal{E}(\omega)|^2}, \tag{3.10}$$

whereas the excitonic coherence factors u_0 and v_0 are given by

$$|u_0|^2 = \frac{1}{2}\left(1 + \frac{\sqrt{\varepsilon^2 - |d_{cv}\mathcal{E}(\omega)|^2}}{\varepsilon}\right), \tag{3.11}$$

$$|v_0|^2 = 1 - |u_0|^2, \tag{3.12}$$

with their relative phase being fixed by

$$u_0 v_0^* = \frac{d_{cv}^* \mathcal{E}(\omega)}{2\varepsilon}. \tag{3.13}$$

The quasiparticle probability current density is

$$J = \frac{\hbar}{m} \sum_\sigma \mathrm{Im}\left[u_\sigma^*(x) \frac{\partial u_\sigma(x)}{\partial x} - v_\sigma^*(x) \frac{\partial v_\sigma(x)}{\partial x} \right]. \tag{3.14}$$

From the above equations it is clear that the Rabi term $\mathcal{E}d$, proportional to the laser beam intensity, controls the flux of the incoming quasiparticle, $J_{\text{in}} = (\hbar k/m)(|u_0|^2 - |v_0|^2)$. For vanishing interband coupling, J_{in} is simply the flux of an electron in the conduction band ($|u_0|^2 \to 1$ and $|v_0|^2 \to 0$). For strong coupling, J_{in} is suppressed as contributions of conduction and valence bands cancel each other out due to their opposite band curvatures ($|u_0|^2 - |v_0|^2 \to 0$).

A distinctive feature of the two-band model, in contrast with the one-band picture, is that the evanescent wave localized at the interface adds to usual travelling waves to make the elastic-scattering basis complete. In the expression of both reflected,

$$\Psi_{\text{refl}}(x) = \begin{pmatrix} \cos(\vartheta/2) e^{-i\varphi/2} a_\uparrow v_0^* \\ \cos(\vartheta/2) e^{-i\varphi/2} a_\uparrow u_0^* \\ \sin(\vartheta/2) e^{i\varphi/2} a_\downarrow v_0^* \\ \sin(\vartheta/2) e^{i\varphi/2} a_\downarrow u_0^* \end{pmatrix} e^{qx} \quad + \begin{pmatrix} \cos(\vartheta/2) e^{-i\varphi/2} r_\uparrow u_0 \\ \cos(\vartheta/2) e^{-i\varphi/2} r_\uparrow v_0 \\ \sin(\vartheta/2) e^{i\varphi/2} r_\downarrow u_0 \\ \sin(\vartheta/2) e^{i\varphi/2} r_\downarrow v_0 \end{pmatrix} e^{-ikx} \qquad x < 0, \tag{3.15}$$

and transmitted waves,

$$\Psi_{\rm trans}(x) = \begin{pmatrix} \cos(\vartheta/2)e^{-i\varphi/2}t_\uparrow u_0 \\ \cos(\vartheta/2)e^{-i\varphi/2}t_\uparrow v_0 \\ \sin(\vartheta/2)e^{i\varphi/2}t_\downarrow u_0 \\ \sin(\vartheta/2)e^{i\varphi/2}t_\downarrow v_0 \end{pmatrix} e^{ikx} \qquad + \begin{pmatrix} \cos(\vartheta/2)e^{-i\varphi/2}d_\uparrow v_0^* \\ \cos(\vartheta/2)e^{-i\varphi/2}d_\uparrow u_0^* \\ \sin(\vartheta/2)e^{i\varphi/2}d_\downarrow v_0^* \\ \sin(\vartheta/2)e^{i\varphi/2}d_\downarrow u_0^* \end{pmatrix} e^{-qx} \qquad x > 0, \tag{3.16}$$

superposition coefficients are labeled as r_σ, t_σ and a_σ, d_σ for plane and evanescent waves, respectively. Note that the plane-wave weight is mainly in the conduction band whereas the evanescent-wave weight in the valence band. The decay length of the evanescent wave, $1/q > 0$, is related to k and hence to ε through the relation

$$\frac{\hbar^2 q^2}{2m} = \frac{\hbar^2 k^2}{2m} + G. \tag{3.17}$$

To proceed we require that $\Psi(x)$ is continuous at the origin,

$$\Psi_{\rm in}(0) + \Psi_{\rm refl}(0) = \Psi_{\rm trans}(0), \tag{3.18}$$

as well as that it satisfies the contact condition for the FM layer exchange force,

$$\frac{\partial u_\sigma(0+)}{\partial x} - \frac{\partial u_\sigma(0-)}{\partial x} = Z_\sigma u_\sigma(0), \tag{3.19}$$

$$\frac{\partial v_\sigma(0+)}{\partial x} - \frac{\partial v_\sigma(0-)}{\partial x} = -Z_\sigma v_\sigma(0), \tag{3.20}$$

with the position

$$Z_\sigma = \frac{2m}{\hbar^2}(\lambda_0 + \sigma\lambda_z). \tag{3.21}$$

Conditions (3.18), (3.19), and (3.20) provide a linear system of four equations in the four unknowns a_σ, r_σ, t_σ, d_σ for each spin channel. The solution is:

$$a_\sigma = \frac{4ikZ_\sigma u_0 v_0}{\mathcal{D}}, \tag{3.22}$$

$$r_\sigma = Z_\sigma \frac{2q - Z_\sigma(|u_0|^2 - |v_0|^2)}{\mathcal{D}}, \tag{3.23}$$

$$t_\sigma = 1 + r_\sigma, \tag{3.24}$$

$$d_\sigma = a_\sigma, \tag{3.25}$$

with

$$\begin{aligned}\mathcal{D} &= Z_\sigma \left[Z_\sigma(|u_0|^2 - |v_0|^2) - 2q \right] \quad + \\ & 2ik \left[-Z_\sigma + 2q(|u_0|^2 - |v_0|^2) \right].\end{aligned} \tag{3.26}$$

Only travelling waves contribute to the probability current, so the transmission and reflection coefficients are respectively $|J_{\rm trans}| / |J_{\rm in}| = \cos^2(\vartheta/2) \left|t_\uparrow\right|^2 + \sin^2(\vartheta/2) \left|t_\downarrow\right|^2$ and $|J_{\rm refl}| / |J_{\rm in}| = \cos^2(\vartheta/2) \left|r_\uparrow\right|^2 + \sin^2(\vartheta/2) \left|r_\downarrow\right|^2$. It is a straightforward calculation to verify that

$$|r_\sigma|^2 + |t_\sigma|^2 = 1 \tag{3.27}$$

and hence $\hat{\mathcal{S}}$ is unitary as expected.

Since the FM scattering potential has zero range the scattering phase shift for the odd-parity wave is exactly zero, so we are left with the phase shift δ_σ for the even-parity channel. As shown e.g. in Chap. 8 of Ref.[98], one has $r_\sigma + t_\sigma = \exp(2i\delta_\sigma)$, which provides, after some manipulations:

$$\tan \delta_\sigma = -\frac{Z_\sigma \left[2q - Z_\sigma(|u_0|^2 - |v_0|^2) \right]}{2k \left[-Z_\sigma + 2q(|u_0|^2 - |v_0|^2) \right]}. \tag{3.28}$$

In the limit of weak Rabi coupling, $|u_0|^2 - |v_0|^2 \to 1$, one recovers the expected single-band result,

$$\tan \delta_\sigma \to -\frac{Z_\sigma}{2k}, \tag{3.29}$$

which is the phase shift experienced by a free electron when scattered by a contact force of strength Z_σ.

3.4 Spin transfer torque

To compute the spin transfer torque (STT) exerted by the FM layer on the carriers flowing through the SC-FM-SC junction, we generalize the spin density matrix formalism of Ref.[108] to two bands. For n-type quasiparticles, the total probability current j and spin current $\mathbf{j}^S$ at time t are respectively

$$j(t) = \frac{1}{2\pi} \int dk \, \frac{\hbar k}{m} \left[|u_0(k)|^2 - |v_0(k)|^2 \right] \mathrm{Tr}[\hat{\rho}(k,t)], \tag{3.30}$$

and

$$\mathbf{j}^S(t) = \frac{1}{2\pi} \int dk \, \frac{\hbar^2 k}{2m} \left[|u_0(k)|^2 - |v_0(k)|^2 \right] \mathrm{Tr}[\hat{\boldsymbol{\sigma}} \hat{\rho}(k,t)], \tag{3.31}$$

where $\hat{\rho}(k,t)$ is the 2×2 nonequilibrium density matrix in spin space and $\hat{\boldsymbol{\sigma}}$ is the vector whose components are Pauli matrices.

In the following we specialize in the case of a transient spin-polarized current impinging on the FM layer from the left SC. This current may be generated either through pulsed electrical injection of carriers[109] previously filtered by a spin valve or by shining the SC with a short optical pulse[108]. In the latter case the laser that pumps real electron-hole pairs (photon energy $> G_0$) imprinting carrier spins through optical selection rules must not be confused with the laser $\mathcal{E}(\omega)$ that continuously creates virtual electron-hole pairs ($\hbar\omega < G_0$). We may neglect the valence hole contribution to the STT since the hole spin relaxation time is much shorter than the optical recombination time in III-V group semiconductors[110].

In all events, we write the density matrix $\hat{\rho}_{\rm in}$ right after the generation of the transient current as

$$\hat{\rho}_{\rm in}(k,t=0) = f_{\rm in}(k)\frac{1}{2}\left(\hat{I}+\mathbf{P}_{\rm in}\cdot\hat{\boldsymbol{\sigma}}\right). \tag{3.32}$$

The spin is polarized along $\mathbf{P}_{\rm in}$ as in (3.9) and $f_{\rm in}(k)$ is the initial nonequilibrium distribution of the hot quasiparticles injected into the left SC. Since orbital relaxation is much faster than spin relaxation in n-doped samples[111], at the following times $f_{\rm in}(k,t)$ decays with a spin-independent relaxation time τ_k,

$$f_{\rm in}(k,t) = f_{\rm in}(k)\exp(-t/\tau_k). \tag{3.33}$$

The integrated distribution provides the number $n_{\rm in}$ of injected electrons per unit length,

$$n_{\rm in} = \frac{1}{2\pi}\int dk\, f_{\rm in}(k) \tag{3.34}$$

(we assume $n_{\rm in}$ much smaller than the doping density).

Following Ref.[108], we make the spin structure of the 2×2 reflection matrix explicit,

$$\hat{r}(k) = \frac{1}{2}\left\{[r_\downarrow(k)+r_\uparrow(k)]\,\hat{I}+[r_\downarrow(k)-r_\uparrow(k)]\,\mathbf{M}\cdot\hat{\boldsymbol{\sigma}}\right\}, \tag{3.35}$$

as well as that of the transmission matrix $\hat{t}(k)$, with matrix elements being given by (3.23) and (3.24), respectively. Neglecting multiple reflections due to sample boundaries, the total particle current j_L flowing from left to right in the left SC is

$$\begin{aligned} j_L(t) \quad = \quad & \frac{1}{2\pi}\int_{k>0} dk\frac{\hbar k}{m}\left[|u_0(k)|^2-|v_0(k)|^2\right] \quad \times \\ & \mathrm{Tr}[\hat{\rho}_{\rm in}(k,t)-\hat{\rho}_{\rm refl}(k,t)], \end{aligned} \tag{3.36}$$

where the reflected density matrix is given by

$$\begin{aligned} \hat{\rho}_{\rm refl}(k,t) \quad = \quad & \hat{r}(k)\,\hat{\rho}_{\rm in}(k,t)\,\hat{r}^\dagger(k) \quad = \\ & f_{\rm in}(k,t)\frac{1}{2}\left[R_0(k)\hat{I}+\mathbf{R}(k)\cdot\hat{\boldsymbol{\sigma}}\right], \end{aligned} \tag{3.37}$$

where, with the k dependence understood,

$$R_0 = \frac{1}{2}\left[\left(|r_\downarrow|^2+|r_\uparrow|^2\right)+\left(|r_\downarrow|^2-|r_\uparrow|^2\right)\mathbf{M}\cdot\mathbf{P}_{\rm in}\right], \tag{3.38}$$

$$
\begin{aligned}
\mathbf{R} &= \frac{1}{2}\left[\left(|r_\downarrow|^2 - |r_\uparrow|^2\right) + \left(|r_\downarrow|^2 + |r_\uparrow|^2\right)\mathbf{M}\cdot\mathbf{P}_{\text{in}}\right]\mathbf{M} \\
&+ \operatorname{Re}\left(r_\downarrow r_\uparrow^*\right)(\mathbf{M}\times\mathbf{P}_{\text{in}})\times\mathbf{M} - \operatorname{Im}\left(r_\downarrow r_\uparrow^*\right)\mathbf{M}\times\mathbf{P}_{\text{in}}.
\end{aligned}
\tag{3.39}
$$

Therefore, the spin $\mathbf{S}_L$ accumulated on the left hand side of the SC-FM-SC junction is

$$
\begin{aligned}
\mathbf{S}_L &= -\int_0^\infty dt\, \mathbf{j}_L^S(t) = -\int_0^\infty dt \int_{k>0} dk\, \frac{\hbar^2 k}{4\pi m} \quad \times \\
&\left[|u_0(k)|^2 - |v_0(k)|^2\right] \operatorname{Tr}\{\hat{\boldsymbol{\sigma}}\,[\hat{\rho}_{\text{in}}(k,t) - \hat{\rho}_{\text{refl}}(k,t)]\} \\
&= \frac{1}{2\pi}\int_{k>0} dk\, \frac{\hbar^2 k \tau_k}{2m} f_{\text{in}}(k)\left[|u_0(k)|^2 - |v_0(k)|^2\right] \\
&\times [\mathbf{R}(k) - \mathbf{P}_{\text{in}}].
\end{aligned}
\tag{3.40}
$$

A similar expression for the spin accumulated on the right hand side of the junction, $\mathbf{S}_R$, is obtained by replacing $\mathbf{R}(k) - \mathbf{P}_{\text{in}}$ with $\mathbf{T}(k)$ in (3.40).

The spin transfer torque $\mathbf{N}_{\text{STT}}$ (averaged over the relaxation time τ, which we assume to weakly depend on k) is the projection of $(\mathbf{S}_L + \mathbf{S}_R)/\tau$ onto the vectors $\mathbf{M}\times\mathbf{P}_{\text{in}}$ and $(\mathbf{M}\times\mathbf{P}_{\text{in}})\times\mathbf{M}$, that is

$$
\begin{aligned}
\mathbf{N}_{\text{STT}} &= \frac{1}{2\pi}\int_{k>0} dk \frac{\hbar^2 k}{2m} f_{\text{in}}(k)\left[|u_0(k)|^2 - |v_0(k)|^2\right] \quad \times \\
&\Big\{ \left[\operatorname{Re}\left(r_\downarrow r_\uparrow^* + t_\downarrow t_\uparrow^*\right) - 1\right](\mathbf{M}\times\mathbf{P}_{\text{in}})\times\mathbf{M} \\
&\quad - \operatorname{Im}\left(r_\downarrow r_\uparrow^* + t_\downarrow t_\uparrow^*\right)\mathbf{M}\times\mathbf{P}_{\text{in}} \Big\},
\end{aligned}
\tag{3.41}
$$

or, in terms of phase shifts,

$$
\begin{aligned}
\mathbf{N}_{\text{STT}} &= \frac{1}{2\pi}\int_{k>0} dk \frac{\hbar^2 k}{4m} f_{\text{in}}(k)\left[|u_0(k)|^2 - |v_0(k)|^2\right] \quad \times \\
&\Big[(\cos\{2[\delta_\uparrow(k) - \delta_\downarrow(k)]\} - 1)(\mathbf{M}\times\mathbf{P}_{\text{in}})\times\mathbf{M} \\
&\quad + \sin\{2[\delta_\uparrow(k) - \delta_\downarrow(k)]\}(\mathbf{M}\times\mathbf{P}_{\text{in}}) \Big],
\end{aligned}
\tag{3.42}
$$

where the phase shifts $\delta_\sigma(k)$ are given by (3.28). From (3.42) it is apparent that there is no STT if the interface potential is non magnetic ($\delta_\uparrow = \delta_\downarrow$).

3.5 Single channel

To uncover the key features of the junction, in the following we assume that only a single channel with Fermi wave vector k_F contributes to spin transfer in (3.42). The STT takes the form

$$\mathbf{N}_{\mathrm{STT}} = \frac{\hbar}{4} n_F v_F \left(|u_0|^2 - |v_0|^2\right) \Big[\sin[2(\delta_\uparrow - \delta_\downarrow)] \mathbf{M} \times \mathbf{P}_{\mathrm{in}} + \left\{ \cos[2(\delta_\uparrow - \delta_\downarrow)] - 1 \right\} (\mathbf{M} \times \mathbf{P}_{\mathrm{in}}) \times \mathbf{M} \Big], \tag{3.43}$$

where n_F is the number of injected electrons per unit length at the Fermi energy and $v_F = \hbar k_F / m$.

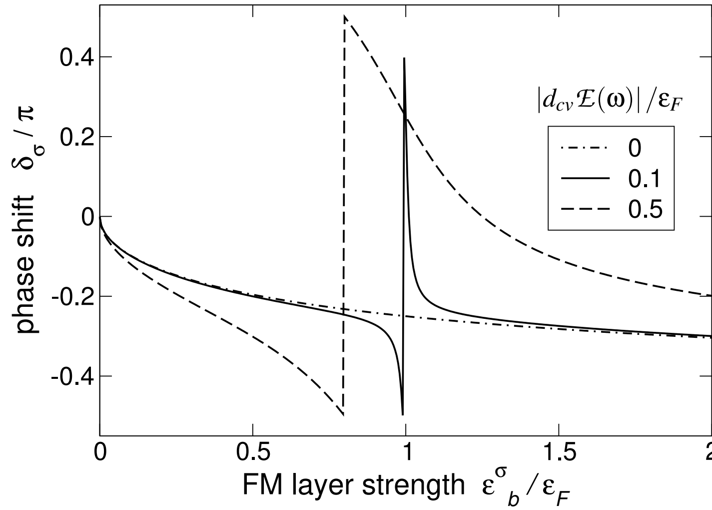

Figure 3.2: Scattering phase shift normalized to π, δ_σ/π, vs dimensionless interface potential strength, $\varepsilon^\sigma_b/\varepsilon_F$, for selected values of the Rabi energy, $|d_{cv}\mathcal{E}(\omega)|/\varepsilon_F$. Here ε^σ_b is the binding energy of the valence-band state, ε_F is the Fermi energy, and the laser is at resonance, $\hbar\omega = G_0$.

From (3.43) it is clear that the STT is ruled by the phase shift difference bewtween the two spin channels. Therefore, we first discuss the behavior of δ_σ. It is important to note that, for negliglible Rabi energy, the evanescent wave localized at the interface is a legitimate bound-state solution of (3.6) with (binding) energy

$$\varepsilon^\sigma_b = \frac{m}{2\hbar^2} (\lambda_0 + \sigma\lambda_z)^2 . \tag{3.44}$$

Here and throughout the paper we have assumed $\lambda_0 + \sigma\lambda_z > 0$, hence the interface state forms in the valence band with $\varepsilon^\sigma_b > 0$. For $\lambda_0 + \sigma\lambda_z < 0$ the bound state forms in the conduction band with $\varepsilon^\sigma_b < 0$. Moreover, we define the dimensionless interface potential strength, Z_σ/k_F, which is related to ε^σ_b by

$$\frac{Z_\sigma}{k_F} = \frac{2m}{\hbar^2 k_F} (\lambda_0 + \sigma\lambda_z) = 2\sqrt{\frac{\varepsilon^\sigma_b}{\varepsilon_F}} . \tag{3.45}$$

As a reference, let us first consider the simple single-band case, which is recovered when the continuous laser beam is switched off. Figure 3.2 shows the dependence of δ_σ/π on the di-

mensionless ratio $\varepsilon_b^\sigma/\varepsilon_F$ parametrizing the interface potential strength (dashed-dotted line). The phase is negative, smoothly decreasing from zero value—in the absence of scattering—to the limit value $\delta_\sigma = -\pi/2$ for infinite strength. The STT depends on the fixed interface parameters $\varepsilon_b^\uparrow$ and $\varepsilon_b^\downarrow$ in a straightforward way through (3.43). The only experimental handle to tune $\mathbf{N}_{\mathrm{STT}}$, apart from replacing the device, is by changing the doping level and hence ε_F.

For finite Rabi energy, which is proportional to the laser beam intensity, the phase exhibits a non trivial behavior. Here we take the laser photon energy to exactly match the bare gap, $G_0 = \hbar\omega$, hence $k_F = q_F$. For weak Rabi coupling ($|d_{cv}\mathcal{E}(\omega)|/\varepsilon_F = 0.1$, solid line in Fig. 3.2) the phase shift first behaves as in the absence of the laser close to the origin, but then it suddenly jumps of $\approx \pi$ changing sign when $\varepsilon_b^\sigma/\varepsilon_F$ approaches unity, and then it overlaps again with the one-band result. As the laser intensity increases ($|d_{cv}\mathcal{E}(\omega)|/\varepsilon_F = 0.5$, dashed line) the overlap with the dashed-dotted curve decreases whereas the threshold at which the phase jumps moves to lower values of $\varepsilon_b^\sigma/\varepsilon_F$.

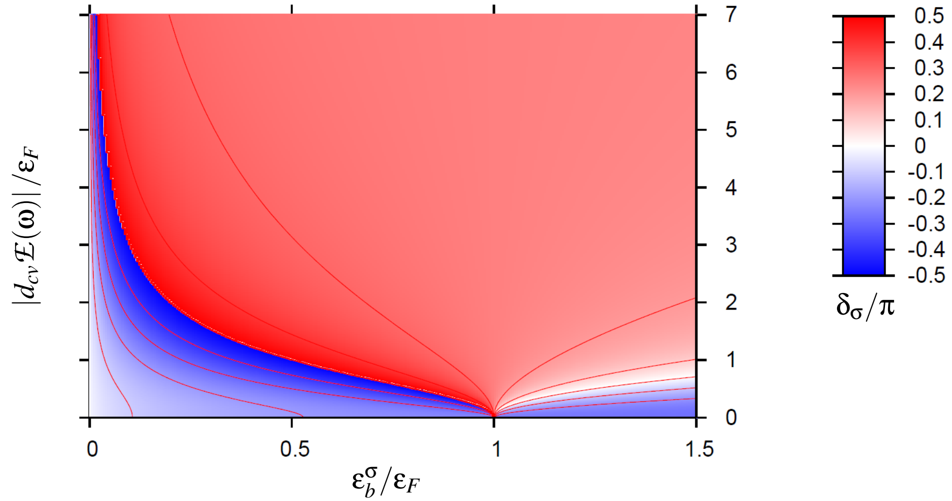

Figure 3.3: (color online) Contour map of the scattering phase shift normalized to π, δ_σ/π. The axes are respectively the binding energy of the valence-band state localized at the interface, ε_b^σ, and the Rabi energy of the laser, $|d_{cv}\mathcal{E}(\omega)|$. Both quantities are normalized to the Fermi energy, ε_F. The color code goes from -0.5 (blue) through zero (white) up to 0.5 (red). Here the laser is at resonance, $\hbar\omega = G_0$.

The contour map of δ_σ in the two-dimensional space whose axes are respectively $\varepsilon_b^\sigma/\varepsilon_F$ and $|d_{cv}\mathcal{E}(\omega)|/\varepsilon_F$ (Fig. 3.3) allows to locate the critical line at which the phase abruptly jumps. This curve is the discontinuous frontier between regions of positive (red color) and negative (blue) values of δ_σ, with $|\delta_\sigma| \approx \pi/2$. Since the phase jump occurs as the denominator on the right hand side of (3.28) changes sign, the equation of the critical line is:

$$\frac{|d_{cv}\mathcal{E}(\omega)|}{\varepsilon_F} = \left(\frac{\varepsilon_F}{\varepsilon_b^\sigma} - 1\right)^{1/2} \qquad \varepsilon_b^\sigma/\varepsilon_F \leq 1. \tag{3.46}$$

For large Rabi energy this frontier tends asymptotically to the axis $\varepsilon_b^\sigma/\varepsilon_F = 0$ whereas for vanishing Rabi energy the line ends exactly at $\varepsilon_b^\sigma/\varepsilon_F = 1$. Interestingly, a second nodal line (white color) develops for $\varepsilon_b^\sigma/\varepsilon_F > 1$ as the specular reflection of (3.46) with respect to the axis $\varepsilon_b^\sigma/\varepsilon_F = 1$, but now the transition between positive and negative regions is smoothed.

We attribute the abrupt variations of the phase to the Fano-like quantum interference[112] between the localized state of energy ε_b^σ in the valence band and the scattering state of energy ε_F in the conduction band. This is apparent for a tiny Rabi energy, as the phase jump occurs exactly when $\varepsilon_F = \varepsilon_b^\sigma$. The increase of the Rabi energy shifts this resonance while decreasing the resonance lifetime and hence broadening the width of the interval in which δ_σ varies significantly.

The appearance of a resonance with the increase of the Rabi energy and the following abrupt jump of the scattering phase suggests that the laser beam intensity might be a powerful experimental handle to enhance / suppress the STT.

This is illustrated in Fig. 3.4 by the plot of the projections of $\mathbf{N}_{\mathrm{STT}}/(n_F v_F \hbar/4)$ on the directions $(\mathbf{M} \times \mathbf{P}_{\mathrm{in}}) \times \mathbf{M}$ (solid line) and $\mathbf{M} \times \mathbf{P}_{\mathrm{in}}$ (dashed line), respectively. When the laser is switched off the value of the STT is given at the origin of the $|d_{cv}\mathcal{E}(\omega)|/\varepsilon_F$ axis and is fixed by the device parameters. Here we consider three exemplar cases, that is, the interface parameters for the two spin channels are: (a) both below the zero-field critical value unity, $\varepsilon_b^\uparrow/\varepsilon_F = 0.5$, $\varepsilon_b^\downarrow/\varepsilon_F = 0.8$ (b) one below and one above, $\varepsilon_b^\uparrow/\varepsilon_F = 0.5$, $\varepsilon_b^\downarrow/\varepsilon_F = 1.2$ (c) both above, $\varepsilon_b^\uparrow/\varepsilon_F = 1.2$, $\varepsilon_b^\downarrow/\varepsilon_F = 1.5$.

Switching on the laser allows to widely modulate the STT, increasing its absolute value even by orders of magnitude [e.g. in panel (a) compare the minimum of the solid curve with respect to the value at the origin] and approaching the extremal values theoretically allowed for the STT, i.e. ± 1 for the dashed curve and -2 for the solid curve. Generically, as $|d_{cv}\mathcal{E}(\omega)|/\varepsilon_F$ increases, the absolute value of the STT reaches a maximum, approximately located in the range of $|d_{cv}\mathcal{E}(\omega)|/\varepsilon_F$ between the origin and unity. Panel (b) displays the most complex beahavior, as around $|d_{cv}\mathcal{E}(\omega)|/\varepsilon_F \approx 0.18$ the STT is perfectly suppressed. In addition, the component along $\mathbf{M} \times \mathbf{P}_{\mathrm{in}}$ changes sign twice. For strong Rabi coupling, all three panels share the same trend, as the STT is asymptotically suppressed. This may be understood from (3.28) since $(|u_0|^2 - |v_0|^2) \to 0$ and hence $\delta_\sigma \to \pi/4$ in both spin channels. Therefore, the strong excitonic coherence imprinted by the laser counteracts the spin transfer torque.

3.6 Conclusions

In conclusion, we have explored at a seminal level a way to coherently control the spin transfer torque by means of the sub-bandgap optical Stark effect. The method is promising as it provides an experimentale handle to change the efficiency of the STT without heating the system. Further work is needed to validate this idea in a more realistic setup.

We thank Lu Sham for many stimulating interactions as well as for hosting both of us at University of California San Diego. This work was supported by EU Marie Curie Initial Training Network INDEX.

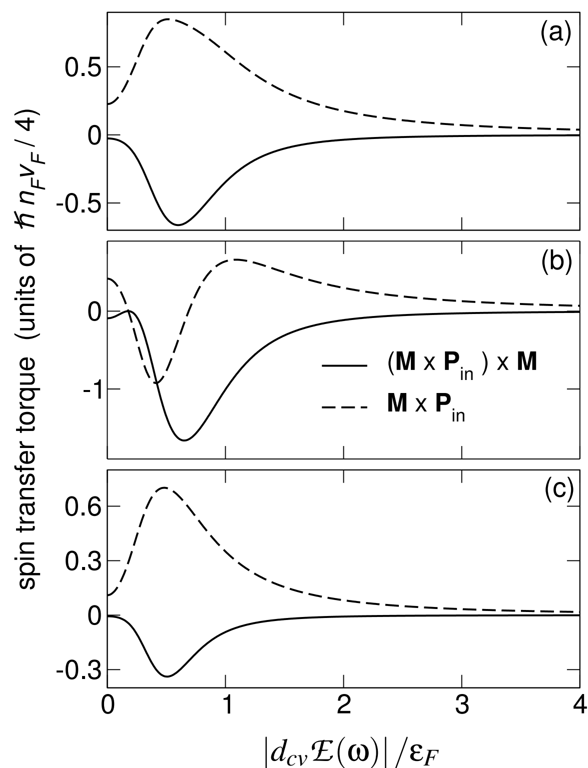

Figure 3.4: Spin transfer torque $\mathbf{N}_{\mathrm{STT}}/(n_F v_F \hbar/4)$ projected along $(\mathbf{M}\times\mathbf{P}_{\mathrm{in}})\times\mathbf{M}$ (solid line) and $\mathbf{M}\times\mathbf{P}_{\mathrm{in}}$ (dashed line), respectively, vs dimensionless Rabi energy $|d_{cv}\mathcal{E}(\omega)|/\varepsilon_F$. (a) $\varepsilon_b^{\uparrow}/\varepsilon_F = 0.5$, $\varepsilon_b^{\downarrow}/\varepsilon_F = 0.8$. (b) $\varepsilon_b^{\uparrow}/\varepsilon_F = 0.5$, $\varepsilon_b^{\downarrow}/\varepsilon_F = 1.2$. (c) $\varepsilon_b^{\uparrow}/\varepsilon_F = 1.2$, $\varepsilon_b^{\downarrow}/\varepsilon_F = 1.5$. Here the laser is at resonance, $\hbar\omega = G_0$.

4 Conclusion

In this Thesis we have explored, at a seminal level, a way to coherently control the spin transfer torque by means of the sub-bandgap optical Stark effect. The proposed junction, made of a ferromagnetic semiconductor thin active layer sandwiched between two standard direct-gap semiconductors, is promising as it provides an experimentale handle to change the efficiency of the spin transfer torque without heating the system.

Further work is needed to validate this idea in a more realistic setup. Whereas the actual suitability of dilute magnetic semiconductors for applications is currently debated, we remark that heterostructures similar in design to the one we have proposed in this Thesis have already been realized and successfully investigated.

Future directions of the research reported in this Thesis are somehow obvious. The first goal is certainly to relax the several approximations involved in the simple toy model we have analyzed in order to describe a realistic junction. Our goal here was to focus on a novel concept to control spin transfer torque.

References

[1] S. Wolf, D. Awschalom, R. Buhrman, J. Daughton, S. Von Molnar, M. Roukes, A. Y. Chtchelkanova, and D. Treger, "Spintronics: a spin-based electronics vision for the future," *Science*, vol. 294, no. 5546, pp. 1488–1495, 2001.

[2] M. N. Baibich, J. M. Broto, A. Fert, F. N. Van Dau, F. Petroff, P. Etienne, G. Creuzet, A. Friederich, and J. Chazelas, "Giant magnetoresistance of (001) fe/(001) cr magnetic superlattices," *Physical review letters*, vol. 61, no. 21, p. 2472, 1988.

[3] G. Binasch, P. Grünberg, F. Saurenbach, and W. Zinn, "Enhanced magnetoresistance in layered magnetic structures with antiferromagnetic interlayer exchange," *Physical review B*, vol. 39, no. 7, p. 4828, 1989.

[4] M. Julliere, "Tunneling between ferromagnetic films," *Physics letters A*, vol. 54, no. 3, pp. 225–226, 1975.

[5] S. Ikeda, J. Hayakawa, Y. Ashizawa, Y. Lee, K. Miura, H. Hasegawa, M. Tsunoda, F. Matsukura, and H. Ohno, "Tunnel magnetoresistance of 604% at 300 k by suppression of ta diffusion in cofeb/mgo/cofeb pseudo-spin-valves annealed at high temperature," *Applied Physics Letters*, vol. 93, no. 8, p. 2508, 2008.

[6] W. Butler, X.-G. Zhang, T. Schulthess, and J. MacLaren, "Spin-dependent tunneling conductance of fel mgol fe sandwiches," *Physical Review B*, vol. 63, no. 5, p. 054416, 2001.

[7] J. Mathon and A. Umerski, "Theory of tunneling magnetoresistance of an epitaxial fe/mgo/fe (001) junction," *Physical Review B*, vol. 63, no. 22, p. 220403, 2001.

[8] S. S. Parkin, C. Kaiser, A. Panchula, P. M. Rice, B. Hughes, M. Samant, and S.-H. Yang, "Giant tunnelling magnetoresistance at room temperature with mgo (100) tunnel barriers," *Nature materials*, vol. 3, no. 12, pp. 862–867, 2004.

[9] S. Yuasa, T. Nagahama, A. Fukushima, Y. Suzuki, and K. Ando, "Giant room-temperature magnetoresistance in single-crystal fe/mgo/fe magnetic tunnel junctions," *Nature materials*, vol. 3, no. 12, pp. 868–871, 2004.

[10] J. C. Slonczewski, "Current-driven excitation of magnetic multilayers," *Journal of Magnetism and Magnetic Materials*, vol. 159, no. 1, pp. L1–L7, 1996.

[11] L. Berger, "Emission of spin waves by a magnetic multilayer traversed by a current," *Physical Review B*, vol. 54, no. 13, p. 9353, 1996.

[12] E. Myers, D. Ralph, J. Katine, R. Louie, and R. Buhrman, "Current-induced switching of domains in magnetic multilayer devices," *Science*, vol. 285, no. 5429, pp. 867–870, 1999.

[13] J. Katine, F. Albert, R. Buhrman, E. Myers, and D. Ralph, "Current-driven magnetization reversal and spin-wave excitations in co/cu/co pillars," *Physical Review Letters*, vol. 84, no. 14, p. 3149, 2000.

[14] S. I. Kiselev, J. Sankey, I. Krivorotov, N. Emley, R. Schoelkopf, R. Buhrman, and D. Ralph, "Microwave oscillations of a nanomagnet driven by a spin-polarized current," *Nature*, vol. 425, no. 6956, pp. 380–383, 2003.

[15] D. C. Ralph and M. D. Stiles, "Spin transfer torques," *Journal of Magnetism and Magnetic Materials*, vol. 320, no. 7, pp. 1190–1216, 2008.

[16] J. Slonczewski, "Currents and torques in metallic magnetic multilayers," *Journal of Magnetism and Magnetic Materials*, vol. 247, no. 3, pp. 324–338, 2002.

[17] I. Theodonis, N. Kioussis, A. Kalitsov, M. Chshiev, and W. Butler, "Anomalous bias dependence of spin torque in magnetic tunnel junctions," *Physical review letters*, vol. 97, no. 23, p. 237205, 2006.

[18] C. Wang, Y.-T. Cui, J. A. Katine, R. A. Buhrman, and D. C. Ralph, "Time-resolved measurement of spin-transfer-driven ferromagnetic resonance and spin torque in magnetic tunnel junctions," *Nature Physics*, vol. 7, no. 6, pp. 496–501, 2011.

[19] R. Koch, J. Katine, and J. Sun, "Time-resolved reversal of spin-transfer switching in a nanomagnet," *Physical review letters*, vol. 92, no. 8, p. 088302, 2004.

[20] W. F. Brown Jr, "Thermal fluctuations of a single-domain particle," *Journal of Applied Physics*, vol. 34, no. 4, pp. 1319–1320, 1963.

[21] I. Krivorotov, N. Emley, A. Garcia, J. Sankey, S. Kiselev, D. Ralph, and R. Buhrman, "Temperature dependence of spin-transfer-induced switching of nanomagnets," *Physical review letters*, vol. 93, no. 16, p. 166603, 2004.

[22] Z. Li and S. Zhang, "Thermally assisted magnetization reversal in the presence of a spin-transfer torque," *Physical Review B*, vol. 69, no. 13, p. 134416, 2004.

[23] D. Apalkov and P. Visscher, "Spin-torque switching: Fokker-planck rate calculation," *Physical Review B*, vol. 72, no. 18, p. 180405, 2005.

[24] P. Braganca, I. Krivorotov, O. Ozatay, A. Garcia, N. Emley, J. Sankey, D. Ralph, and R. Buhrman, "Reducing the critical current for short-pulse spin-transfer switching of nanomagnets," *Applied Physics Letters*, vol. 87, no. 11, p. 112507, 2005.

[25] L. Liu, T. Moriyama, D. Ralph, and R. Buhrman, "Reduction of the spin-torque critical current by partially canceling the free layer demagnetization field," *Applied Physics Letters*, vol. 94, no. 12, p. 122508, 2009.

[26] A. Kent, B. Özyilmaz, and E. Del Barco, "Spin-transfer-induced precessional magnetization reversal," *Applied Physics Letters*, vol. 84, no. 19, pp. 3897–3899, 2004.

[27] O. Lee, V. Pribiag, P. Braganca, P. Gowtham, D. Ralph, and R. Buhrman, "Ultrafast switching of a nanomagnet by a combined out-of-plane and in-plane polarized spin current pulse," *Applied Physics Letters*, vol. 95, no. 1, p. 012506, 2009.

[28] S. Mangin, D. Ravelosona, J. Katine, M. Carey, B. Terris, and E. E. Fullerton, "Current-induced magnetization reversal in nanopillars with perpendicular anisotropy," *Nature Materials*, vol. 5, no. 3,

pp. 210–215, 2006.

[29] T. Devolder, A. Tulapurkar, Y. Suzuki, C. Chappert, P. Crozat, and K. Yagami, “Temperature study of the spin-transfer switching speed from dc to 100ps,” *Journal of applied physics*, vol. 98, no. 5, p. 053904, 2005.

[30] I. Krivorotov, N. Emley, J. Sankey, S. Kiselev, D. Ralph, and R. Buhrman, “Time-domain measurements of nanomagnet dynamics driven by spin-transfer torques,” *Science*, vol. 307, no. 5707, pp. 228–231, 2005.

[31] Y.-T. Cui, G. Finocchio, C. Wang, J. Katine, R. Buhrman, and D. Ralph, “Single-shot time-domain studies of spin-torque-driven switching in magnetic tunnel junctions,” *Physical review letters*, vol. 104, no. 9, p. 097201, 2010.

[32] N. Emley, I. Krivorotov, O. Ozatay, A. Garcia, J. Sankey, D. Ralph, and R. Buhrman, “Time-resolved spin-torque switching and enhanced damping in permalloy/cu/permalloy spin-valve nanopillars,” *Physical review letters*, vol. 96, no. 24, p. 247204, 2006.

[33] T. Devolder, J. Hayakawa, K. Ito, H. Takahashi, S. Ikeda, P. Crozat, N. Zerounian, J.-V. Kim, C. Chappert, and H. Ohno, “Single-shot time-resolved measurements of nanosecond-scale spin-transfer induced switching: Stochastic versus deterministic aspects,” *Physical review letters*, vol. 100, no. 5, p. 057206, 2008.

[34] I. Krivorotov, N. Emley, R. Buhrman, and D. Ralph, “Time-domain studies of very-large-angle magnetization dynamics excited by spin transfer torques,” *Physical Review B*, vol. 77, no. 5, p. 054440, 2008.

[35] J. Sankey, I. Krivorotov, S. Kiselev, P. Braganca, N. Emley, R. Buhrman, and D. Ralph, “Mechanisms limiting the coherence time of spontaneous magnetic oscillations driven by dc spin-polarized currents,” *Physical Review B*, vol. 72, no. 22, p. 224427, 2005.

[36] S. Kiselev, J. Sankey, I. Krivorotov, N. Emley, A. Garcia, R. Buhrman, and D. Ralph, “Spin-transfer excitations of permalloy nanopillars for large applied currents,” *Physical Review B*, vol. 72, no. 6, p. 064430, 2005.

[37] K. Thadani, G. Finocchio, Z.-P. Li, O. Ozatay, J. Sankey, I. Krivorotov, Y.-T. Cui, R. Buhrman, and D. Ralph, “Strong linewidth variation for spin-torque nano-oscillators as a function of in-plane magnetic field angle,” *Physical Review B*, vol. 78, no. 2, p. 024409, 2008.

[38] W. Rippard, M. Pufall, S. Kaka, S. Russek, and T. Silva, “Direct-current induced dynamics in c o 90 f e 10/n i 80 f e 20 point contacts,” *Physical Review Letters*, vol. 92, no. 2, p. 027201, 2004.

[39] W. Rippard, M. Pufall, S. Kaka, T. Silva, and S. Russek, “Current-driven microwave dynamics in magnetic point contacts as a function of applied field angle,” *Physical Review B*, vol. 70, no. 10, p. 100406, 2004.

[40] V. Pribiag, I. Krivorotov, G. Fuchs, P. Braganca, O. Ozatay, J. Sankey, D. Ralph, and R. Buhrman, “Magnetic vortex oscillator driven by dc spin-polarized current,” *Nature Physics*, vol. 3, no. 7, pp. 498–503, 2007.

[41] V. Pribiag, G. Finocchio, B. Williams, D. Ralph, and R. Buhrman, “Long-timescale fluctuations in zero-field magnetic vortex oscillations driven by dc spin-polarized current,” *Physical Review B*, vol. 80, no. 18, p. 180411, 2009.

[42] A. Tulapurkar, Y. Suzuki, A. Fukushima, H. Kubota, H. Maehara, K. Tsunekawa, D. Djayaprawira, N. Watanabe, and S. Yuasa, “Spin-torque diode effect in magnetic tunnel junctions,” *Nature*, vol. 438, no. 7066, pp. 339–342, 2005.

[43] A. A. Kovalev, G. E. Bauer, and A. Brataas, “Current-driven ferromagnetic resonance, mechanical torques, and rotary motion in magnetic nanostructures,” *Physical Review B*, vol. 75, no. 1, p. 014430, 2007.

[44] J. Sankey, P. Braganca, A. Garcia, I. Krivorotov, R. Buhrman, and D. Ralph, “Spin-transfer-driven ferromagnetic resonance of individual nanomagnets,” *Physical review letters*, vol. 96, no. 22, p. 227601, 2006.

[45] J. C. Sankey, Y.-T. Cui, J. Z. Sun, J. C. Slonczewski, R. A. Buhrman, and D. C. Ralph, “Measurement of the spin-transfer-torque vector in magnetic tunnel junctions,” *Nature Physics*, vol. 4, no. 1, pp. 67–71, 2008.

[46] C. Wang, Y.-T. Cui, J. Sun, J. Katine, R. Buhrman, and D. Ralph, “Bias and angular dependence of spin-transfer torque in magnetic tunnel junctions,” *Physical Review B*, vol. 79, no. 22, p. 224416, 2009.

[47] T. Dietl and H. Ohno, “Ferromagnetic iii–v and ii–vi semiconductors,” *MRS bulletin*, vol. 28, no. 10, pp. 714–719, 2003.

[48] N. Brandt and V. V. Moshchalkov, “Semimagnetic semiconductors,” *Advances in Physics*, vol. 33, no. 3, pp. 193–256, 1984.

[49] H. Ohno, “Making nonmagnetic semiconductors ferromagnetic,” *science*, vol. 281, no. 5379, pp. 951–956, 1998.

[50] A. Haury, A. Wasiela, A. Arnoult, J. Cibert, S. Tatarenko, T. Dietl, and Y. M. d’Aubigné, “Observation of a ferromagnetic transition induced by two-dimensional hole gas in modulation-doped cdmnte quantum wells,” *Physical Review Letters*, vol. 79, no. 3, p. 511, 1997.

[51] L. Hansen, D. Ferrand, G. Richter, M. Thierley, V. Hock, N. Schwarz, G. Reuscher, G. Schmidt, L. Molenkamp, and A. Waag, “Epitaxy and magnetotransport properties of the diluted magnetic semiconductor p-be (1- x) mnxte,” *Applied Physics Letters*, vol. 79, no. 19, pp. 3125–3127, 2001.

[52] C. Piermarocchi, P. Chen, L. J. Sham, and D. G. Steel, “Optical RKKY interaction between charged semiconductor quantum dots,” *Phys. Rev. Lett.*, vol. 89, p. 167402, 2002.

[53] H. Munekata, H. Ohno, S. Von Molnar, A. Segmüller, L. Chang, and L. Esaki, “Diluted magnetic iii-v semiconductors,” *Physical Review Letters*, vol. 63, no. 17, p. 1849, 1989.

[54] H. Ohno, H. Munekata, T. Penney, S. Von Molnar, and L. Chang, “Magnetotransport properties of p-type (in, mn) as diluted magnetic iii-v semiconductors,” *Physical Review Letters*, vol. 68, no. 17, p. 2664, 1992.

[55] J. De Boeck, R. Oesterholt, A. Van Esch, H. Bender, C. Bruynseraede, C. Van Hoof, and G. Borghs, “Nanometer-scale magnetic mnas particles in gaas

grown by molecular beam epitaxy," *Applied physics letters*, vol. 68, no. 19, pp. 2744–2746, 1996.

[56] H. Ohno, A. Shen, F. Matsukura, A. Oiwa, A. Endo, S. Katsumoto, and Y. Iye, "(ga, mn) as: a new diluted magnetic semiconductor based on gaas," *Applied Physics Letters*, vol. 69, no. 3, pp. 363–365, 1996.

[57] F. Matsukura, H. Ohno, A. Shen, and Y. Sugawara, "Transport properties and origin of ferromagnetism in (ga, mn) as," *Physical Review B*, vol. 57, no. 4, p. R2037, 1998.

[58] H. Ohno, "Properties of ferromagnetic iii–v semiconductors," *Journal of magnetism and magnetic materials*, vol. 200, no. 1, pp. 110–129, 1999.

[59] Y. Ohno, D. Young, B. a. Beschoten, F. Matsukura, H. Ohno, and D. Awschalom, "Electrical spin injection in a ferromagnetic semiconductor heterostructure," *Nature*, vol. 402, no. 6763, pp. 790–792, 1999.

[60] P. Van Dorpe, Z. Liu, W. Van Roy, V. Motsnyi, M. Sawicki, G. Borghs, and J. De Boeck, "Very high spin polarization in gaas by injection from a (ga, mn) as zener diode," *Applied physics letters*, vol. 84, no. 18, pp. 3495–3497, 2004.

[61] M. Tanaka and Y. Higo, "Large tunneling magnetoresistance in gamnas/alas/gamnas ferromagnetic semiconductor tunnel junctions," *Physical Review Letters*, vol. 87, no. 2, p. 026602, 2001.

[62] V. Korenev, I. Akimov, S. Zaitsev, V. Sapega, L. Langer, D. Yakovlev, Y. A. Danilov, and M. Bayer, "Dynamic spin polarization by orientation-dependent separation in a ferromagnet–semiconductor hybrid," *Nature communications*, vol. 3, p. 959, 2012.

[63] M. Yamanouchi, D. Chiba, F. Matsukura, and H. Ohno, "Current-induced domain-wall switching in a ferromagnetic semiconductor structure," *Nature*, vol. 428, no. 6982, pp. 539–542, 2004.

[64] S. Zaitsev, M. Dorokhin, A. Brichkin, O. Vikhrova, Y. A. Danilov, B. Zvonkov, and V. Kulakovskii, "Ferromagnetic effect of a mn delta layer in the gaas barrier on the spin polarization of carriers in an ingaas/gaas quantum well," *JETP letters*, vol. 90, no. 10, pp. 658–662, 2010.

[65] V. L. Korenev, "Electric control of magnetic moment in a ferromagnet/semiconductor hybrid system," *Journal of Experimental and Theoretical Physics Letters*, vol. 78, no. 9, pp. 564–568, 2003.

[66] O. Madelung, *Semiconductors: group IV elements and III-V compounds*. Springer Science & Business Media, 2012.

[67] T. Dietl, "Magnetic semiconductors," *interaction*, vol. 2, no. 5, p. 9, 1994.

[68] J. Okabayashi, A. Kimura, O. Rader, T. Mizokawa, A. Fujimori, T. Hayashi, and M. Tanaka, "Core-level photoemission study of ga 1- x mn x as," *Physical Review B*, vol. 58, no. 8, p. R4211, 1998.

[69] H. Ohldag, V. Solinus, F. Hillebrecht, J. Goedkoop, M. Finazzi, F. Matsukura, H. Ohno, *et al.*, "Magnetic moment of mn in the ferromagnetic semiconductor (ga˜ 0˜.˜ 9˜ 8mn˜ 0˜.˜ 0˜ 2) as," *Applied Physics Letters*, vol. 76, no. 20, pp. 2928–2930, 2000.

[70] J. Okabayashi, A. Kimura, O. Rader, T. Mizokawa, A. Fujimori, T. Hayashi, and M. Tanaka, "Angle-resolved photoemission study of ga 1- x mn x as," *Physical Review B*, vol. 64, no. 12, p. 125304, 2001.

[71] N. Mott, "The metal-insulator transition in extrinsic semiconductors," *Advances in Physics*, vol. 21, no. 94, pp. 785–823, 1972.

[72] N. F. Mott and L. Friedman, "Metal-insulator transitions in vo2, ti2o3 and ti2-x v x o3," *Philosophical Magazine*, vol. 30, no. 2, pp. 389–402, 1974.

[73] B. I. Shklovskii and A. L. Efros, *Electronic properties of doped semiconductors*, vol. 45. Springer Science & Business Media, 2013.

[74] M. Berciu and R. Bhatt, "Effects of disorder on ferromagnetism in diluted magnetic semiconductors," *Physical Review Letters*, vol. 87, no. 10, p. 107203, 2001.

[75] D. A. Woodbury and J. Blakemore, "Impurity conduction and the metal-nonmetal transition in manganese-doped gallium arsenide," *Physical Review B*, vol. 8, no. 8, p. 3803, 1973.

[76] A. Van Esch, L. Van Bockstal, J. De Boeck, G. Verbanck, A. Van Steenbergen, P. Wellmann, B. Grietens, R. Bogaerts, F. Herlach, and G. Borghs, "Interplay between the magnetic and transport properties in the iii-v diluted magnetic semiconductor ga 1- x mn x as," *Physical Review B*, vol. 56, no. 20, p. 13103, 1997.

[77] T. Dietl and H. Ohno, "Dilute ferromagnetic semiconductors: Physics and spintronic structures," *Rev. Mod. Phys.*, vol. 86, pp. 188–251, 2014.

[78] R. Campion, K. Edmonds, L. Zhao, K. Wang, C. Foxon, B. Gallagher, and C. Staddon, "The growth of gamnas films by molecular beam epitaxy using arsenic dimers," *Journal of crystal growth*, vol. 251, no. 1, pp. 311–316, 2003.

[79] C. Timm, F. Schäfer, and F. von Oppen, "Correlated defects, metal-insulator transition, and magnetic order in ferromagnetic semiconductors," *Physical review letters*, vol. 89, no. 13, p. 137201, 2002.

[80] S.-R. E. Yang and A. MacDonald, "Disorder and ferromagnetism in diluted magnetic semiconductors," *Physical Review B*, vol. 67, no. 15, p. 155202, 2003.

[81] P. W. Anderson, "Absence of diffusion in certain random lattices," *Physical review*, vol. 109, no. 5, p. 1492, 1958.

[82] C. Timm, "Disorder effects in diluted magnetic semiconductors," *Journal of Physics: Condensed Matter*, vol. 15, no. 50, p. R1865, 2003.

[83] S. Von Molnar, H. Munekata, H. Ohno, and L. Chang, "New diluted magnetic semiconductors based on iii–v compounds," *Journal of Magnetism and Magnetic Materials*, vol. 93, pp. 356–364, 1991.

[84] H. Ohno, D. Chiba, F. Matsukura, T. Omiya, E. Abe, T. Dietl, Y. Ohno, and K. Ohtani, "Electric-field control of ferromagnetism," *Nature*, vol. 408, no. 6815, pp. 944–946, 2000.

[85] K. Burch, D. Shrekenhamer, E. Singley, J. Stephens, B. Sheu, R. Kawakami, P. Schiffer, N. Samarth, D. Awschalom, and D. Basov, "Impurity band conduction in a high temperature ferromagnetic semiconductor," *Physical review letters*, vol. 97, no. 8, p. 087208, 2006.

[86] J. Qi, Y. Xu, A. Steigerwald, X. Liu, J. Furdyna, I. Perakis, and N. Tolk, "Ultrafast laser-induced coherent spin dynamics in ferromagnetic ga 1- x mn x

as/gaas structures," *Physical Review B*, vol. 79, no. 8, p. 085304, 2009.

[87] E. Rozkotová, P. Němec, P. Horodyská, D. Sprinzl, F. Trojánek, P. Malỳ, V. Novák, K. Olejník, M. Cukr, and T. Jungwirth, "Light-induced magnetization precession in gamnas," *Applied Physics Letters*, vol. 92, no. 12, p. 122507, 2008.

[88] N. Tesařová, P. Němec, E. Rozkotová, F. Trojánek, and P. Malỳ, "Light-induced precession of magnetization in ferromagnetic semiconductor (ga, mn) as," *Acta Physica Polonica A*, vol. 118, no. 5, pp. 1065–1066, 2010.

[89] N. Tesařová, P. Němec, E. Rozkotová, J. Zemen, T. Janda, D. Butkovičová, F. Trojánek, K. Olejník, V. Novák, P. Malỳ, *et al.*, "Experimental observation of the optical spin-orbit torque," *Nature Photonics*, vol. 7, no. 6, pp. 492–498, 2013.

[90] J. Shah, *Ultrafast spectroscopy of semiconductors and semiconductor nanostructures*, vol. 115. Springer Science & Business Media, 2013.

[91] M. Dyakonov, "Basics of semiconductor and spin physics," in *Spin Physics in Semiconductors*, pp. 1–28, Springer, 2008.

[92] S. Maekawa, *Concepts in spin electronics*, vol. 13. Oxford University Press on Demand, 2006.

[93] P. Němec, E. Rozkotová, N. Tesařová, F. Trojánek, E. De Ranieri, K. Olejník, J. Zemen, V. Novák, M. Cukr, P. Malỳ, *et al.*, "Experimental observation of the optical spin transfer torque," *Nature Physics*, vol. 8, no. 5, pp. 411–415, 2012.

[94] A. Chernyshov, M. Overby, X. Liu, J. K. Furdyna, Y. Lyanda-Geller, and L. P. Rokhinson, "Evidence for reversible control of magnetization in a ferromagnetic material by means of spin–orbit magnetic field," *Nature Physics*, vol. 5, no. 9, pp. 656–659, 2009.

[95] D. Fang, H. Kurebayashi, J. Wunderlich, K. Vỳbornỳ, L. Zârbo, R. Campion, A. Casiraghi, B. Gallagher, T. Jungwirth, and A. Ferguson, "Spin-orbit-driven ferromagnetic resonance," *Nature nanotechnology*, vol. 6, no. 7, pp. 413–417, 2011.

[96] J. Zemen, J. Kučera, K. Olejník, and T. Jungwirth, "Magnetocrystalline anisotropies in (ga, mn) as: Systematic theoretical study and comparison with experiment," *Physical Review B*, vol. 80, no. 15, p. 155203, 2009.

[97] T. Dietl, H. Ohno, F. Matsukura, J. Cibert, and D. Ferrand, "Zener model description of ferromagnetism in zinc-blende magnetic semiconductors," *Science*, vol. 287, no. 5455, pp. 1019–1022, 2000.

[98] H. J. Lipkin, *Quantum Mechanics – New Approaches to Selected Topics*. Amsterdam: North-Holland, 1973.

[99] D. C. Ralph and M. D. Stiles, "Spin transfer torques," *J. Magn. Magn. Mat.*, vol. 320, pp. 1190–1216, 2008.

[100] A. Kirilyuk, A. V. Kimel, and T. Rasing, "Ultrafast optical manipulation of magnetic order," *Rev. Mod. Phys.*, vol. 82, pp. 2731–2784, 2010.

[101] K. Vahaplar, A. M. Kalashnikova, A. V. Kimel, S. Gerlach, D. Hinzke, U. Nowak, R. Chantrell, A. Tsukamoto, A. Itoh, A. Kirilyuk, and T. Rasing, "All-optical magnetization reversal by circularly polarized laser pulses: Experiment and multiscale modeling," *Phys. Rev. B*, vol. 85, p. 104402, 2012.

[102] S. Mangin, M. Gottwald, C. Lambert, D. Steil, V. Uhlíř, L. Pang, M. Hehen, S. Alebrand, M. Cinchetti, G. Malinowksi, Y. Fainman, M. Aeschlimann, and E. E. Fullerton, "Engineered materials for all-optical helicity-dependent magnetic switching," *Nature Mat.*, vol. 13, pp. 286–292, 2014.

[103] C. Comte and G. Mahler, "Dynamic Stark effect in interacting electron-hole systems: Light-enhanced excitons," *Phys. Rev. B*, vol. 34, p. 7164, 1986.

[104] S. Schmitt-Rink, D. S. Chemla, and H. Haug, "Nonequilibrium theory of the optical Stark effect and spectral hole burning in semiconductors," *Phys. Rev. B*, vol. 37, p. 941, 1988.

[105] J. Fernández-Rossier, C. Piermarocchi, P. Chen, A. H. MacDonald, and L. J. Sham, "Coherently photoinduced ferromagnetism in diluted magnetic semiconductors," *Phys. Rev. Lett.*, vol. 93, p. 127201, 2004.

[106] G. Zi-zhao and Y. Guo-zhen, "Theory of coherent propagation of a light wave in semiconductors. I," *Phys. Rev. B*, vol. 26, p. 6826, 1982.

[107] M. Rontani and L. J. Sham, "Coherent exciton transport in semiconductors," in *Novel Superfluids Volume 2* (K. H. Bennemann and J. B. Ketterson, eds.), vol. 157 of *International Series of Monographs on Physics*, ch. 19, pp. 423–474, Oxford, UK: Oxford University Press, 2014.

[108] C. Ciuti, J. P. McGuire, and L. J. Sham, "Spin polarization of semiconductor carriers by reflection off a ferromagnet," *Phys. Rev. Lett.*, vol. 89, p. 156601, 2002.

[109] S. Garzon, L. Ye, R. A. Webb, T. M. Crawford, M. Covington, and S. Kaka, "Coherent control of nanomagnet dynamics via ultrafast spin torque pulses," *Phys. Rev. B*, vol. 78, p. 180401, 2008.

[110] T. Uenoyama and L. J. Sham, "Hole relaxation and luminescence polarization in doped and undoped quantum wells," *Phys. Rev. Lett.*, vol. 64, pp. 3070–3073, 1990.

[111] J. M. Kikkawa and D. D. Awschalom, "Resonant spin amplification in *n*-type GaAs," *Phys. Rev. Lett.*, vol. 80, pp. 4313–4316, 1998.

[112] U. Fano, "Effects of configuration interaction on intensities and phase shifts," *Phys. Rev.*, vol. 124, pp. 1866–1878, 1961.